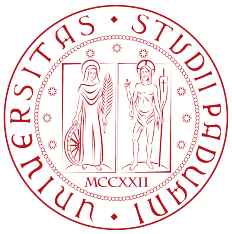

UNIVERSITÀ DEGLI STUDI DI PADOVA

Dipartimento di Fisica e Astronomia

Scuola di Dottorato di Ricerca in Fisica

CICLO XXVII

The neon-sodium cycle: Study of the ^{22}Ne(p, γ)^{23}Na reaction at astrophysical energies

---

Direttore della scuola: Ch.mo Prof. Andrea Vitturi
Supervisore: Dr. Carlo Broggini

Dottorando: Rosanna Depalo

Abstract

The ^{22}Ne(p,γ)^{23}Na reaction takes part in the neon-sodium cycle of hydrogen burning. This cycle plays a crucial role for the synthesis of the elements with mass A = 20-25 in asymptotic giant branch stars, classical novae explosions and type Ia supernovae, where hydrogen burning occurs at high temperatures. The ^{22}Ne(p,γ)^{23}Na thermonuclear reaction rate is highly uncertain because of a large number of poorly known resonances lying at astrophysical energies.
This thesis reports on a new experimental study of the ^{22}Ne(p,γ)^{23}Na reaction. In particular, two experiments have been performed to pin down the cross section of the proton capture on ^{22}Ne: a measurement of the resonances at proton energies below 400 keV has been performed at the Laboratory for Underground Nuclear Astrophysics (LUNA) in Gran Sasso (Italy), while a high-precision study of the resonances between 400 and 660 keV has been performed at the Helmoltz-Zentrum Dresden-Rossendorf (Germany).
For the LUNA measurement, a windowless gas target filled with enriched ^{22}Ne was used and the gamma rays emitted in the ^{23}Na decay were detected by two high-purity germanium detectors. The experiment performed at LUNA led to the first detection of three previously unobserved resonances. Moreover, the decay schemes of the corresponding excited states of ^{23}Na have been extended with the observation of new transitions. The LUNA measurement also allowed to reduce the upper limits on three unobserved resonances that represent the main source of uncertainty for the reaction rate.
The HZDR experiment was performed with a ^{22}Ne solid target and two high-purity germanium detectors surrounded by BGO anti-Compton shields. The target were prepared implanting ^{22}Ne on a tantalum backing. The implantation was performed at the 200 kV high-current implanter of Legnaro National Laboratories (Italy).
To improve the precision on the strengths of the resonances between 400 and 660 keV, the well known ^{22}Ne(p,γ)^{23}Na resonances at 1279 keV and 478 keV were used for normalization. This measurement allowed to reduce the uncertainty on the strengths of the 436 keV and 638.5 keV resonances up to a factor of three. Moreover, the strength of the 661 keV resonance has been revised downward by one order of magnitude.
Taking into account the new results, an updated thermonuclear reaction rate has been calculated. At the temperatures of classical novae explosions, the uncertainty on the reaction rate has been reduced by about one order of magnitude compared to the literature.

Sommario

La reazione ^{22}Ne(p,γ)^{23}Na fa parte del ciclo neon-sodio per il bruciamento dell' idrogeno. Il ciclo neon-sodio gioca un ruolo fondamentale per la sintesi degli elementi con massa A = 20-25 nelle stelle in fase di asymptotic giant branch, nelle esplosioni di novae di tipo classico e nelle esplosioni di supernovae di tipo Ia, dove il bruciamento di idrogeno avviene ad alte temperature.
In particolare, la reazione ^{22}Ne(p,γ)^{23}Na è la più incerta del ciclo neon-sodio. L'incertezza sulla sezione d'urto è dovuta al contributo, alle energie di interesse astrofisico, di un gran numero di risonanze. Alcune di queste risonanze non sono mai state osservate, per altre, invece, l'intensità è conosciuta con grande incertezza.
Per misurare la sezione d'urto della ^{22}Ne(p,γ)^{23}Na alle energie di interesse astrofisico, due esperimenti sono stati condotti nell'ambito di questa tesi: il primo, svolto con l'apparato sperimentale di LUNA, ha permesso di esplorare le risonanze di energia inferiore a 400 keV. Il secondo, invece, è stato svolto all'Helmoltz-Zentrum Dresden-Rossendorf (HZDR), in Germania, ed ha permesso di miglirare la precisione sulle intensità delle risonanze tra 400 e 660 keV.
Per la misura svolta al Gran Sasso è stato usato un bersaglio di tipo gassoso senza finestre di ingresso e i fotoni emessi nel decadimento del ^{23}Na sono stati osservati con due rivelatori al germanio. L'esperimento svolto a LUNA ha permesso di rivelare per la prima volta tre risonanze. Per queste risonanze sono stati osservati anche nuovi modi di decadimento gamma. Questo ha permesso di ampliare gli schemi di decadimento di letteratura. Questa misura ha permesso, inoltre, di ridurre di due ordini di grandezza i limiti superiori sulle intensit di tre risonanze la cui esistenza è tuttora dubbia.
Per l'esperimento svolto all'HZDR è stato utilizzato un bersaglio solido di ^{22}Ne e due rivelatori al germanio circondati da schermi anti Compton. I target sono stati realizzati all'impiantatore da 200 kV dei Laboratori Nazionali di Legnaro impiantando il ^{22}Ne su una targhetta di tantalio.
L'intensità delle risonanze tra 400 e 660 keV è stata misurata usando come riferimento le risonanze a 1279 keV e 478 keV, che sono intense e ben note. Questo esperimento ha permesso di ridurre l'incertezza sull'intensità della risonanza a 436 keV di un fattore tre, mentre, per la risonanza a 661 keV, è stata determinata un'intensità un ordine di grandezza inferiore rispetto alla letteratura.
Il rate di reazione astrofisico è stato aggiornato tenendo conto dei nuovi risultati descritti sopra. Alle temperature caratteristiche delle esplosioni di novae di tipo classico, l'incertezza sul nuovo rate è un ordine di grandezza inferiore rispetto alla letteratura.

Contents

Introduction **3**

1 Astrophysical motivation **5**
1.1 Thermonuclear reaction rate . . . 5
1.2 The neon - sodium cycle and the ^{22}Ne(p,γ)^{23}Na reaction . . . 8
1.2.1 RGB and AGB stars . . . 10
1.2.2 Classical nove and type Ia supernovae . . . 11
1.3 ^{22}Ne(p,γ)^{23}Na reaction rate: state of the art . . . 13

2 Study of ^{22}Ne(p,γ)^{23}Na low energy resonances at LUNA **19**
2.1 The LUNA experiment . . . 19
2.1.1 The LUNA 400 kV accelerator . . . 19
2.1.2 The gas target system . . . 20
2.1.3 Gas density measurement . . . 22
Gas density without beam . . . 23
Beam heating effect . . . 26
2.1.4 Setup design . . . 29
2.1.5 Detection efficiency . . . 34
Summing-out correction . . . 39
2.2 Data analysis and results . . . 43
2.2.1 156.2 keV resonance . . . 44
Branching ratios . . . 44
2.2.2 189.5 keV resonance . . . 46
Gamma - gamma coincidences . . . 46
Branching ratios . . . 51
2.2.3 259.7 keV resonance . . . 51
Gamma - gamma coincidences . . . 54
Branching ratios . . . 56
2.2.4 Resonance strength determination . . . 58

3 Study of ^{22}Ne(p,γ)^{23}Na high energy resonances at HZDR **61**
3.1 Experimental Setup . . . 61
3.1.1 ^{22}Ne solid target preparation . . . 62
3.1.2 Detectors and data acquisition . . . 63
Detection efficiency . . . 64
3.2 Data Analysis and results . . . 68
3.2.1 Study of ^{22}Ne implantation profile . . . 69

1279 keV resonance 69
479 keV resonance 70
3.2.2 436 keV resonance 75
3.2.3 638.5 keV resonance 76
3.2.4 661 keV resonance 80
3.2.5 Resonance strengths 83

4 Astrophysical reaction rate **85**
4.1 Nonresonant reaction rate 85
4.2 Narrow-resonance reaction rate 86

Summary **91**

Bibliography **93**

Introduction

The idea that the energy powering the stars is produced by nuclear reactions was first formulated by Eddington in 1920. Since then, great progress has been made concerning the understanding of stellar structure and nucleosynthesis both on the theoretical and on the experimental side.
With the development of high resolution spectrometry it has become possible to measure the abundances of the elements in the stellar photosphere with unprecedent accuracy. Theoretical models are trying to reproduce the observed abundances but, in order to achieve the same level of accuracy of the observations, the input parameters of the model should also be well known, and nuclear cross sections are among these parameters.
Measuring nuclear cross sections at astrophysical energies is a challenge that triggered a huge amount of experimental work. At stellar temperatures the kinetic energy of the interacting nuclei is much lower than the Coulomb repulsion energy, therefore nuclear reactions can only occur *via* tunnel effect. This makes the cross section extremely small (of the order of nano or femto barn) and difficult to measure. The main issue is that, approaching the astrophysically relevant energy range, any nuclear reaction signal becomes smaller and smaller until it gets lost in the background mainly produced by cosmic radiation and environmental radioactivity.
Over the years, different techniques have been developed to face this problem: on one side, cross sections measured at high energies can be extrapolated to stellar energies. This approach may produce wrong results if, for example, unforseen resonances lie in the experimentally unexplored energy region. On the other side, indirect techniques have been developed to measure either nuclear cross sections or the nuclear parameters needed to derive the cross section. Anyway, a direct measurement at astrophysical energies remains the best way to constraint nuclear reactions and reduce the nuclear uncertainty in stellar models.
A breakthrough in this direction was the first operation of an underground accelerator at the Laboratory for Underground Nuclear Astrophysics (LUNA) in Gran Sasso, Italy. The 1400 meters of rocks above the laboratory act as a natural shield against cosmic radiation, suppressing the background by orders of magnitude.
This thesis reports on a new direct measurement of the ^{22}Ne(p,γ)^{23}Na reaction. The proton capture on ^{22}Ne takes part in the neon-sodium cycle of hydrogen burning. This cycle plays a crucial role for the synthesis of the elements with mass A = 20-25 during hydrogen burning at high temperatures. ^{22}Ne(p,γ)^{23}Na is the most uncertain reaction of the neon-sodium cycle (the uncertainty on the reaction rate is as high as a factor of 2000). The uncertainty is due to a large

number of resonances lying at astrophysical energies. None of the resonances at proton energy below 400 keV has ever been observed either in direct or in indirect experiments and only the energies of the corresponding excited state in ^{23}Na are known. On the other hand, the resonances above 400 keV are known with high uncertainties.
Two experiments have been performed to pin down the cross section of the proton capture on ^{22}Ne: in order to investigate the unobserved resonances, a measurement at proton energies below 400 keV has been performed at LUNA, while a high-precision study of the resonances between 400 and 660 keV has been performed at the Helmoltz-Zentrum Dresden-Rossendorf (Germany).
This thesis is organized as follows: chapter 1 provides a description of the astrophysical relevance of the ^{22}Ne(p,γ)^{23}Na reaction and it gives an overview of the current knowledge of its cross section. Chapter 2 is dedicated to the ^{22}Ne(p,γ)^{23}Na experiment performed at LUNA, while chapter 3 reports on the HZDR measurement. Finally, the impact of the new measurements on the ^{22}Ne(p,γ)^{23}Na thermonuclear reaction rate is discussed in chapter 4.

Chapter 1

Astrophysical motivation

Nuclear reactions provide most of the energy radiated by stars. The whole life of a star consists of a sequence of phases in which heavier and heavier elements are burnt inside the stellar core. The network of nuclear reactions taking place in stars is also responsible for the production of all the elements starting from primordial hydrogen and helium (with the exception of beryllium and boron, which are mainly produced by cosmic ray spallation).
Theoretical models have been developed to understand the evolution of stars and to try to reproduce the observed elemental abundances. An important input for these models is the thermonuclear reaction rate for all the nuclear reactions involved (i.e. the number of reactions per unit time and volume happening in a star at a given temperature).
In the folowing sections, the general procedure to evaluate thermonuclear reaction rates is described. Then the role of the ^{22}Ne(p,γ)^{23}Na in different astrophysical scenarios is discussed. Finally, an overview of the literature information on the ^{22}Ne(p,γ)^{23}Na cross section is given.

1.1 Thermonuclear reaction rate

The rate of a nuclear reaction is defined as the number of reactions per unit time and volume [1]. It depends on the nuclear cross section σ, on the density of interacting particles n_1 and n_2 and on their relative velocity v:

$$\frac{N_R}{V \cdot t} = \sigma \cdot v \cdot n_1 \cdot n_2 \tag{1.1}$$

In a non degenerate stellar plasma at thermodynamic equilibrium, the relative velocity of the interacting nuclei follows a Maxwell-Boltzmann distribution:

$$P(v) \cdot dv = \left(\frac{\mu}{2\pi k_B T}\right)^{3/2} e^{-\mu v^2/(2k_B T)} 4\pi v^2 \cdot dv \tag{1.2}$$

where μ is the reduced mass of the interacting particles, k_B is the Boltzmann constant and T is the star temperature.
Assuming $E = \mu v^2/2$, the velocity distribution 1.2 can be written as an energy distribution:

$$P(E) \cdot dE = \frac{2}{\sqrt{\pi}} \frac{1}{(k_B T)^{3/2}} \sqrt{E} e^{-E/k_B T} \cdot dE \tag{1.3}$$

and the reaction rate per particle pair becomes:

$$\langle \sigma v \rangle = \int_0^\infty \sqrt{\frac{2E}{\mu}} \sigma(E) P(E) dE = \left(\frac{8}{\pi\mu}\right)^{1/2} \frac{1}{(kT)^{3/2}} \int_0^\infty E\sigma(E) exp\left(-\frac{E_R}{kT}\right) dE \tag{1.4}$$

At stellar temperatures, the kinetic energy of the interacting particles is usually much lower than the Coulomb repulsion between the nuclei. Therefore, nuclear reactions can only occur by quantum mechanical tunneling and the cross section decreases exponentially with the energy:

$$\sigma = \frac{1}{E} S(E) exp\left(-\frac{2\pi}{\hbar}\sqrt{\frac{\mu}{2E}} Z_1 Z_2 e^2\right) = \frac{1}{E} S(E) e^{-2\pi\eta} \tag{1.5}$$

where Z_1 and Z_2 are the atomic charges of the target and projectile, S(E) is called the astrophysical S-factor and $e^{-2\pi\eta}$ is the Gamow factor, representing the s-wave Coulomb barrier transmission probability at energies well below the height of the Coulomb barrier.
With this definition, the thermonuclear reaction rate becomes:

$$\langle \sigma v \rangle = \left(\frac{8}{\pi\mu}\right)^{1/2} \frac{1}{(kT)^{3/2}} \int_0^\infty S(E) e^{-2\pi\eta} e^{-E/kT} dE \tag{1.6}$$

Fig. 1.2 shows how the terms $e^{-2\pi\eta}$ and $e^{-E/kT}$ change with the energy, together with their product.

The integrand of equation 1.6 has its highest values in an energy region called the *Gamow peak*. The Gamow peak represents the energy window over which most of the nuclear reactions occur and it depends on the mass and charge of the interacting nuclei and on the typical temperature of the astrophysical environment of interest. At energies lower than the Gamow window, the Coulomb barrier penetrability becomes too low, suppressing the cross section. At higher energies the number of interacting nuclei lying in the tail of the Maxwell-Boltzmann distribution becomes smaller and smaller.
The reaction cross section inside the Gamow window should therefore be accurately known in order to evaluate the thermonuclear reaction rate.
For an astrophysical environment at temperature T_9 (in GK) and for a given system of interacting particles with atomic charge $Z_{1,2}$ and mass $M_{1,2}$, the energy of the maximum of the Gamow peak in MeV can be approximated as:

$$E_0 = 0.122 \left(Z_1^2 Z_2^2 \frac{M_1 M_2}{M_1 + M_2} T_9^2\right)^{1/3} \tag{1.7}$$

while the $1/e$ width Δ can be estimated approximating the Gamow peak with a Gaussian function:

$$\Delta = \frac{4}{\sqrt{3}} \sqrt{E_0 k_B T} \tag{1.8}$$

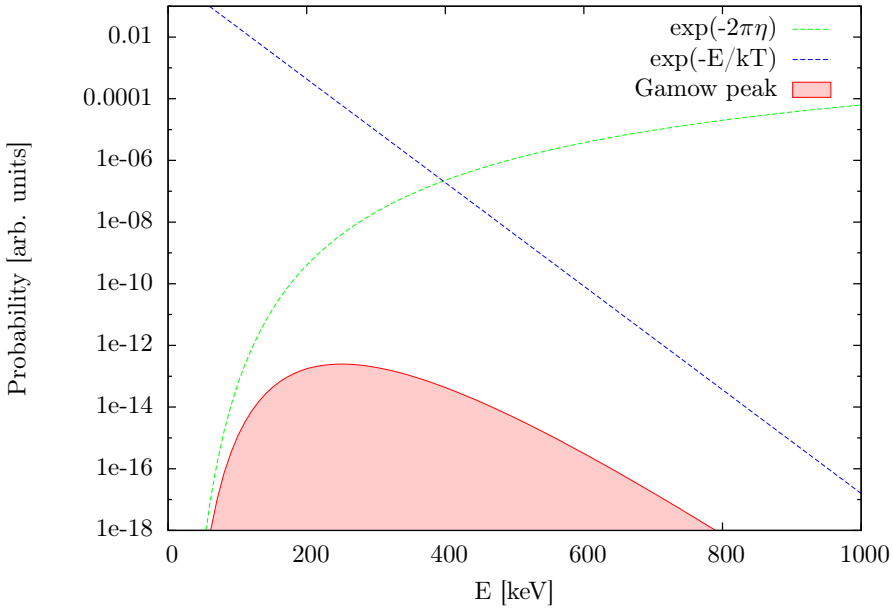

Figure 1.1: Gamow peak for the ^{22}Ne(p,γ)^{23}Na reaction at a typical peak temperature for classical novae explosions (T = 0.3 GK). The exponential terms in the integral of equation 1.6 are also shown.

Hereafter, the lower and upper bounds of the energy regions of astrophysical interest are approximated as $E_0(T_{min}) - \Delta(T_{min})/2$ and $E_0(T_{max}) + \Delta(T_{max})/2$ (where T_{min} and T_{max} are the minimum and maximum temperatures involved).

As discussed below, the ^{22}Ne(p,γ)^{23}Na cross section is characterized by a large number of narrow resonances.
When a nuclear reaction proceeds through an isolated narrow resonance, an excited state E_x is first formed in the entrance channel, which subsequently decays to lower lying states [2]. This process only occurs when the sum of the Q-value [1] and the energy of the projectile in the center of mass E_R corresponds to the energy of the excited state:

$$E_x = E_R + Q \tag{1.9}$$

When a resonance occurs, the reaction cross section sharply changes. The cross section trand as a function of the energy can be desribed by the Breit-Wigner formula:

$$\sigma_{BW}(E) = \pi\lambda^2 \frac{2J+1}{(2j_1+1)(2j_2+1)}(1+\delta_{12})\frac{\Gamma_a\Gamma_b}{(E-E_R)^2+(\Gamma/2)^2} \tag{1.10}$$

where:

[1] difference between the sum of the masses of the initial reactants and the sum of the masses of the final products, in energy units

- $\lambda = 2\pi\hbar/\sqrt{2\mu E}$ is the de Broglie wavelength of the projectile in the center of mass system
- j_1 and j_2 are the spins of the interacting particles and J is the spin of the excited state populated in the compound nucleus
- δ_{12} is the Kronecker delta function
- Γ_a and Γ_b are the partial widths for the entrance and exit channels, representing the probability for the formation and the decay of the compound state
- $\Gamma = \Gamma_a + \Gamma_b + ...$ is the total width of the resonance (all open decay channels are included in the sum)
- E_R is the resonance energy in the center of mass frame

In presence of a resonance, the stellar reaction rate can be calculated as:

$$\langle \sigma v \rangle = \left(\frac{8}{\pi\mu}\right)^{1/2} \frac{1}{(kT)^{3/2}} \int_0^\infty E exp\left(-\frac{E}{kT}\right) \sigma_{BW}(E) dE \tag{1.11}$$

for a narrow resonance, $\Gamma << E_R$ and the Maxwell - Boltzmann function, $E \cdot exp(-\frac{E}{kT})$, changes very little over the resonance region therefore its value at $E = E_R$ can be taken outside the integral:

$$\langle \sigma v \rangle = \left(\frac{8}{\pi\mu}\right)^{1/2} \frac{1}{(kT)^{3/2}} E_R exp\left(-\frac{E_R}{kT}\right) \int_0^\infty \sigma_{BW}(E) dE \tag{1.12}$$

The integration of the Breit-Wigner cross section yields, assuming a negligible energy dependence of the partial and total widths,

$$\int_0^\infty \sigma_{BW}(E) dE = 2\pi^2 \lambda^2 \omega\gamma \tag{1.13}$$

with:

$$\omega\gamma = \frac{2J+1}{(2j_1+1)(2j_2+1)}(1+\delta_{12})\frac{\Gamma_a \Gamma_b}{\Gamma} \tag{1.14}$$

The factor $\omega\gamma$ is called the resonance strength and expresses the integrated cross section.
In the following sections, the astrophysical environments defining the Gamow window for the ^{22}Ne(p,γ)^{23}Na are illustrated, and the current knowledge on the ^{22}Ne+p cross section is summarized.

1.2 The neon - sodium cycle and the ^{22}Ne(p,γ)^{23}Na reaction

The neon - sodium cycle of hydrogen burning allows the conversion of four protons into helium using neon and sodium isotopes as catalysts. The NeNa cycle is not

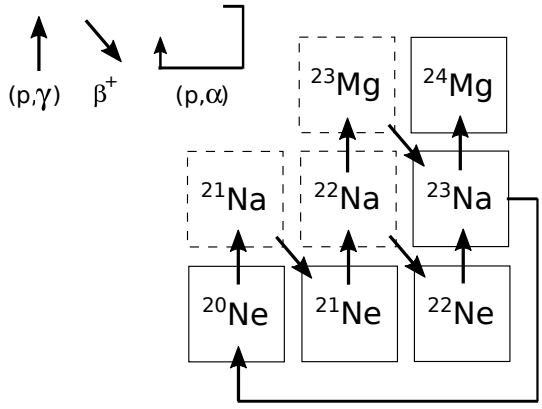

Figure 1.2: Schematic view of the neon sodium cycle of hydrogen burning. Stable isotopes are reported with solid squares while unstable isotopes are drawn with dashed squares.

a very strong source of energy for stars. Its importance lies, however, in the fact that it allows the synthesis of the elements between ^{20}Ne and ^{24}Mg [3].

Fig. 1.3 shows the reaction rates of all the reactions involved in the NeNa cycle. The bottleneck of the cycle (i.e. the reaction with the smallest rate) is ^{20}Ne(p,γ)^{21}Na. The ^{22}Ne(p,γ)^{23}Na reaction is instead the most puzzling. For this reaction, the thermonuclear rates reported in the NACRE compilation [4] and in the more recent compilation by C. Iliadis et al. [5] differ by about three orders of magnitude and the adopted uncertainties are also orders of magnitude different (see sec. 1.3).

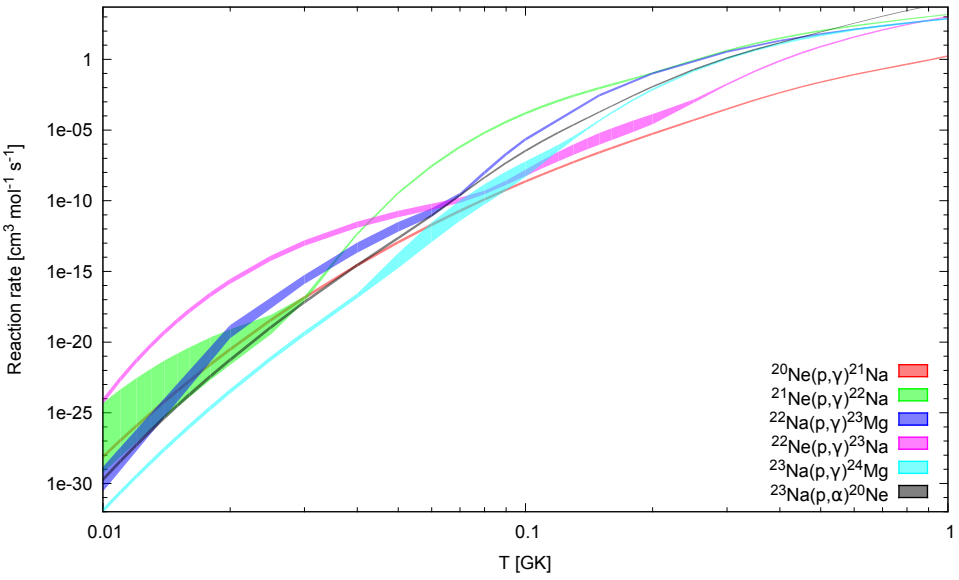

Figure 1.3: Reaction rates for all the reactions involved in the NeNa cycle. For each reaction, a band between the lower and upper limits on the reaction rate is reported. All reaction rates are from [5], except the rate of the ^{22}Na(p,γ)^{23}Mg reaction which is taken from [6].

Whithin the NeNa cycle, ^{22}Ne can only be produced by the decay of ra-

dioactive ^{22}Na ($T_{1/2}$ = 2.6 y). However, the beta decay competes with proton capture on ^{22}Na. At temperatures T > 0.07 GK the proton capture is stronger than the beta decay and ^{22}Ne is bypassed in the NeNa cycle. Nevertheless, ^{22}Ne is efficiently produced from the ashes of the CNO cycle through the chain: ^{14}N(α,γ)^{18}F($\beta^+\nu$)^{18}O(α,γ)^{22}Ne. Therefore ^{22}Ne can still be present in second generation stars or whenever material processed through the CNO cycle is mixed with helium-rich material.

1.2.1 RGB and AGB stars

The Red Giant Branch (RGB) phase of stellar evolution is a transition phase between the core hydrogen burning and core helium burning phases. When the hydrogen fuel is exhausted in the stellar core, hydrogen burning reactions remain active in a thin shell. As the shell moves outward, the core contracts because there is no energy source balancing the gravitational force. On the other hand, the outer layers expand until a convective envelope is developed to transport the energy produced in the shell. The RGB phase ends when the helium mass in the core is high enough to ignite helium burning.

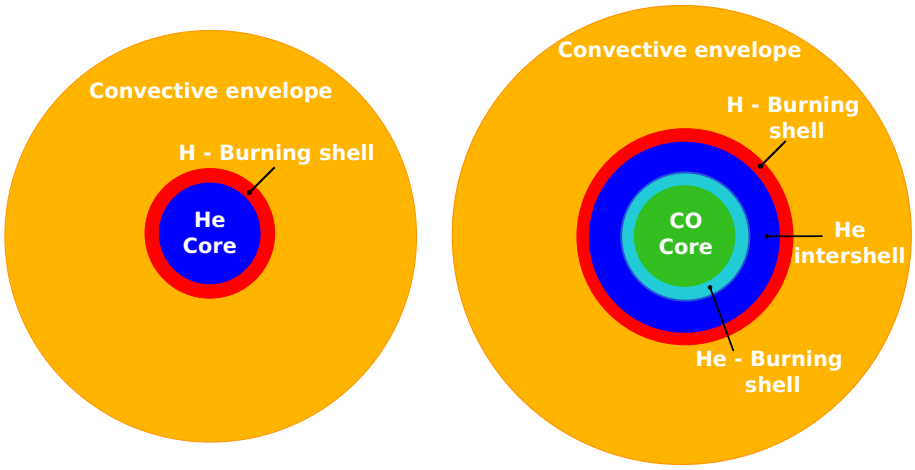

Figure 1.4: Schematic illustration of the structure of an RGB star (left) and an AGB star (right).

The observation of globular cluster red giants with high resolution spectrometers opened new scenarios on stellar evolution and galactic chemical evolution. Globular clusters were considered to be sets of stars with the same age and initial composition. Recent works have shown that globular clusters actually host stars with different ages and very different composition [7]. The discovery of the anticorrelation between sodium and oxygen abundances in all the globular clusters investigated with high resolution spectrometers is the most outstanding signature [8].
Oxygen depletion and sodium enrichment are the results of the combined action of the ON and NeNa cycles in hydrogen burning regions at T > 40 MK, but the mechanism bringing the ashes of hydrogen burning to the surface of stars should be explained. Two main hypotheses have been developed: a deep mixing event

during the RGB phase or the injection in the interstellar medium of nuclearly processed material by polluting stars (see [9] for a review).
Intermediate-mass Asymptotic Giant Branch stars (IM-AGB) are commonly considered to be the best candidates for polluting the early protoclusters via Hot Bottom Burning (HBB) [9]. The AGB phase occurs between the helium burning phase and the ignition of carbon burning. AGB stars consist of a carbon core, an helium burning shell, an hydrogen burning shell and an extended convective envelope (fig. 1.4). In IM-AGB stars with mass higher than 4 solar masses, hydrogen burning occurs at the base of the convective envelope. This process is called hot-bottom burning (HBB) and involves the CNO, NeNa and MgAl cycles at temperatures between 60 and 100 MK [10]. The hydrogen burning products are brought to the surface of the star and then ejected through strong stellar wind, enriching the interstellar medium.
Stellar models trying to reproduce HBB nucleosynthesis require an accurate knowledge of all the nuclear reactions involved. A sensitivity study showed how the uncertainty on the ^{22}Ne(p,γ)^{23}Na cross section propagates to the predicted abundances of neon, sodium and magnesium isotopes [10]. Fig. 1.5 shows that the uncertainty on proton capture on ^{22}Ne produces large variations in the nucleosynthetic output (especially for ^{23}Na, the abundance of which suffers from a factor of 100 uncertainty).

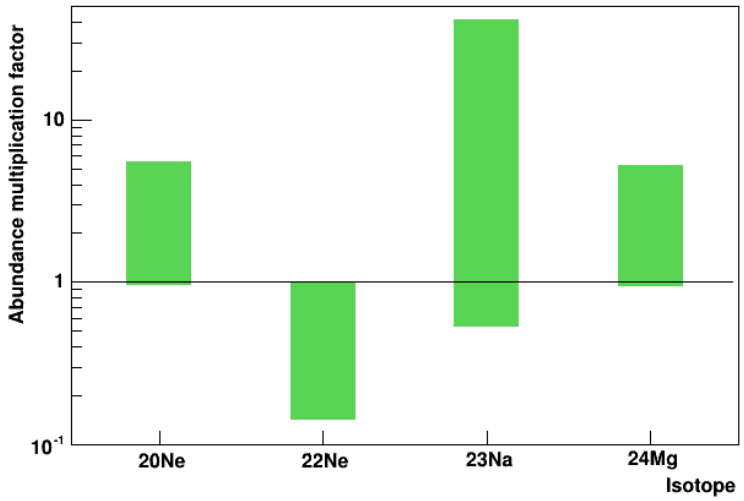

Figure 1.5: Range of uncertainties for the neon, sodium and magnesium yields in IM-AGB during HBB, obtained varying the ^{22}Ne(p,γ)^{23}Na reaction rate within its uncertainty [10]. The yield variations are normalized to the abundances obtained with the recommended reaction rate.

1.2.2 Classical nove and type Ia supernovae

White dwarfs are the last stage of the evolution of low and intermediate mass stars (M $< 13 M_{\odot}$) that develope a degenerate core made of carbon and oxygen (if the last burning stage is helium burning) or neon and oxygen (if the star goes through carbon burning). When a white dwarf is in a close binary system with a

main sequence star, H - rich material can be accreted on the surface of the white dwarf [11].
For large white dwarf masses and accretion rates, the white dwarf mass may increase up to the Chandrasekhar limit (1.4 $M_\odot$) and the ignition of thermonuclear reactions produces a type Ia supernova explosion.
If the acretion rate is smaller than $10^{-8} M_\odot/yr$, the accreted material is gradually compressed and the temperature increases up to the point at which a thermonuclear runaway ignites in the outer layer. As a consequence, the white dwarf envelope is ejected. While in a type Ia supernova the whole white dwarf is destroyed, classical nova explosions only affect the accreted envelope, therefore material can be accreted again on the white dwarf and the explosion may eventually happen repeatedly.
Classical nova explosions are the most common type of stellar outburst (in our Galaxy, a rate of about 35 nova events per year is expected) and are considered important contributors to the chemical evolution of the Galaxy. In a nova outburst peak temperatures between 0.15 and 0.4 GK are achieved. Since during the evolution material from the white dwarf is mixed into the hydrogen rich envelope, the material ejected from classical novae is enriched in the products of the hot CNO cycle and the NeNa and MgAl cycles.
A sensitivity study showed how the abundances of the elements with mass A $<$ 40 in classical novae ejecta are affected by the uncertainty on 175 nuclear reactions [12]. When the white dwarf is made of carbon and oxygen (CO novae), the proton capture on ^{22}Ne significantly affects the abundances of the elements between neon and aluminum (see fig. 1.6). If the white dwarf is made of oxygen and neon (ONe novae), the uncertainty on the ^{22}Ne(p,γ)^{23}Na reaction rate produces a six orders of magnitude uncertainty on the ^{22}Ne yield.

Also in type Ia supernova explosions, where temperatures higher than 1 GK are achieved, the ^{22}Ne(p,γ)^{23}Na reaction rate uncertainty propagates to the nucleosynthetic output predicted by theoretical models.
Type Ia supernovae (SN Ia) are used as standard candles to measure cosmological distances and probe the geometrical structure of the Universe [13]. The light curve of a SN Ia is powered by the decay of radioactive ^{56}Ni produced during the thermonuclear runaway. Nonetheless, theoretical models trying to reproduce the full nucleosynthetic output of SN Ia include a complex nuclear reaction network with thousands of reactions [14].
A sensitivity study recently revealed that an improvement of the ^{22}Ne(p,γ)^{23}Na reaction rate at temperatures above 1.5 GK is necessary to better constrain the yield of ^{18}O, ^{23}Na and ^{24}Na from SN Ia [14].

These results demonstrate the need for new experimental efforts to constrain the ^{22}Ne(p,γ)^{23}Na cross section at center of mass energies between 60 and 160 keV for HBB in AGB stars, between 100 and 440 keV for classical novae and above 375 keV for SN Ia.

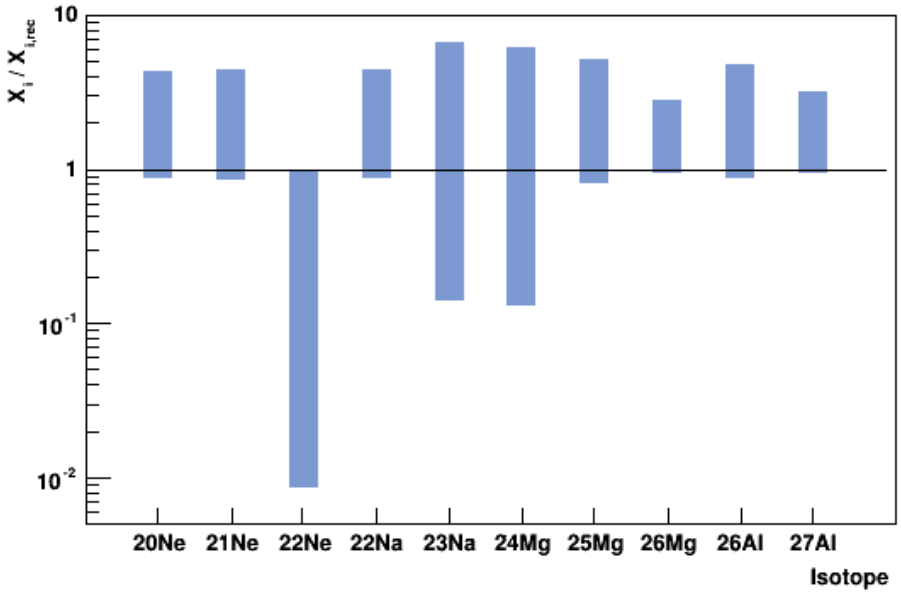

Figure 1.6: Isotopic abundance variations obtained changing the ^{22}Ne(p,γ)^{23}Na reaction rate within its uncertainty [12] in a CO nova model. The yields X_i are normalized to the abundances obtained with the recommended reaction rate $X_{i,rec}$.

1.3 ^{22}Ne(p,γ)^{23}Na reaction rate: state of the art

At astrophysical energies, the ^{22}Ne(p,γ)^{23}Na cross section (Q-value = 8794 keV) is characterized by the contribution of many resonances. Fig. 1.7 shows part of the ^{23}Na level scheme with the entry point of the ^{22}Ne+p reaction and the literature resonance energies in the center of mass system. The energy ranges relevant for hot bottom burning in AGB stars, classical nova and type Ia supernova nucleosynthesis are also displayed.

The literature resonance strengths for the ^{22}Ne+p reaction are summarized in table 1.1 together with the values adopted in the main reaction rate compilations used in astrophysics.

Many experiments have been performed to investigate the levels in fig. 1.7 with indirect techniques, but for many of them there is no clear spin and parity assignment and the gamma decay scheme is also poorly known.
Most of the literature information on the ^{22}Ne+p resonances below 400 keV come from ^{22}Ne(^{3}He,d)^{23}Na experiments [20, 22]. Indirect experiments exploiting proton transfer reactions allow to deduce the partial width of the entrance channel from the spectroscopic factor of the excited state [1, 20]. Once the proton width is known the resonance strength can be calculated with equation 1.14, provided that the level spin is known.
On the other hand, direct experiments allow to derive the resonance strengths from the measured reaction yield with no assumption on the level spin (see sec. 2.2.4). For the ^{22}Ne(p,γ)^{23}Na resonances below 400 keV only one direct measurement is reported in the literature [17] and it shows only upper limits.
The levels at 8862, 8894 and 9000 keV have been tentatively reported in [22] but

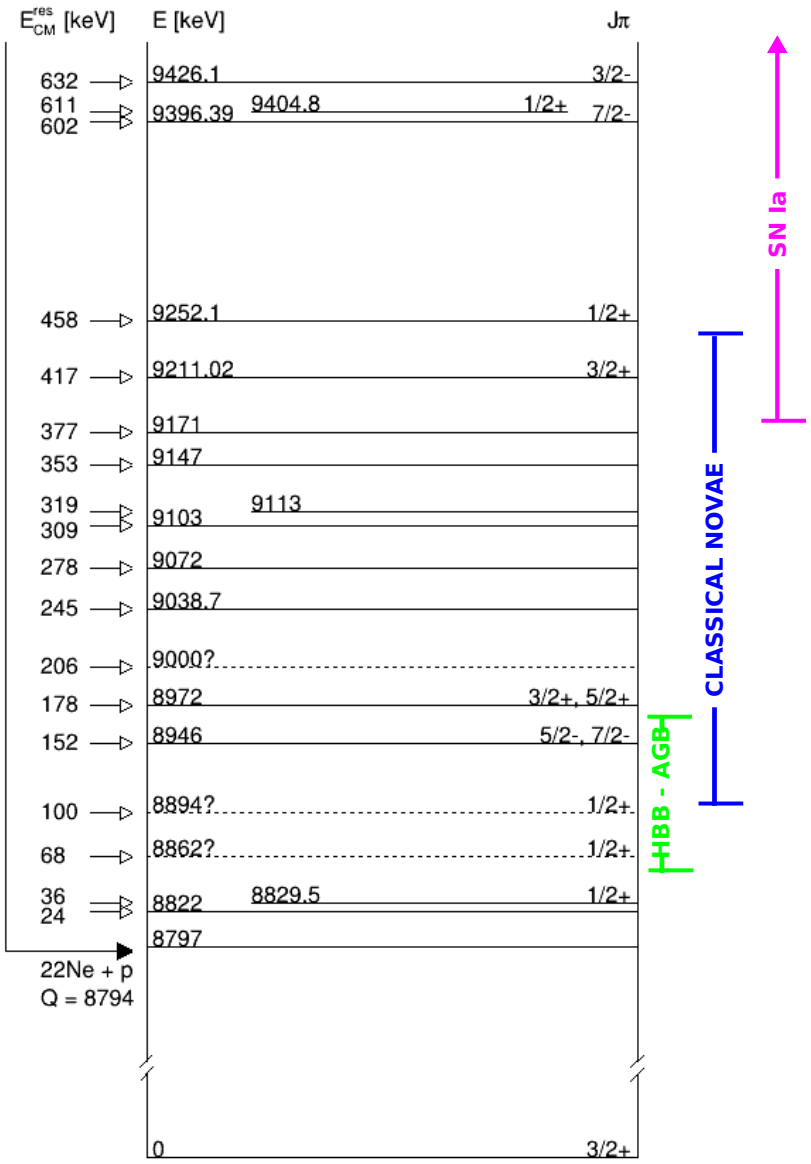

Figure 1.7: Partial level scheme of ^{23}Na. The center of mass energies of the ^{22}Ne+p resonances are reported on the left, while the energy ranges highlighted on the right represent the Gamow windows for hot bottom burning in AGB stars and for classical novae explosions.

E_{res}^{CM} [keV]	E_{res}^{LAB} [keV]	$\omega\gamma$ [eV] NACRE [4]	$\omega\gamma$ [eV] Iliadis et al. [15]
27.9	29	-	$\leq 2.6 \cdot 10^{-25}$ [e]
35.4	37	$(6.8 \pm 1.0) \cdot 10^{-15}$ [a]	$(3.1 \pm 1.2) \cdot 10^{-15}$ [e]
68	71	$\leq 4.2 \cdot 10^{-9}$ [a]	-
100	105	$\leq 6.0 \cdot 10^{-7}$ [b]	-
152	159	$(6.5 \pm 1.9) \cdot 10^{-7}$ [a]	$(9.2 \pm 3.7) \cdot 10^{-9}$ [e]
178	186	$\leq 2.6 \cdot 10^{-6}$ [b]	$\leq 2.6 \cdot 10^{-6}$ [b]
206	215	$\leq 1.4 \cdot 10^{-6}$ [b]	-
245	256	$\leq 2.6 \cdot 10^{-6}$ [b]	$\leq 1.3 \cdot 10^{-6}$ [e]
278	291	$\leq 2.2 \cdot 10^{-6}$ [b]	$\leq 2.2 \cdot 10^{-6}$ [e]
309	323	$\leq 2.2 \cdot 10^{-6}$ [b]	$\leq 2.2 \cdot 10^{-6}$ [e]
319	334	$\leq 3.0 \cdot 10^{-6}$ [b]	$\leq 3.0 \cdot 10^{-6}$ [e]
353	369	-	$\leq 6.0 \cdot 10^{-4}$ [e]
377	394	-	$\leq 6.0 \cdot 10^{-4}$ [e]
417	436	0.07 ± 0.02 [c]	0.065 ± 0.015 [f]
458	479	0.49 ± 0.13 [c,d]	0.45 ± 0.1 [f]
602	630	0.03 ± 0.01 [c]	0.03 ± 0.01 [f]
611	639	2.70 ± 0.25 [c,d]	2.8 ± 0.3 [f]
632	661	0.34 ± 0.09 [c,d]	0.35 ± 0.1 [f]

[a] adopted from [16], indirect data
[b] adopted from [17], direct data
[c] adopted from [18], direct data
[d] adopted from [19], direct data
[e] adopted from [20], indirect data
[f] adopted from [21]

Table 1.1: Summary of ^{22}Ne(p,γ)^{23}Na resonance strengths adopted in the two reference compilations of thermonuclear reaction rates.

have not been observed in the similar and more recent experiment by S. E. Hale at al. [20]. Therefore, those levels are completely disregarded in [5], while an upper limit is quoted in [4].
A very recent experiment by D.G. Jenkins et al. [23] provided some information on both the decay scheme and the spin and parity of some of the ^{23}Na excites states between 8797 and 9171 keV. In this experiment the ^{23}Na excited states were populated by the ^{12}C+^{12}C reaction. No evidence has been found for the levels at 8862, 8894 and 9000 keV, while the 8946 and 9038.7 keV levels are reported as doublets.
The resonances above 400 keV have all been measured in the past (mainly using the intense and well known resonance at 1279 keV as a reference for normalization), but in some cases the uncertainty on the resonance strength is still high (tab. 1.1). Fig. 1.8 shows the contribution of the resonances above 400 keV to the reaction rate. For each resonance, the reaction rate is normalized to the rate adopted by Iliadis et al. [5] and the bands represent the uncertainty due to the error on the $\omega\gamma$.

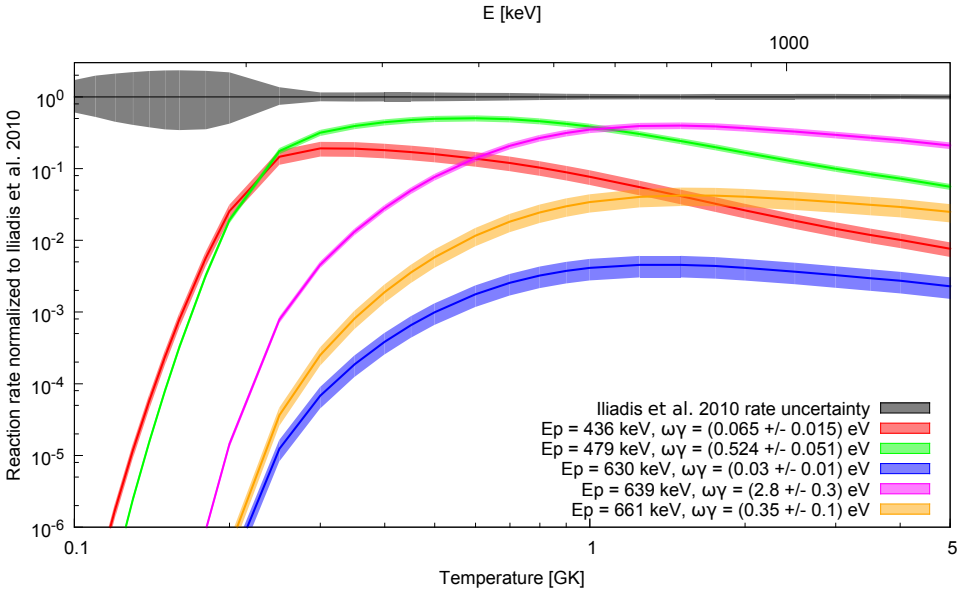

Figure 1.8: Relative contribution to the thermonuclear reaction rate of the resonances between 436 and 661 keV proton energy. The reaction rate for each resonance is normalized to the rate adopted by Iliadis et al. [5]. The bands represent the uncertainty on each contribution.

The resonance at 479 keV has been recently re-measured with 10% accuracy ($\omega\gamma = (0.524 \pm 0.051)$ eV) [24]. The resonances at 436 and 661 keV significantly contribute to the reaction rate, but the uncertainty on the resonance strengths is still at the 20 - 30% level. The resonance at 630 keV is also poorly known, but its contribution to the reaction rate is much smaller than that of the other resonances.

The poor knowledge of the ^{22}Ne+p low-energy resonances translates into high

uncertainties on the reaction rate. Moreover, the different statistical treatment of the upper limits and the choice of the adopted resonances produce orders of magnitude discrepancies in the reaction rates adopted by NACRE and Iliadis et al. (as shown in fig. 1.9).

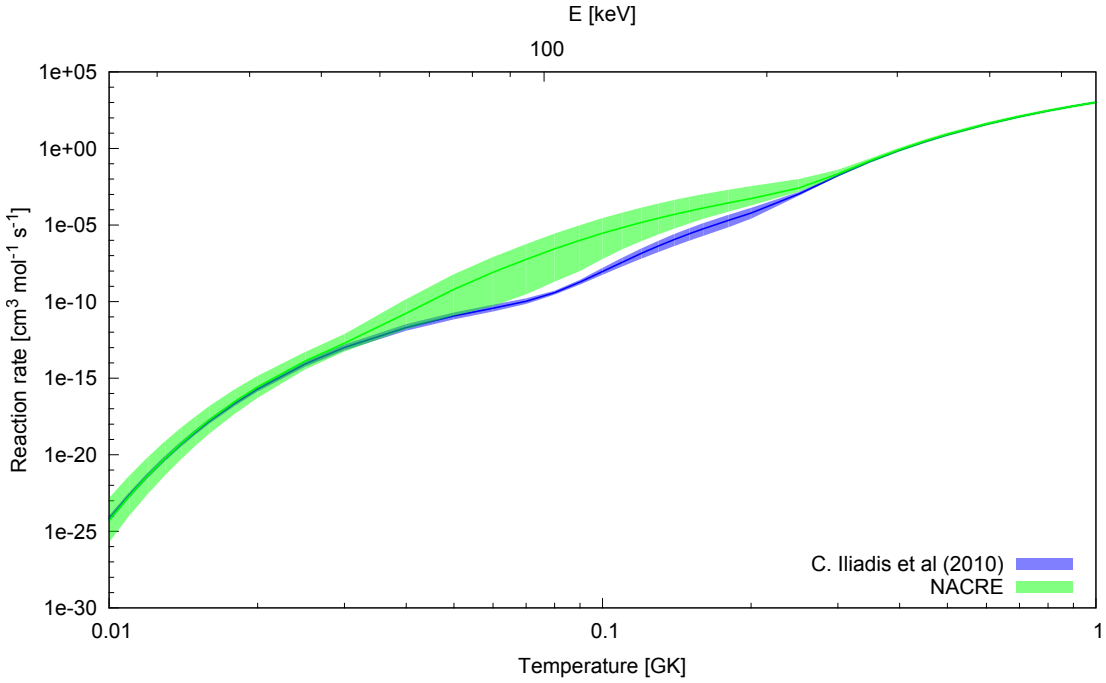

Figure 1.9: Reaction rates reported by NACRE [4] and C. Iliadis at al. [5] for the ^{22}Ne(^{3}He,d)^{23}Na reaction. The maximum discrepancy is about a factor of 700 at 0.08 GK.

In order to reduce the uncertainty on the ^{22}Ne(p,γ)^{23}Na reaction rate, two experiments have been performed in the framework of the present PhD thesis: the resonances below 400 keV have been investigated at the Laboratory for Underground Nuclear Astrophysics (LUNA) in Gran Sasso (see chapter 2), while the resonances at 436, 639 and 661 keV have been measured at Helmholtz-Zentrum Dresden-Rossendorf (HZDR) in Germany (see chapter 3).

Chapter 2

Study of ^{22}Ne(p,γ)^{23}Na low energy resonances at LUNA

Measuring radiative capture cross sections at astrophysical energies is often challenging because the reaction signal can be much smaller than the background in the gamma ray spectrum.
Below 2.6 MeV, the gamma ray background is maily due to the decay of environmental radioactive isotopes (uranium and thorium chains and ^{40}K). This background can be substancially reduced shielding the detector with high Z and high density material (usually lead or copper).
Above 2.6 MeV, the main source of environmental background is cosmic radiation. At sea level, most of the cosmic radiation is made of muons. Muons can either interact inside the detector volume or produce radioactive isotopes and neutrons via spallation, capture or inelastic scattering.
The most efficient way to suppress the muon-induced background is to perform experiments in underground laboratories.
This chapter describes the measurement of the low energy resonances ($E_p < 400$ keV) in the ^{22}Ne(p,γ)^{23}Na reaction performed at the Laboratory for Underground Nuclear Astrophysics (LUNA).

2.1 The LUNA experiment

The Laboratory for Underground Nuclear Astrophysics is located at Gran Sasso National Laboratories (Italy) (see [25] for a review). The laboratory is shielded against cosmic radiation by 1400 meters of rock (3800 meters of water equivalent). This guarantees a six orders of magnitude reduction in the cosmic muon flux and a three orders of magnitude reduction in the neutron flux.
The LUNA experimental apparatus and all preliminary measurements performed to characterize the setup are described in the following sections.

2.1.1 The LUNA 400 kV accelerator

The LUNA experiment is equipped with a 400 kV electrostatic accelerator embedded in a tank filled with an insulating gas mixture composed of N_2 (75%),

CO_2 $(20-25\%)$ and SF_6 $(1-5\%)$ at a pressure of 20 bar [26]. A radio-frequency ion source mounted directly on the accelerator tube provides proton or alpha beams with intensity as high as 500 μA on target. The high voltage (HV) is generated by an Inline-Cockcroft-Walton power supply and is stabilized both by an RC filter at the HV power supply output and by an active feedback loop based on a chain of resistors. The beam energy stability is particularly important for nuclear astrophysics experiments, since the fusion cross section below the Coulomb barrier depends exponentially on the energy. The LUNA proton beam energy is calibrated with 0.3 keV accuracy and has a long term stability of 5 eV/h. The beam energy spread has been measured to be about 100 eV [27].
The ion beam can be delivered to a solid target or to a windowless gas target. A 45° magnet and a vertical steerer guide the beam to the gas target. Optimal beam focusing on the gas target line is obtained minimizing the current on three water cooled collimators of decreasing diameter (see section 2.1.2).

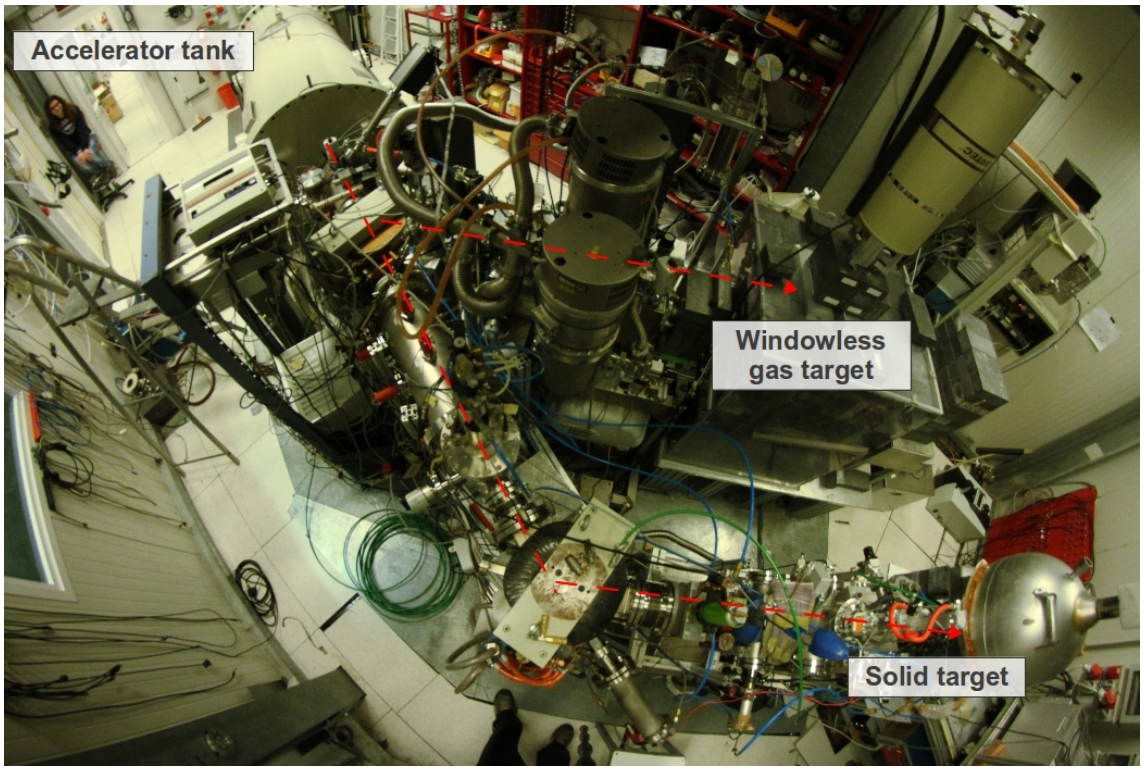

Figure 2.1: Wide angle photo of the LUNA experimental hall.

2.1.2 The gas target system

The use of gas targets provides many advantages compared to solid targets. Indeed, gas targets can be stable over long periods and do not suffer deterioration due to the intense ion beam. Moreover, gas targets can achieve very high isotopical purity, reducing possible beam induced background. On the other hand, measuring nuclear cross sections with extended gas targets requires a precise knowledge of the gas density and detection efficiency along the beam path.

The LUNA experiment is equipped with a windowless gas target. This prevents beam energy loss before entering the target chamber and limits the beam energy straggling.
A scheme of the LUNA gas target is reported in fig. 2.2. The gas enters the target chamber from an inlet tube located on the chamber end flange (right hand side in fig.2.2) . The gas is continuously pumped away from the chamber through three pumping stages that gradually bring the pressure from a few mbar (typical pressure in the target chamber) to the 10^{-7} mbar range (typical pressure in the beam line). The pumping stages are separated by long water cooled apertures of decreasing diameter. The apertures serve both as beam collimators and to increase the impedance for the gas flow from the target to the pumping stages.
The gas taken from the pumping stages can be discharged or recirculated back in the gas target. In recirculation mode, the gas is sent to a Mono Torr II chemical getter suitable for noble gases which removes possible air impurities, and then to a buffer with 1 liter volume. A buffer pressure between 200 and 800 mbar is enough to sustain a target chamber pressure from 0.5 to 5 mbar. When the gas is not recirculated, the target chamber can be fed from a pressurized bottle. Three bottles were always connected to the gas target: enriched ^{22}Ne, neon with natural isotopic composition and nitrogen.
A feedback valve connected to the target chamber inlet regulates the gas flux, keeping the target pressure constant.

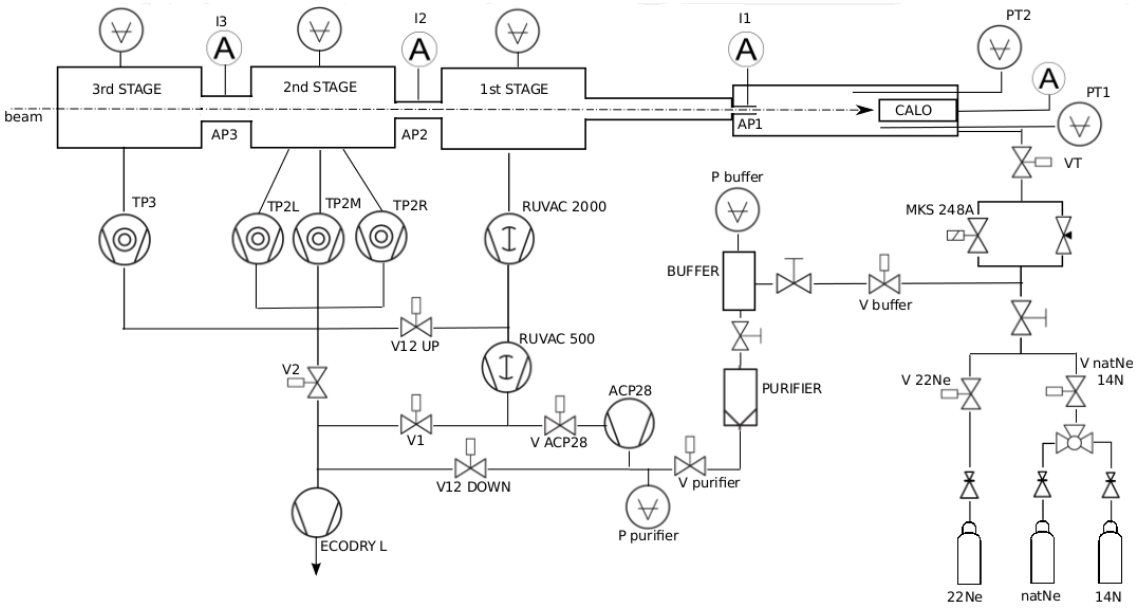

Figure 2.2: Scheme of the LUNA windowless gas target system.

The beam enters the target chamber from the left hand side of fig. 2.2 and is stopped in a copper calorimeter mounted on the chamber end flange. The calorimeter provides an accurate beam current measurement, since the proton beam passing through the gas releases many secondary electrons making the electrical current reading impossible.
The calorimeter is composed of a hot side and a cold side in thermal contact with each other. The hot side is kept at a constant temperature of 70°C by a set of

resistors driven by electrical current, while the cold side is kept at -3°C by an insulating cooling liquid. The temperature of the hot side is measured by five PT100 thermoresistors. A feedback system reads the hot side temperature and adjusts the resistors power in order to keep a constant temperature.
When the beam hits the calorimeter hot side, part of the power needed to keep the 70°C is provided by the beam itself and the power supplied by the resistors decreases.
The power with no beam, called zero power W_0, is recorded on a daily basis over a 10 minutes period keeping the target gas at the same pressure used for the measurement. During both zero power measurement and target irradiation, the resisistors power is logged every two seconds. The beam current is then calculated as follows:

$$I_{beam} = \frac{W_o - W}{E_p - \Delta E} \tag{2.1}$$

where W is the resistors power in presence of the beam, E_p is the proton beam energy at the entrance of the target chamber and ΔE is the total beam energy loss from the target chamber entrance to the calorimeter.
The calorimeter has been calibrated evacuating the target chamber and using the calorimeter and the chamber as a Faraday cup. Throughout the calibration campaign the AP1 collimator was unmounted in order to minimize the production of secondary electrons.
The calibration function is obtained comparing the beam power deduced from the electrical current reading with the power determined from the difference $W_0 - W$. The results are reported in fig. 2.3.

The calibration has been performed both before and after the ^{22}Ne + p data taking. Moreover, at the end of the data taking the calibration was repeated applying a bias voltage of -100 V on the AP1 collimator holder, in order to prevent possible secondary electrons from migrating to the target chamber.
As shown in fig. 2.3, all the data sets lie on the same line, proving that the calibration remained constant over one year and that during the calibration there was no significant production of secondary electrons on the collimator holder. The calorimeter calibration line is:

$$W_{electric} = (0.922 \pm 0.01) W_{calorimeter} \tag{2.2}$$

The plot of residuals in fig. 2.3 shows that for the 80% of the data points the deviation from the fitting line is less than 1%. Therefore a final uncertainty of $\pm 1\%$ on $W_0 - W$ has been adopted for the beam current measurement.

2.1.3 Gas density measurement

The beam energy loss in the target chamber depends on the gas density along the beam path. The gas pressure is always kept at a constant level by the feedback system. On the other hand, the calorimeter hot side and the collimator water cooling introduce a temperature gradient along the target chamber.

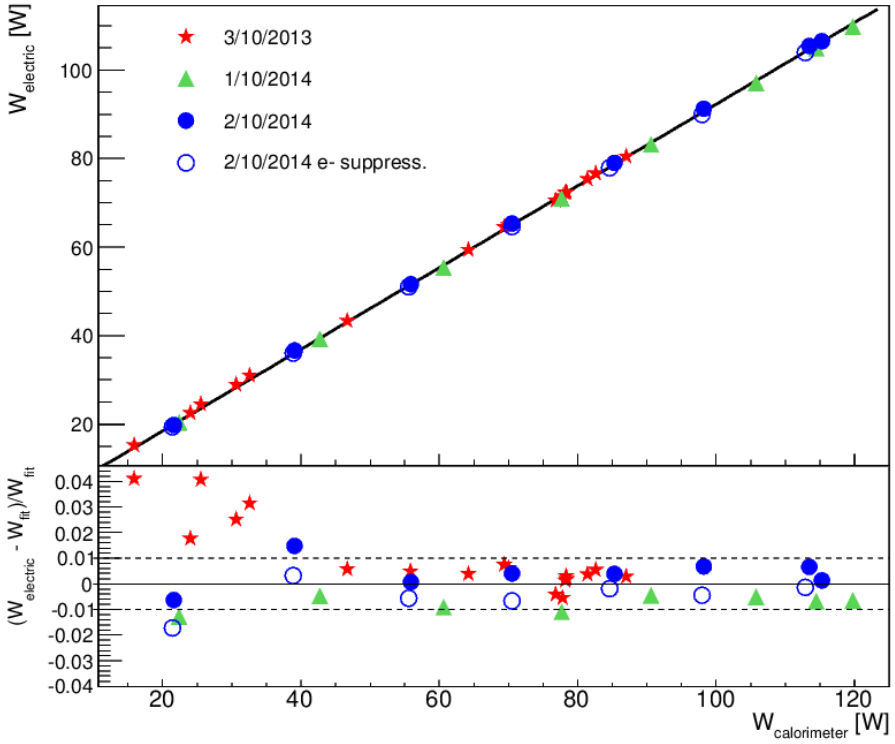

Figure 2.3: Calorimeter calibration function (top) and relative residuals (bottom). The data sets names indicate the date when the calibration was performed. The "02/10/2014 e^- suppress." data set was taken applying -100 V on the AP1 collimator holder.

In order to determine the gas density profile without beam on target and the density reduction due to the beam heating effect, a preliminary set of measurements has been performed using dedicated setups.

Gas density without beam

The gas density profile without beam on target has been deduced from pressure and temperature measurements at different positions along the beam axis. The target chamber used for this purpose has the same geometry as the chamber used for the ^{22}Ne + p study but it is equipped with several flanges to connect pressure or temperature gauges (fig. 2.4).

The gas pressure has been measured with three capacitance manometers: two Pfeiffer manometers with 0.20% accuracy and one MKS manometer with 0.25% accuracy. Another MKS manometer with 0.25% accuracy was connected to the chamber end flange and used as a reference for the feedback system.

One manometer was always mounted on the flange at z = 65 cm, while the other two manometers were moved from run to run in order to cover all possible positions.

The pressure between the AP1 collimator and the calorimeter was found to be constant (fig. 2.5). The variance between the maximum and minimum pressure recorded is always less than the 0.4%. The only exception is the point at 65 cm, which is systematically (1.8 ± 0.5)% lower than the others for all target

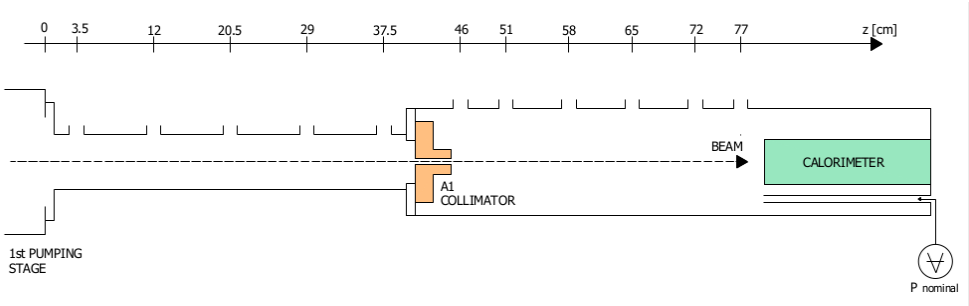

Figure 2.4: Schematic view of the target chamber used for the pressure and temperature profiles measurement. The position of each flange is reported on the top axis.

pressures. We attribute this effect to a misscalibration of the manometer, since this discrepancy was constant in different runs and also moving the manometer to a different position.
Fig. 2.5 also shows that the AP1 collimator produces a pressure drop of about a factor of 30 between the target chamber and the connecting pipe.

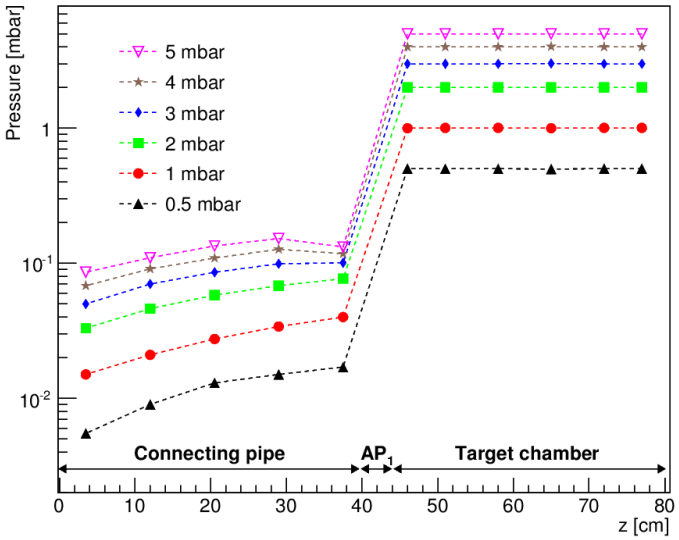

Figure 2.5: Pressure profiles for different target pressures. The dashed lines are just to guide the eye.

The temperature profile has been measured with four resistance temperature detectors PT100 with an accuracy of 0.3 K. An additional uncertainty of 1 K has to be included to take into account the temperature variations observed changing the gauge's orientation, while an uncertainty of 0.5 K accounts for the variations observed repeating the measurement in the same conditions. The resulting temperature profile is shown in fig. 2.6.

The gas temperature increases monotonically from the water cooled AP1 collimator to the calorimeter hot side.
A peculiar behaviour is observed near the calorimeter: for target pressures up to 2 mbar the gas temperature is directly proportional to the target pressure, while

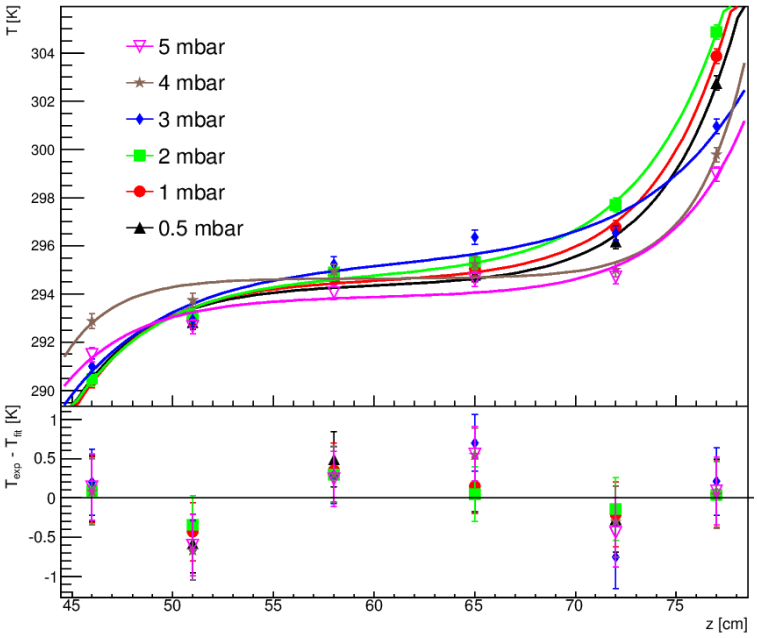

Figure 2.6: Top: temperature profile inside the target chamber for different values of gas pressure. Only statistical errors are reported. Bottom: Fit residuals

Pressure [mbar]	A_0 [K]	A_1 [10^{-3} K]	A_2 [K]	B [1/cm]
0.5	294.4 ± 0.2	1.2 ± 1.1	5.1 ± 0.5	0.28 ± 0.03
1	294.6 ± 0.2	1.8 ± 1.4	5.5 ± 0.5	0.27 ± 0.02
2	294.7 ± 0.2	5.3 ± 3.4	5.5 ± 0.5	0.24 ± 0.02
3	295.2 ± 0.2	10.2 ± 8.8	5.4 ± 0.5	0.20 ± 0.03
4	294.7 ± 0.2	0.01 ± 0.04	2.8 ± 0.5	0.41 ± 0.11
5	293.9 ± 0.2	0.8 ± 1.4	3.3 ± 0.5	0.27 ± 0.05

Table 2.1: Temperature profile fit parameters.

the trend is inverted at higher pressures. This can be interpreted assuming that at low target pressures the heat transport is dominated by conduction. At target pressures around 3 mbar, the heat transfer from the calorimeter hot side becomes more effective because of the onset of forced convection due to the continuous gas flow inside the chamber [28].
Fig. 2.6 also shows the results of the fit of the experimental data with the parametric function

$$T(z) = A_0 + A_1 \cdot e^{B(z-45)} - A_2 \cdot e^{-B(z-45)} \tag{2.3}$$

where the 45 cm offset in the exponentials represents the distance between the beginning of the connecting pipe and the end of the AP1 collimator. The fit parameters and corresponding errors are reported in tab. 2.1.

Combining pressure and temperature measurements through the perfect gas law it is possible to evaluate the gas density profile with 1% uncertainty:

$$\rho = \frac{P}{k_B T} \tag{2.4}$$

where ρ is the gas density, P the pressure, T the temperature and k_B the Boltzmann constant.

Beam heating effect

The gas density along the beam path may decrease because of the interaction with the intense ion beam. This effect, called beam heating, has been already studied in the past for different gases [29–31].
The beam heating in neon has been measured with the resonance scan technique, exploiting the dependency of the beam energy loss on the gas density.
The proton beam energy loss over a distance Δx is given by:

$$\Delta E = \left.\frac{dE}{d(n \cdot x)}\right|_{SRIM} \cdot n \cdot \Delta x \tag{2.5}$$

where n is the gas density in atoms/cm^3 and $\frac{dE}{d(n \cdot x)}$ is the stopping power in eV/(atoms/cm^2) taken from the SRIM database [32]. In presence of the beam only the gas density decreases, therefore the density reduction factor, i.e. the ratio between real and nominal gas density, can be expressed as:

$$\frac{n}{n_0} = \frac{\Delta E}{\Delta E_0} \tag{2.6}$$

where n is the gas density with the beam, n_0 is the nominal gas density (deduced from experimental pressure and temperature profiles with equation 2.4) ΔE is the beam energy loss measured with the beam and ΔE_0 is the energy loss with zero beam current.
The beam heating effect was measured using the same target chamber used for the ^{22}Ne+p study and a (2" x 2") NaI detector. The detector was positioned on a movable table on one side of the chamber and surrounded by a 5 cm thick lead shielding with a 2 cm aperture in front of the detector itself (fig. 2.7).

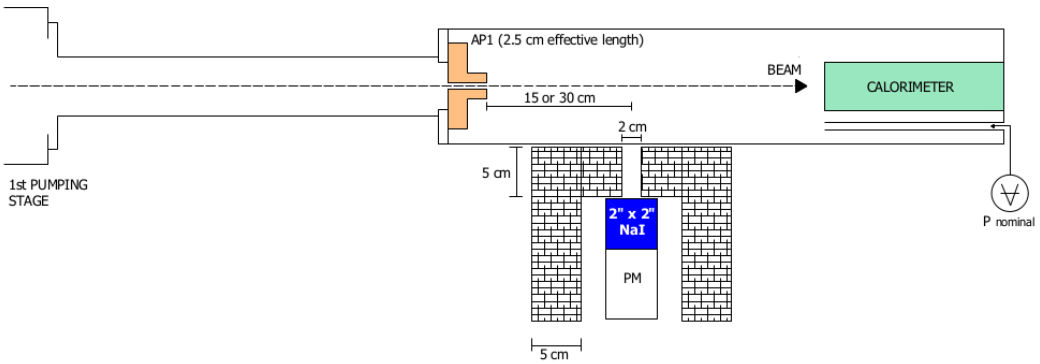

Figure 2.7: Sketch of the setup used for the beam heating measurement.

The beam energy loss was determined scanning the well known narrow resonance of the ^{21}Ne(p,γ)^{22}Na reaction at 271.56 keV [15, 33]. For this purpose, the target chamber was filled with natural neon gas (90.48% ^{20}Ne, 0.27% ^{21}Ne, 9.25% ^{22}Ne) at different pressures and the beam energy was changed in small steps (0.5 to 2 keV, depending on the gas pressure). The maximum yield is obtained when

the reaction is populated in front of the detector.
Fig. 2.8 shows the comparison between a typical NaI spectrum taken on resonance and a spectrum obtained running on the same resonance with an HPGe detector.

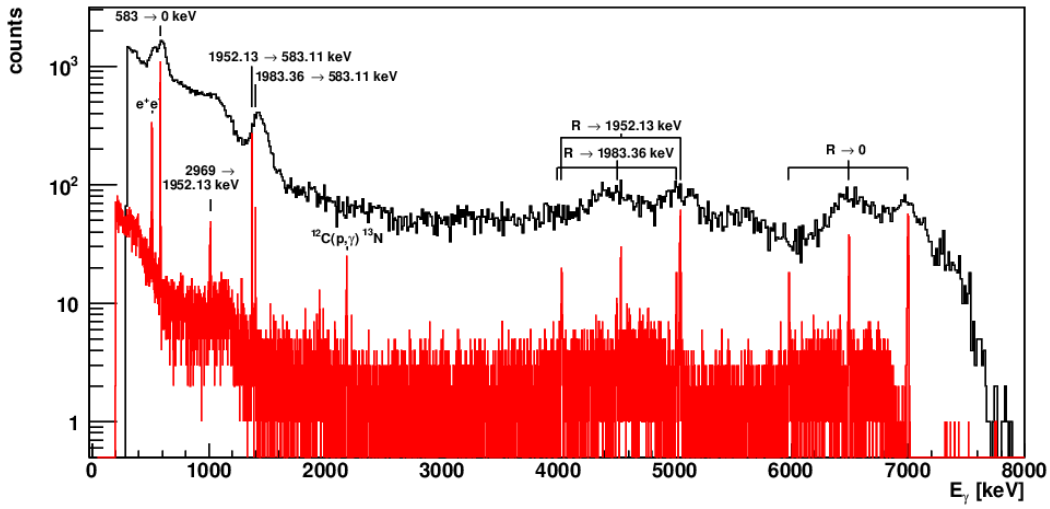

Figure 2.8: Comparison between the spectrum recorded with the collimated NaI detector and an HPGe spectrum over the ^{21}Ne(p,γ)^{22}Na resonance at 271.56 keV.

In order to increase the statistics, the yield has been evaluated integrating the spectrum between 4 and 8 MeV. Typical resonance scans are reported in fig. 2.9. The energy of maximum yield is obtained fitting each curve with a gaussian function.

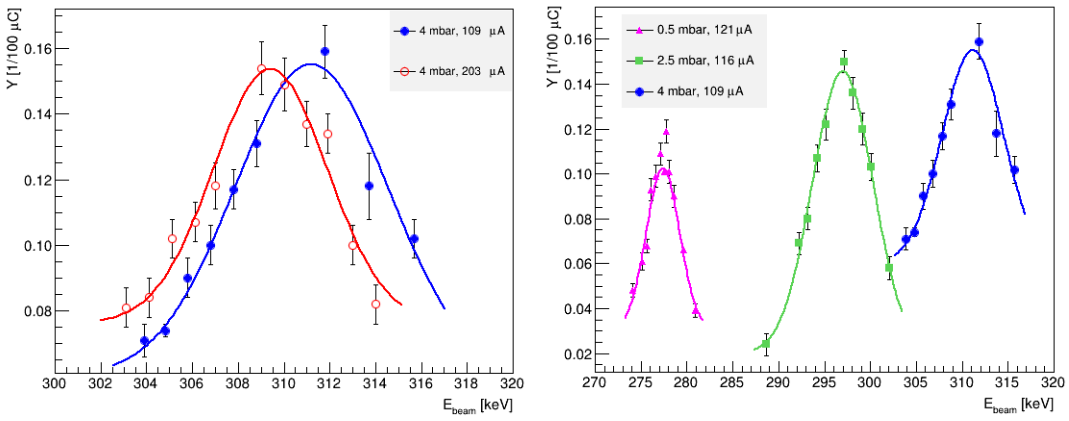

Figure 2.9: Left: scans of the ^{21}Ne(p,γ)^{22}Na resonance at 271.56 keV performed at 4 mbar target pressure with two different beam currents. Right: scans performed at similar beam current and different target pressures.

Resonance scans have been performed at 0.5 mbar, 2.5 mbar and 4 mbar target pressures and, for each pressure, with two different values of beam intensity. Moreover, the measurement was repeated with the NaI detector at 17.5 cm and 32.5 cm effective distance from the target chamber entrance (an effective length

of (2.5 ± 0.5)cm is adopted for the AP1 collimator).
The beam energy loss is calculated as the difference between the energy of maximum yield and the resonance energy:

$$\Delta E = E_{p,max} - E_{res} \tag{2.7}$$

Since the beam heating effect reduces the gas density, the beam energy loss is observed to decrease for increasing beam current (fig. 2.10).

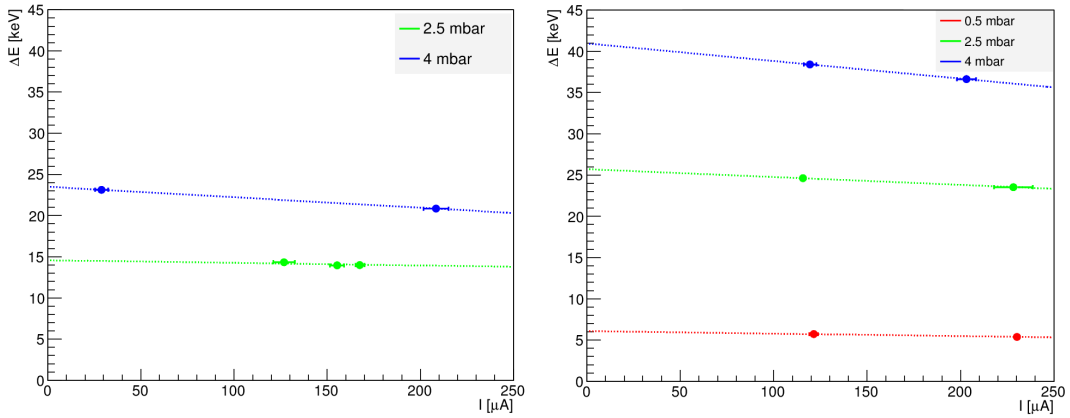

Figure 2.10: Energy loss as a function of the beam current measured with the NaI detector at 17.5 cm (left) and at 32.5 cm (right) from the target chamber entrance.

In order to avoid possible systematic effects due to the positioning of the NaI detector, the energy loss without beam has been evaluated extrapolating the lines in fig. 2.10 to I = 0.
It is known that the the beam heating effect is directly proportional to the power dissipated by the beam per unit length dW/dx [29]:

$$\frac{dW}{dx} = \frac{dE}{d(n \cdot x)} \cdot n \cdot I \tag{2.8}$$

Fig. 2.11 shows the density reduction factor n/n_0 as a function of the beam dissipated power:

The points taken with the detector at 17.5 cm and those taken with the detector at 32.5 cm lie on the same line, therefore they have been fitted together. The line has been bounded to have Y axis intercept equal to one. The beam heating fitting function is:

$$\frac{n}{n_0} = 1 - (0.44 \pm 0.05) \cdot 10^{-3} \frac{dW}{dx} \tag{2.9}$$

where dW/dx is expressed in mW/cm.
The beam heating parameter determined here for proton beam in neon gas has to be compared to $0.5 \cdot 10^{-3}$ for proton beam in nitrogen gas [29,30], and $0.91 \cdot 10^{-3}$ for $^4He^+$ beam in helium gas [31]. The differences may be explained by the different heat transport coefficients in different gases. As a result, the beam heating effect is lower than in previous similar experiments at LUNA but must still be taken into account using eq. 2.11 when determining the final target density.

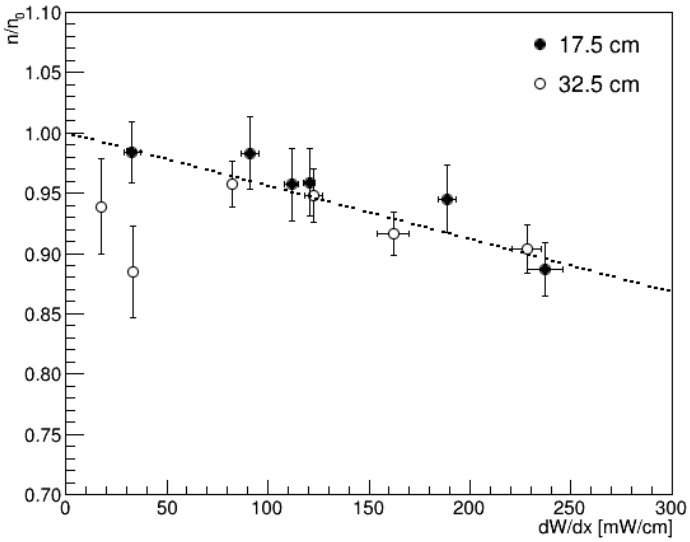

Figure 2.11: Beam heating effect as a function of the beam dissipated power. The points taken with the detector at 17.5 cm (full dots) and 32.5 cm (open circles) are fitted together with a single straight line.

2.1.4 Setup design

The underground location of the LUNA experiment provides about four orders of magnitude background reduction in the gamma ray spectrum above 5 MeV [25,34] (the remaining counts are mainly due to (n,γ) or (n,n'γ) reactions inside the detector). This is particularly important for the study of the ^{22}Ne(p,γ)^{23}Na reaction since, given the 8.79 MeV Q-value, high energy gammas may be emitted in the resonances decay.
At gamma ray energies below 2.6 MeV the background is dominated by environmental radioactivity (^{238}U and ^{232}Th chains and ^{40}K). The background in the low - energy region can be suppressed surrounding the detector with a passive lead shielding. In underground experiments the use of a lead shielding is even more advantageous compared to sea level experiments, since no muon-induced activation is produced inside lead.
The setup used to study the proton capture on ^{22}Ne is illustrated in fig. 2.12.

It consists of two high - purity germanium detectors: a Camberra low backgroung detector with 130% relative efficiency and an Ortec low background detector with 88% relative efficiency.
The 130% detector is collimated at 55° by a 2.8 cm thick lead brick positioned inside the target chamber. This angle has been chosen because at 55° the second order Legendre polynomial $P_2(\cos\theta)$ is zero and possible angular distribution effects (expressed with eq. 2.17) are minimal. The collimator has a truncated cone hole with elliptical bases and with the axis inclined by 45°. With this geometry, the detector line of sight is at 55° with respect to the beam axis. Behind the lead collimator, a 1.6 cm thick tungsten brick shields the 55° detector against possible gamma rays produced on the calorimeter end cap. The 88% detector is

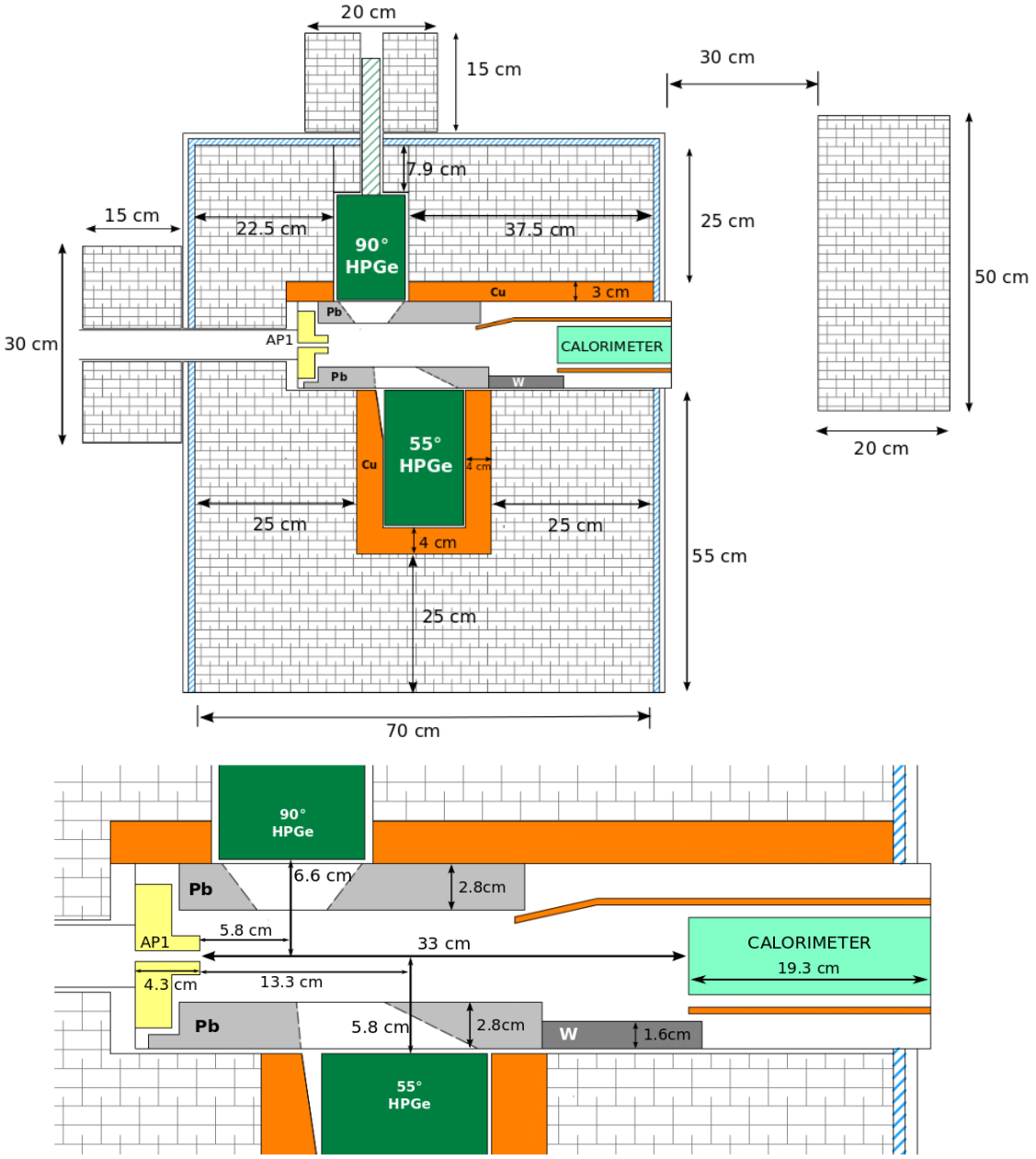

Figure 2.12: Scketch of the experimental setup used for the ^{22}Ne(p,γ)^{23}Na resonances study. The lead and copper shielding dimensions are reported.

collimated at 90° by a 2.8 cm thick lead brick with a truncated cone hole. This brick is positioned in the upper part of the chamber and it is held by a steel support.
The 55° detector is surrounded by a 4 cm thick copper shielding and a 25 cm thick lead shielding. The copper lining shields the detector against bremsstrahlung photons produced in the interaction of electrons emitted in ^{210}Bi beta decay inside lead. ^{210}Bi is the daughter of ^{210}Pb, a radioactive isotope usually present in lead. The 90° detector is only shielded with lead.
The lead castle is enclosed in a plexiglass radon box (cyan dashed lines in fig. 2.12) that prevents radon gas accumulation around the detectors flushing inside the castle the nitrogen exaust from the 55° detector dewar. The radon box also creates a nitrogen overpressure around the castle, preventing radon entering from outside.
The external lead wall on the right hand side of fig. 2.12 shields the detectors from gamma rays that may enter the target chamber through the end-flange. The lead layer between the chamber and the first pumping stage reinforces the detectors shielding against gamma rays that may be produced when the beam hits the AP2 collimator.
The 55° detector shielding is the same adopted for the ^{3}He(^{4}He,γ)^{7}Be cross section measurement, providing the lowest background conditions achieved at LUNA [35]. However, an opening in the shielding had to be introduced to place the second detector. In order to estimate the effect of the introduction of the second detector on the background, Geant4 simulations of the experimental setup have been developed during the design phase. Geant 4 simulations have also been used to define the optimal position for the 90° detector, that is to find the configuration in which the two detectors "see" the same target region.
The environmental radioactivity sources have been treated in an approximate way. Spherical, uniformly distributed sources with 2 meters radius centered on the 55° detector endcap have been simulated. Moreover the ^{238}U, ^{232}Th and ^{40}K sources have been simulated independently. Fig 2.13 shows the sum of simulated ^{238}U, ^{232}Th and ^{40}K spectra for both the single detector setup (*i.e.* the ^{3}He+^{4}He setup) and the two detectors configuration. For each radioactive source, $8 \cdot 10^{8}$ gamma emissions have been simulated.

Since the background suppression depends on the gamma ray energy and each source emits gammas with different energies, the proportions between ^{238}U, ^{232}Th and ^{40}K in the LUNA hall have been estimated using one gamma ray line for each source, namely the 609 keV, 2615 keV and 1461 keV gammas. The peak areas in a real and simulated spectrum without lead shielding have been compared to obtain the weights:

$$w_i = \frac{A_i^{Exp}}{A_i^{Sim}} \tag{2.10}$$

where A_i^{Exp} is the peak area in the experimental spectrum and A_i^{Sim} is the peak area in the simulated spectrum. All isotopes have been simulated with the same number of gamma emissions and the most intense gammas from each decay chain have been simulated with their branching ratios.
For each radioactive source, the background deterioration due to the inclusion

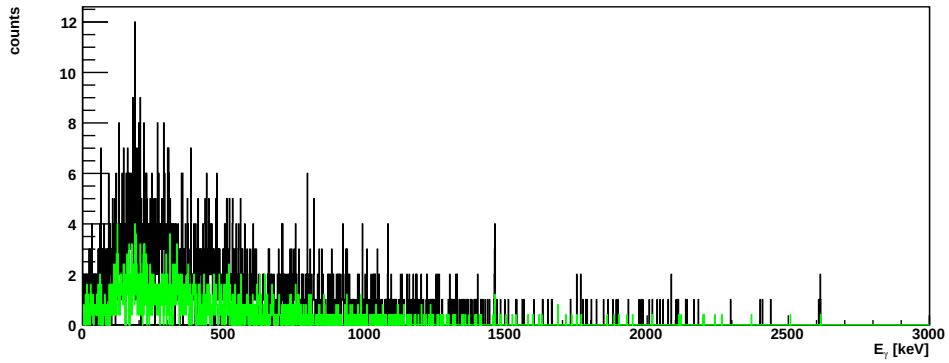

Figure 2.13: Sum of simulated ^{238}U, ^{232}Th and ^{40}K spectra for the single detector setup (green) and for the two detectors configuration (black).

of the second detector in the setup has been estimated integrating the whole simulated spectrum and dividing the integral I_j obtained for the two detectors configuration by the integral for the single detector configuration (see table 2.2). The average background ratio has then been calculated as follows:

$$< R >= \frac{\sum_{j=K,U,Th} I_j w_j}{\sum_{j=K,U,Th} w_j} \tag{2.11}$$

	w_j	I_j Single detector	I_j Two detectors	Ratio
^{40}K	67	306 ± 17	862 ± 29	2.8 ± 0.1
^{238}U	27	128 ± 11	416 ± 20	3.2 ± 0.2
^{232}Th	58	161 ± 13	446 ± 21	2.8 ± 0.1
$< R >$				3.0 ± 0.2

Table 2.2: Simulated background deterioration due to the inclusion, inside the lead shielding, of a second detector in the setup C of [35]. The third and fourth columns show the integrals of the spectra obtained in the single detector and in the two detectors configurations, respectively. The ratio between the two detectors and the one detector areas is reported in the last column.

Table 2.2 shows that the background with two shielded detectors is expected to be three times worse than the background with one detector only.
Fig. 2.14 shows the comparison between experimental background spectra taken with the 55° detector unshielded, in the ^{3}He+^{4}He configuration and in the ^{22}Ne+p experimental setup. The real background deterioration between the single detector and the two detectors configurations has been found to be a factor of 2.77 ± 0.05. This factor is calculated as the ratio between the total areas under the red and the blue spectra in fig. 2.14.

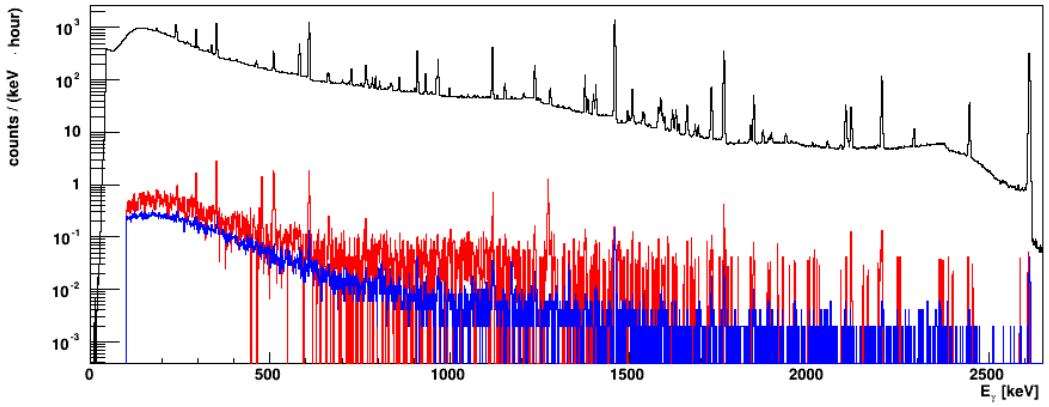

Figure 2.14: Experimental background spectra acquired with the 55° detector unshielded (black) in the single detector shielding (blue) and in the two detectors shielding (red) configurations.

Fig 2.15 shows the 55° and 90° detectors background spectra in the ^{22}Ne+p setup. The most intense gamma ray lines are those emitted in the decay of ^{214}Pb and ^{214}Bi, daughters of ^{222}Rn. Given the complexity of the setup and the many openings needed to insert the setup components in the radon box, a leak in the radon box sealing may be the origin of the radon background.
^{7}Be and ^{22}Na lines are also visible in the spectra. ^{7}Be ($T_{1/2} = 53$ days) is produced by the ^{10}B(p,α)^{7}Be reaction if ^{10}B contamination is present in the setup. ^{22}Na ($T_{1/2} = 2.6$ years) was produced with the ^{21}Ne(p,γ)^{22}Na reaction during the beam heating measurement.

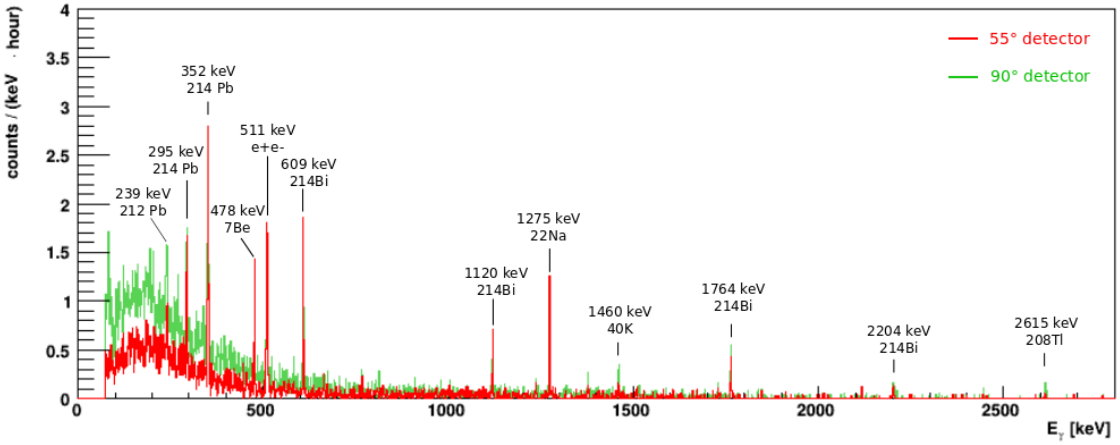

Figure 2.15: Comparison between experimental background spectra in the 55° detector (red) and the background in the 90° detector (green).

As shown in fig. 2.12, the two detectors are positioned 7.5 cm apart along the beam direction. This was found to be the optimal distance for the two detectors to look at the same region of the target chamber.
The detectors alignment has been designed using Geant4 simulations: the fully shielded geometry has been simulated with the 90° detector at different positions

along the beam axis. For each detector position, a ^{137}Cs point-like source emitting gamma rays with an isotropical angular distribution has been simulated. The source has been moved along the beam axis in 5 mm steps, and for each position $2 \cdot 10^7$ gamma emissions have been simulated.
The simulated yield profiles as a function of the source position are reported in fig. 2.16 for the final detectors configuration. The x = 0 coordinate corresponds to the center of the 55° detector. The shape of the two yield profiles is different because of the different collimation geometry, but it is shown that when the 90° detector is positioned 7.5 cm away from the 55° detector in the AP1 direction, the two detectors have the maximum efficiency in the same target region. In the adopted configuration, the hole at the lower end of the 90° detector collimator has 5.1 cm diameter, while the hole at the upper end has 7.0 cm diameter. With this setup, the simulated yield profiles have about the same full width at half maximum.

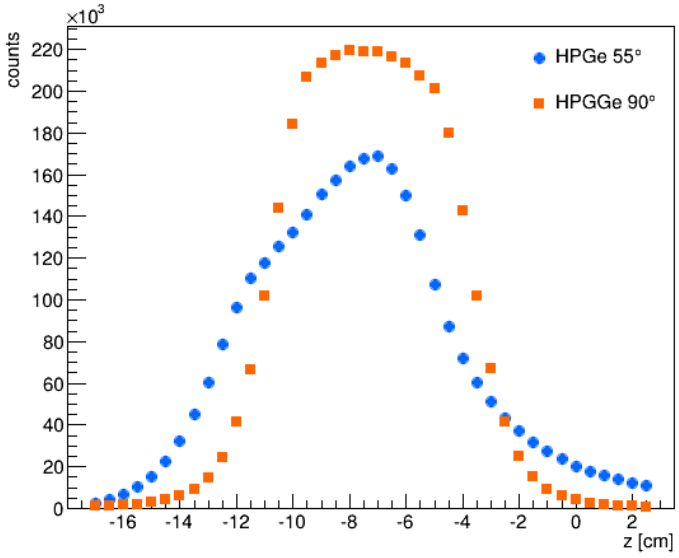

Figure 2.16: Simulated yield profiles obtained moving a point-like ^{137}Cs source along the beam axis.

Two parallel data acquisition systems have been used. A scheme is reported in fig 2.17. The CAEN digital acquisition can be used to store the single events recorded by the two detectors in list mode configuration. For each event, the corresponding energy, time stamp and a pileup flag are recorded. The events can then be sorted off-line, allowing for example to analize coincident events in the two detectors. On the other hand, the EtherNIM analog multichannel analizer provides directly the detectors spectra. The dead time recorded by the analog data acquisition was always at the 1% level or lower.

2.1.5 Detection efficiency

The absolute full-energy peak efficiency is defined as the ratio between the measured peak area and the number of gammas emitted at the same energy in the

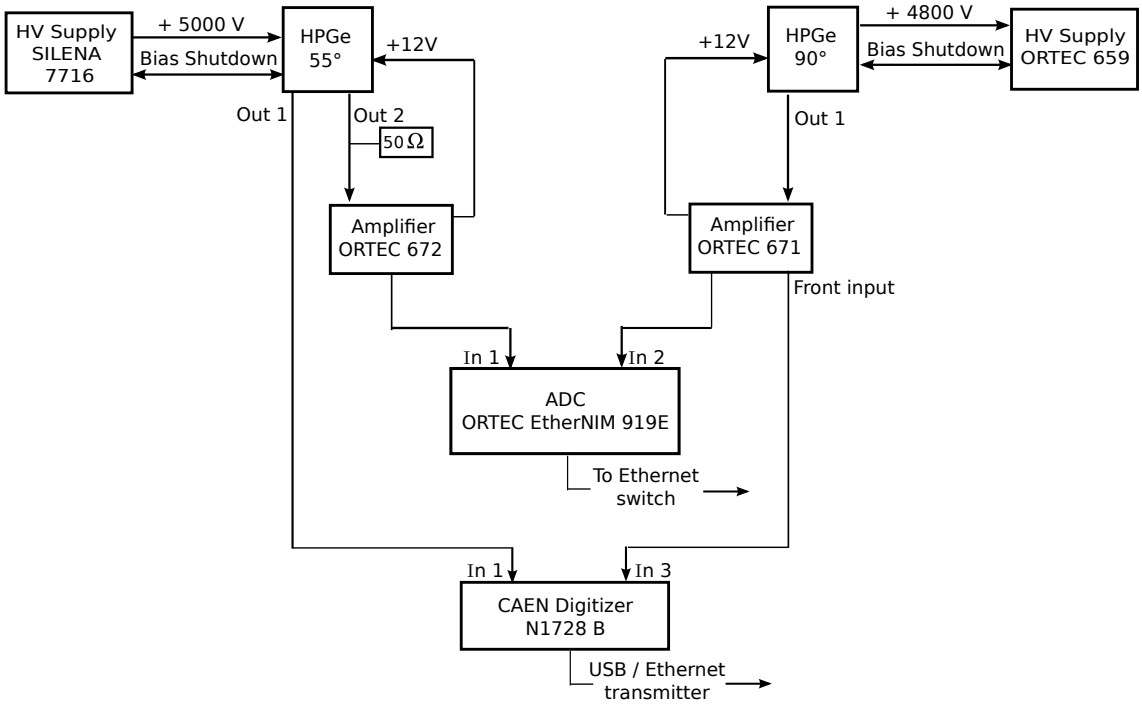

Figure 2.17: Scheme of the data acquisition system adopted for the ^{22}Ne+p experiment at LUNA.

whole solid angle by a radioactive nuclide. It can be determined as:

$$\eta(E) = \frac{N(E)}{A \cdot t \cdot Br} \tag{2.12}$$

where N(E) is the number of counts in the peak at energy E, A is the source activity, t is the measuring time and Br is the transition branching ratio.
Given the 8.79 MeV Q-value of the ^{22}Ne+p reaction, the de-excitation of ^{23}Na may produce high energy gamma rays. On the other hand, the gamma decay modes of the excited states investigated at LUNA are not known, and the most intense transition expected in the gamma ray spectrum is the 440 keV gamma emitted in the decay of the first excited state in ^{23}Na. Indeed, the first excited state is expected to collect most of the statistics from the decay of the higher energy states. Therefore, the detection efficiency should be measured in the widest possible energy range.
The detection efficiency as a function of the position along the beam axis has been measured with four point-like radioactive sources: ^{7}Be, ^{137}Cs, ^{60}Co and ^{88}Y. The main characteristics of each source are summarized in tables 2.3 and 2.4.

A special source holder was designed for the efficiency measurement. The holder consists of a central PVC frame with two lateral wings designed to hold the source at the same height as the center of the AP1 collimator. The frame is mostly empty to avoid gamma absorption. The frame is connected to two rods: a cylindrical rod moving inside the AP1 collimator and, on the opposite side, a rectangular rod. The rectangular rod fits in a specific flange that keeps it alligned, preventing the source holder from rotating around the beam axis. The end flange is 8 cm thick in order to maximize the stability of the rectangular rod against

Source	E_γ [keV]	Branching [%]	Ref.
^{7}Be	477.6	10.44 ± 0.04	[36]
^{137}Cs	661.66	85.0 ± 0.2	[37]
^{60}Co	1173.23	99.85 ± 0.03	[38]
	1332.49	99.9826 ± 0.0006	
^{88}Y	898.04	94.0 ± 0.3	[39]
	1836.06	99.4 ± 0.3	

Table 2.3: List of most intense gamma rays emitted in the decay of the radioactive sources used for the efficiency measurement. For ^{88}Y, the branching ration are those adopted by the source producer to calculate the source activity.

Source	$T_{1/2}$ [y]	Activity [kBq]	Ref. Date	Activity (t) [kBq]
^{7}Be	0.14571 ± 0.00016	113.6 ± 1.6	18/04/2014 15:00	64.6 ± 0.9
^{137}Cs	30.08 ± 0.09	11.30 ± 0.06	01/01/2005	9.10 ± 0.05
^{60}Co	5.2711 ± 0.0004	9.12 ± 0.04	01/01/2005	2.65 ± 0.01
^{88}Y	0.29193 ± 0.00006	36.8 ± 0.4	01/04/2014	24.8 ± 0.3

Table 2.4: Half life, activity at the reference date (provided by the source producer) and activity at the efficiency measurement date.

vibrations. A photo of the source holder is shown in fig. 2.18.

Fig. 2.19 shows the experimental efficiency profile as a function of the source distance from the AP1 collimator, measured with the ^{137}Cs source. The plots confirm that the two detectors "see" with maximum efficiency the same target region. Similar curves have been obtained for all radioactive sources.

Fig. 2.20 shows, for each detector, the efficiency as a function of the gamma ray energy measured with radioactive sources.

The curve has been fitted with a line in the double logarithmic plane:

$$\eta(E) = exp(a + b \cdot ln(E)) \tag{2.13}$$

The fitting lines are also shown in fig. 2.20 together with the fit residuals. The fit parameters and the reduced χ^2 (*i.e.* the χ^2 divided by the number of degrees of freedom) are reported in table 2.5.

The efficiency curve has been extended up to 6.79 MeV using the well known intense resonance at 278 keV in the ^{14}N(p,γ)^{15}O reaction [40]. For this purpose,

Detector	a	b	χ^2/d.o.f.
HPGe 55°	2.71 ± 0.08	-0.43 ± 0.01	2.9
HPGe 90°	4.28 ± 0.08	-0.65 ± 0.01	1.2

Table 2.5: Fitting parameters for the efficiency curve measured with radioactive sources. The chi-squared divided by the number of degrees of freedom (d.o.f.) is also reported.

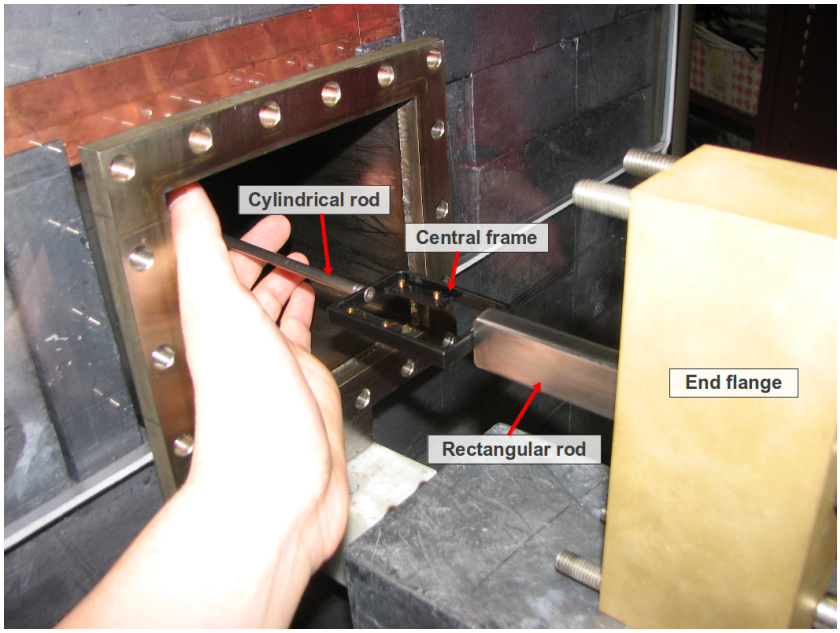

Figure 2.18: Photo taken during the mounting of the source holder for the efficiency measurement. All components are indicated.

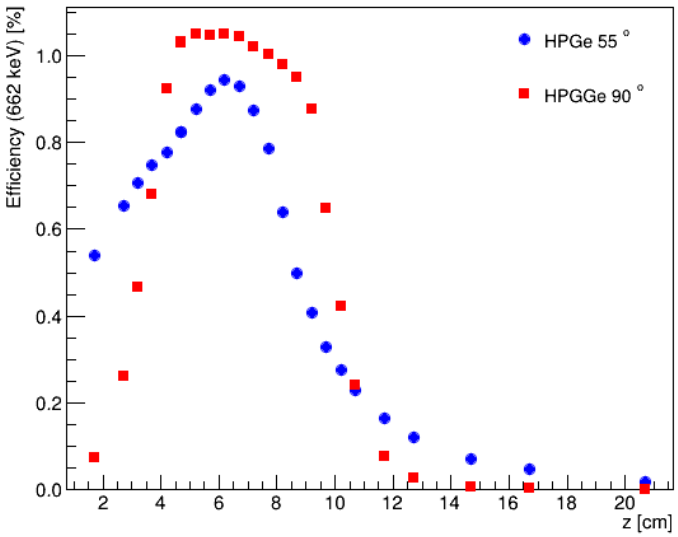

Figure 2.19: Efficiency as a function of the distance from the AP1 collimator measured moving a ^{137}Cs source along the beam axis.

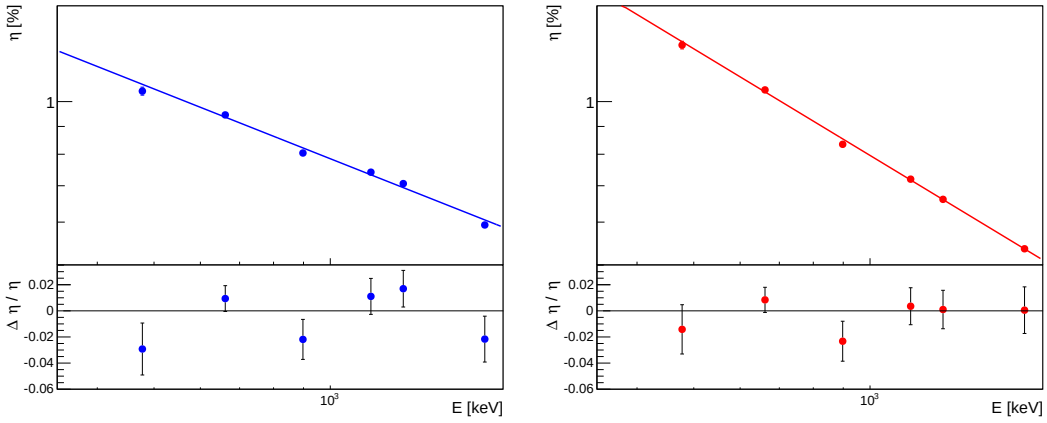

Figure 2.20: Efficiency as a function of the gamma ray energy for the 55° detector (left) and for the 90° detector (right). The fitting function and residuals are also shown.

the target chamber was filled with nitrogen gas at a pressure of 3.6 mbar. The resonance excitation function was obtained changing the beam energy in 1 keV steps. A long run was then performed at the beam energy of maximum yield. The yield prfiles obtained at different gamma ray energies are shown in fig. 2.21.

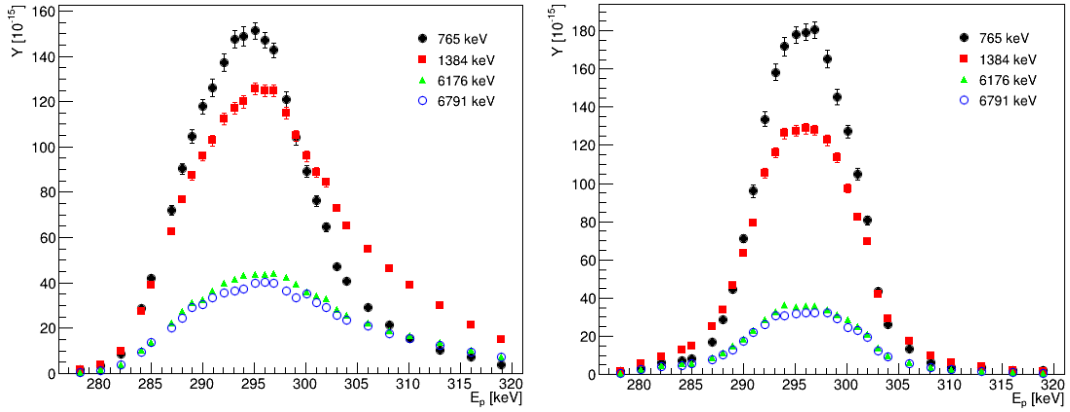

Figure 2.21: Yield profiles for different gamma rays emitted in the ^{14}N(p,γ)^{15}O reaction. The left plot shows the results for the 55° detector while the right plot refers to the 90° detector. The data are not corrected for summing-out.

The detection efficiency for high energy gamma rays was then derived using a relative method: the resonance decays through four different cascades [40]. A 1384 keV and a 765 keV gamma ray de-excite the nucleus to the 6171 and 6790 keV levels respectively. The 6171 and 6790 keV levels decay to the gound state with 100% branching. Therefore an high energy gamma is accompained by a gamma ray in the energy range covered by the radioactive sources and the two gammas have the same branching ratio. The detection efficiency for the high energy gammas can then be evaluated as follows:

$$\eta(E'') = \eta^{fit}(E') \cdot \frac{N_{E''}}{N_{E'}} \tag{2.14}$$

Detector	a	b	c	χ^2/d.o.f.
HPGe 55°	-2.7 ± 0.5	1.2 ± 0.1	-0.116 ± 0.009	3.5
HPGe 90°	0.45 ± 0.5	0.48 ± 0.14	-0.083 ± 0.009	2.9

Table 2.6: Fitting parameters for the complete efficiency curve.

where $\eta(E'')$ is the efficiency for the high energy gamma, $\eta^{fit}(E')$ is the efficiency for the corresponding low energy gamma deduced from the fit of the efficiency curve in fig. 2.20, $N_{E''}$ and $N_{E'}$ are the number of counts in the gamma ray spectrum for the high energy and for the low energy transition, respectively. The complete efficiency curves as a function of the gamma ray energy are shown in fig. 2.22.

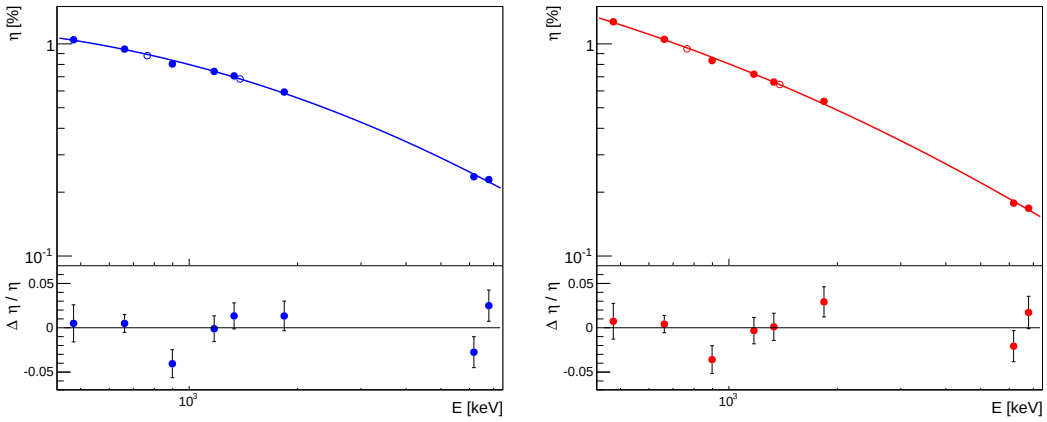

Figure 2.22: Efficiency as a function of the gamma ray energy for the 55° detector (left) and for the 90° detector (right). Open circles represent the efficiency for the 765 keV and for the 1384 keV gammas and are excluded from the fit. The fitting function and residuals are also shown.

The data have been fitted with a second order polynomial in the double logarithmic plane:

$$\eta(E) = exp(a + b \cdot ln(E) + c \cdot ln^2(E)) \tag{2.15}$$

The fit parameters are reported in table 2.6.

Summing-out correction

Radioactive isotopes often decay emitting two (or more) gamma rays in cascade. If the lifetime of the individual nuclear levels is shorter than the resolving time of the gamma ray detector, the two gamma rays may both reach the spectrometer and be detected together. The summing-out effect entails a loss of counts from the full energy peak and the probability increases when the detector is in close geometry.

The number of events lost from the full-energy peak can be expressed as the joined probability of one gamma being detected with its total energy and the coincident gamma being detected anywhere in the spectrum (including the compton shoulder

and the first and second escapes). Therefore, the number of events recorded in the full-energy peak can be expressed as:

$$N_1 = A \cdot Br_1 \cdot \eta_1 - A \cdot Br_1 \cdot \eta_1 \cdot \eta_{T,2} \cdot W(0) \tag{2.16}$$

where N_1 is the number of counts in the full energy peak for one transition, A is the number of source decays in the measuring time, Br_1 is the probability of de-excitation producing that gamma, η_1 is the full-energy peak efficiency for the first gamma, $\eta_{T,2}$ is the probability of the coincident gamma being detected and appearing at any energy in the gamma ray spectrum.
W(0) represents the probability of the two gamma rays being emitted in the same direction. Indeed, when a nucleus decays emitting two gamma rays in succession, the direction of emission of the two gamma rays may be correlated. The probability that two consecutive gamma rays are emitted at an angle θ can be expressed as a sum of Legendre polynomials:

$$W(\theta) = 1 + a_2 Q_2 P_2(cos\theta) + a_4 Q_4 P_4(cos\theta) \tag{2.17}$$

where P_2 and P_4 are the Legendre polynomials, a_2 and a_4 are the angular correlation coefficients typical for each decay cascade, Q_2 and Q_4 are attenuation factors introduced to take into account the finite solid angle occupied by the detector.
The efficiencies measured with ^{60}Co and ^{88}Y sources and with the ^{14}N(p,γ)^{15}O reaction have been calculated taking into account the summing out effect. In particular, the detection efficiency can be deduced from eq. 2.16:

$$\eta_1 = \frac{N_1}{A \cdot Br_1 \cdot (1 - \eta_{T,2} \cdot W(0))} \tag{2.18}$$

For ^{60}Co and ^{88}Y, theoretical angular correlation coefficients have been adopted [41] while for ^{15}O the coefficients have been taken from reference [42]. The attenuation factors have been evaluated for both detectors using the method described in [43]. Q_2 is 0.81 (0.74) for HPGe 55° (HPGe 90°) while Q_4 is 0.43 (0.26).
The total detection efficiency $\eta_{T,i}$ has been evaluated using Geant 4 simulations. As a first step, all radioactive sources have been simulated in order to verify that the shape of the experimental spectrum was correctly reproduced and that the simulated peak-to-total ratio was comparable with the experimental one.
The comparison between experimental and simulated ^{137}Cs spectra is shown in fig 2.23, while tables 2.7 and 2.8 report experimental and simulated peak-to-total ratios for all radioactive sources and the relative discrepancy between the two. For non monochromatic sources, the peak-to-total is calculated as the sum of the two peak areas divided by the total area under the spectrum.

Then individual point-like sources emitting a single gamma ray of the energy of interest has been simulated and the total detection efficiency has been evaluated as the ratio between the experimental photopeak efficiency and the simulated peak-to-total ratio:

$$\eta_{T,i} = \frac{\eta_1^{exp}}{P/T^{sim}} \tag{2.19}$$

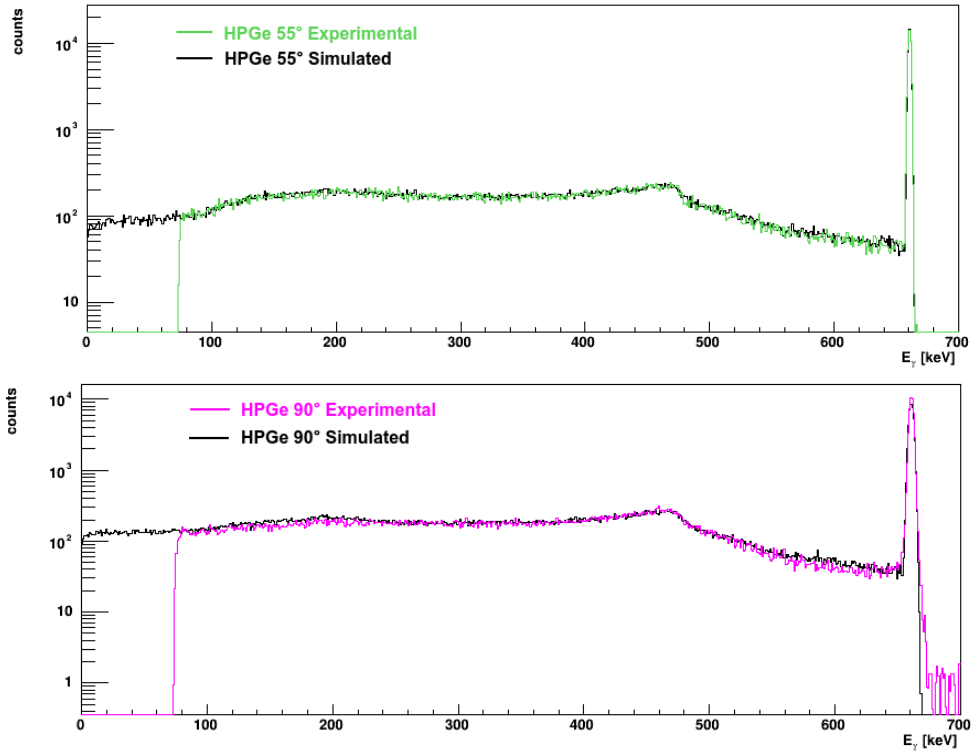

Figure 2.23: Comparison between simulated and experimental ^{137}Cs spectra for the 55° detector (up) and for the 90° detector (down). The two apectra are normalized by the total area.

Source	P/T$_{exp}$	P/T$_{sim}$	(P/T$_{exp}$ - P/T$_{sim}$)/ P/T$_{exp}$
^{7}Be	0.390 ± 0.004	0.377 ± 0.02	3.3%
^{137}Cs	0.329 ± 0.002	0.317 ± 0.001	3.5%
^{60}Co	0.232 ± 0.002	0.229 ± 0.001	1.4%
^{88}Y	0.223 ± 0.001	0.225 ± 0.001	-0.9%

Table 2.7: Comparison between experimental and simulated peak-to-total ratios for the 55° detector

Source	P/T$_{exp}$	P/T$_{sim}$	(P/T$_{exp}$ - P/T$_{sim}$)/ P/T$_{exp}$
^{7}Be	0.426 ± 0.004	0.380 ± 0.01	10.7%
^{137}Cs	0.343 ± 0.002	0.308 ± 0.001	10.2%
^{60}Co	0.231 ± 0.002	0.216 ± 0.001	6.5%
^{88}Y	0.230 ± 0.001	0.216 ± 0.001	6.0%

Table 2.8: Comparison between experimental and simulated peak-to-total ratios for the 90° detector

In this approach, the experimental photopeak efficiency (which is the quantity to be corrected) enters the summing out correction itself. The degeneracy can be removed using equations 2.19 and 2.18 iteratively. One iteration has been proved to be enough to converge.
Table 2.9 reports the simulated peak-to-total ratio, the experimental photopeak efficiency and the total efficiency for all gamma rays affected by summing-out. A conservative uncertainty of ±20% on the summing-out correction has been adopted. The summing out correction is always between the 2.8% and the 4%.

	HPGe 55°			HPGe 90°		
E_γ [keV]	P/T_{sim}	η [%]	η_T [%]	P/T_{sim}	η [%]	η_T [%]
1173	0.23	0.72	3.16	0.21	0.69	3.30
1332.5	0.21	0.68	3.20	0.20	0.64	3.22
898	0.26	0.78	3.05	0.24	0.81	3.37
1836	0.18	0.58	3.20	0.16	0.52	3.17
1384	0.21	0.68	3.27	0.19	0.64	3.34
6171	0.06	0.24	3.93	0.05	0.18	3.98
765	0.28	0.88	3.19	0.26	0.98	3.64
6792	0.05	0.23	4.35	0.04	0.17	4.33

Table 2.9: Summary of total detection efficiencies for the gamma rays interested by summing-out.

The final efficiency curves shown in fig. 2.20 and 2.22 have been done including this correction.

2.2 Data analysis and results

During about five months of data taking, all the ^{22}Ne(p,γ)^{23}Na resonances at proton energy between 70 and 340 keV have been investigated. The measurement was performed filling the target chamber with enriched ^{22}Ne at 1.5 mbar pressure. The gas was isotopically enriched in ^{22}Ne at the 99.9% level.
Residual ^{nat}Ne from the gas taget characterization phase and nitrogen entering the setup through possible vacuum leaks may change the gas composition and be a source of beam induced background. Therefore, the ^{21}Ne and ^{14}N levels were checked on a daily basis exploiting the ^{21}Ne(p,γ)^{22}Na resonance at 271.6 keV and the ^{14}N(p,γ)^{15}O resonance at 278 keV. Throughout the experiment, the maximum natural neon contamination was at the 1% level, while the nitrogen content was always below 0.1%.

The investigation of the ^{22}Ne(p,γ)^{23}Na resonances was carried out with the following approach: in order to check the sensitivity to a particular resonance, a long run was performed at the beam energy where the maximum yield was expected (according to the literature resonance energy, the stopping power at 1.5 mbar and the position of maximum detection efficiency from the efficiency profiles). If a signal was observed, a complete resonance scan was performed in order to find the experimental energy of maximum yield. The resonance scans were obtained integrating the 440 keV peak, originating from the decay of the first excited state in ^{23}Na to the ground state. This was always the most intense line in the gamma ray spectrum since most of the higher energy states decay to the first excited state. Once the maximum of the excitation function was found, a long run was performed at the beam energy of maximum yield.
For the unobserved resonances, an upper limit for the resonance strength was calculated according to the experimental background in the region of interest of the 440 keV peak.
The resonances at 157 keV, 186 keV and 259 keV have been clearly detected and updated resonance energies of 156.2 keV, 189.5 keV and 259.7 keV have been derived from the corresponding excitation functions (see [44] for the detailed analysis). For the 71 keV, 105 keV and 215 keV resonances new upper limits on the resonance strength are provided. Finally, for the 291 keV, 320 keV and 334 keV resonances the 440 keV peak was observed in the spectrum but the yield is compatible with the direct capture cross section, therefore no estimate of the resonance strength is given.
In the following sections the resonance scans and the gamma ray spectra for the observed resonances are shown.
The most intense resonances observed are those at 189.5 keV and 259.7 keV, corresponding to the 8972 keV and 9041 keV excited states of ^{23}Na, respectively. For these resonances, several new gamma decay modes have been observed and the collected statistics is high enough to study gamma - gamma coincidences between the two detectors. The analysis of gamma - gamma coincidences is described in detail for the 189.5 keV resonance. The same general procedure has been applied to the 259.7 keV reosonance, but only the results are discussed. Finally, the new resonance strengths and upper limits are summarized.

2.2.1 156.2 keV resonance

The resonance scan for the 156.2 keV resonance is shown in fig. 2.24. In order to maximize the statistics, the yield is calculated summing the 440 keV peak areas in the two detectors.

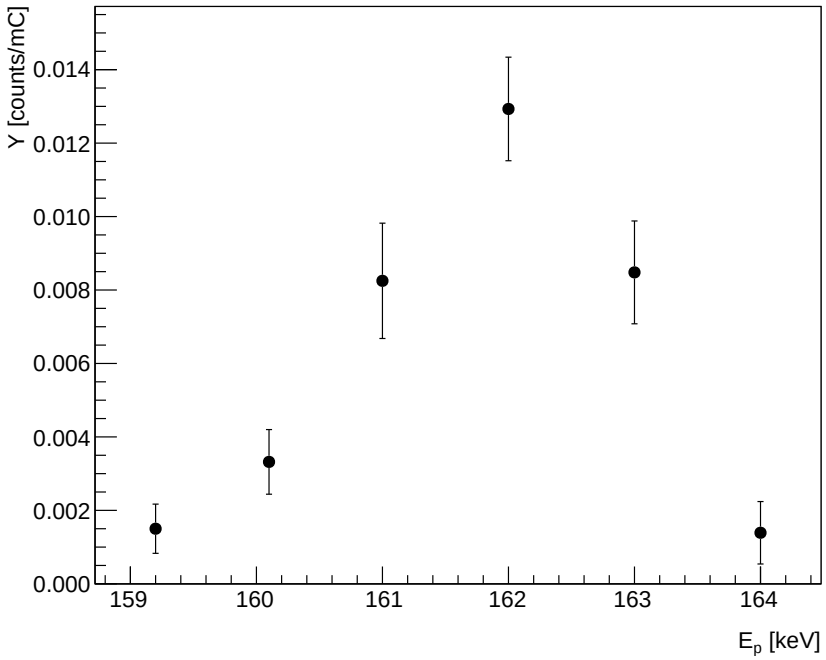

Figure 2.24: Excitation function of the 156 keV resonance. The sum of the 440 keV peak yields from the 55° and 90° detectors is reported.

Fig. 2.25 shows the comparison between a spectrum taken at the beam energy of maximum yield and an off resonance spectrum. The two spectra are normalized according to the integrated charge. The most intense transitions associated to the resonance decay or to beam induced background are labelled.

The 156.2 keV resonance corresponds to the 8944 keV excited state in ^{23}Na. This state was recently found to be part of a doublet with a 8945 keV level [23]. According to [23], the 8944 keV and 8945 keV levels have tentative spin and parity assignments of $3/2^+$ and $7/2^-$, respectively. The same authors report some gamma decay modes for the two levels (tab. 2.10).

As shown in fig.2.25, the observed transitions correspond to the decay of the $3/2^+$ state, while the decay modes reported for the $7/2^-$ state are not detected. Therefore, only the lower spin level of the doublet was observed in this experiment.

Branching ratios

The branching ratios for the observed decay modes of the 8944 keV level have been determined using the total statistics acquired at 162 keV beam energy (Q = 36.7 C) with the 55° detector, which is less affected by angular distribution effects. The branchings are calculated assuming that all possible decay modes are observed:

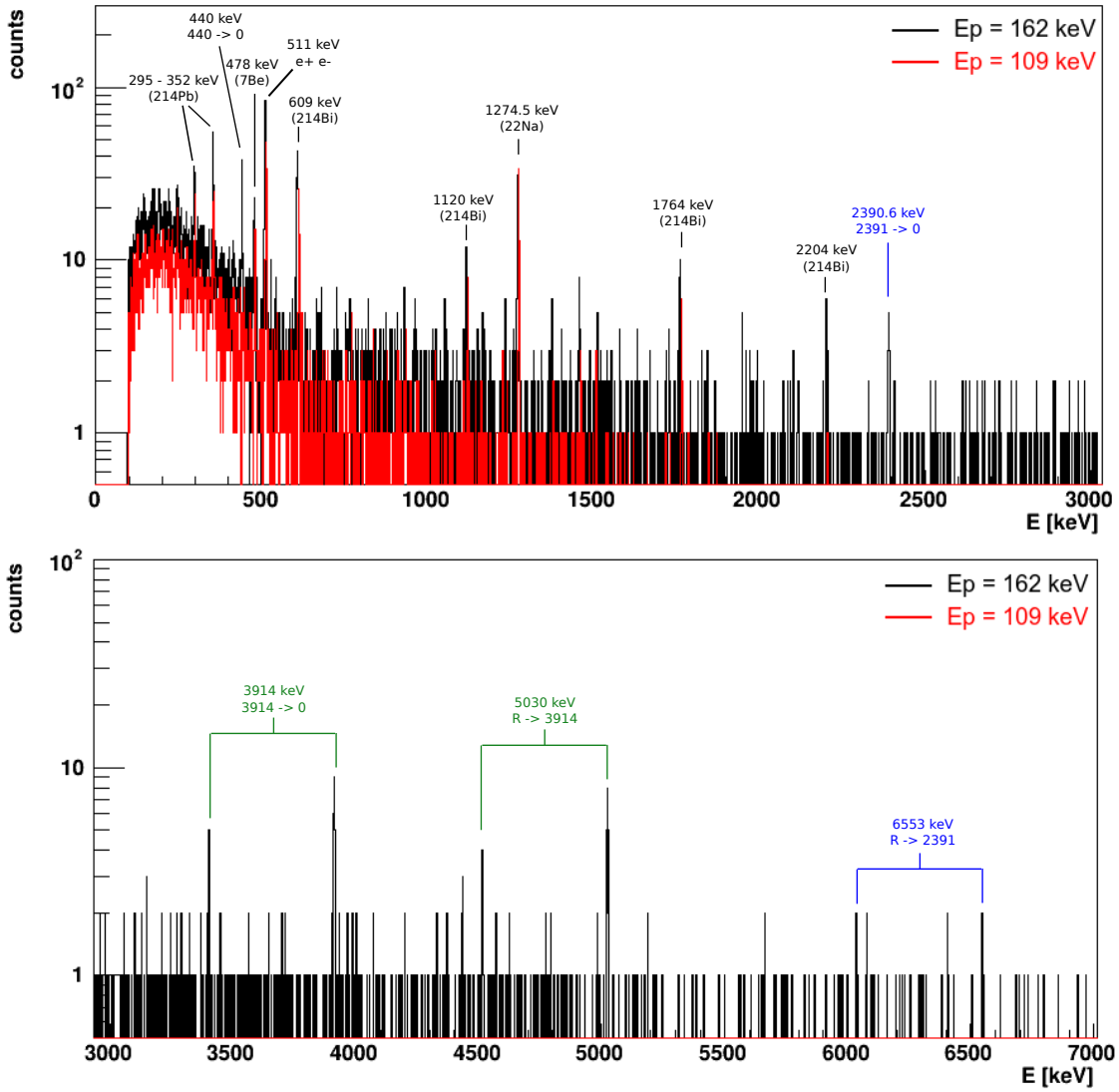

Figure 2.25: Comparison between on resonance (Q = 11.5 C) and off resonance (Q = 11.7 C) spectra for the 156 keV resonace. The resonance and background lines are also indicated.

E_i [keV]	E_f [keV]	E_γ [keV]
8944	3914	5030
8944	2391	6553
8945	7125	1821
8945	6353	2592
8945	2703.5	6240
8945	2076	6872

Table 2.10: Gamma decay modes reported in [23] for the doublet at 8944 keV. E_i is the initial state, E_f is the final state and E_γ is the energy of the emitted gamma. Since the energy difference between the two levels is not given in [23], the states are reported in table with their spin and parity in parenthesis.

$$Br_i = \frac{1}{\sum_j (A_j/\eta(E_j))} \cdot \frac{A_i}{\eta(E_i)} \tag{2.20}$$

where A_i is the net peak area for the transition i and η is the detection efficiency.
The results are reported in table 2.11.

E_i [keV]	E_f [keV]	E_γ [keV]	Branching [%]
8944	3914	5030	77 ± 4
8944	2391	6553	23 ± 4

Table 2.11: Gamma decay modes and branching ratios observed at LUNA for the 8944 keV excited state.

2.2.2 189.5 keV resonance

The excitation function of the 189.5 keV resonance is shown in fig. 2.26, while fig. 2.27 shows the comparison between the on and off resonance spectra. The on and off resonance spectra have been obtained with 16.5 C and 16.3 C of integrated charge, respectively.

The 189.5 keV resonance corresponds to the 8972 keV excited state in ^{23}Na. The only information on the gamma decay of the 8972 keV level is reported in [23]. In this work only a transition to the 2982 keV state was observed, while a number of transitions have been observed in the experiment performed at LUNA (fig. 2.27).
The analysis of gamma - gamma coincidences in the 55° and 90° detectors has been used to confirm the origin of the observed transitions. The analysis procedure is described in the following paragraph.

Gamma - gamma coincidences

The coincidence analysis has been performed exploiting the list mode acquisition system. The data used for this analysis have been collected running for five days at 194.5 proton beam energy (total integrated charge of 76.7 C).

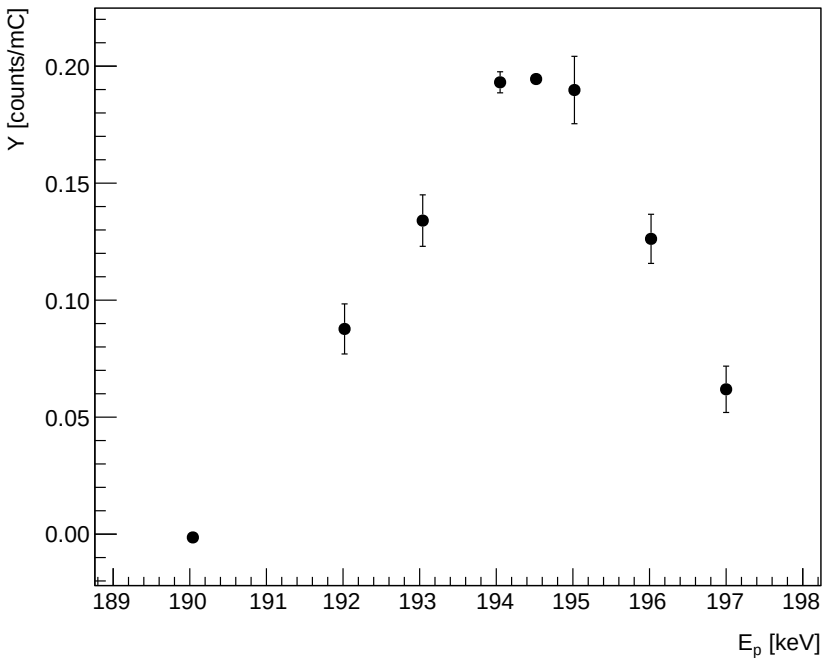

Figure 2.26: Excitation function of the 189.5 keV resonance obtained integrating the 440 keV peak.

In the first data sorting, coincident events have been identified comparing the time stamps of the events registered in the 55° and in the 90° detectors. In particular, two events were considered to be in coincidence if the difference between the time stamps was in the (-50 μs, 50 μs) range. Fig. 2.28 shows the distribution of the time differences between coincident events, which is actually confined in a narrower range between (-1 μs, 1 μs).

A coincidence matrix can then be obtained displaying the number of coincident events as a function of the the energy released in the 55° detector in the 90° detector. Fig. 2.29 shows the coincidence matrix for the 189.5 keV resonance. To increase the statistics, the matrix has beed binned at 20 keV per channel. The structures in the coincidence matrix correspond to the most intense gammas from the de-excitation of ^{23}Na.

The following general procedure has been adopted for the analysis of gamma - gamma coincidences: the coincident spectra have been obtained selecting, among all coincident events, those which fulfill a certain condition on the energy release in the 90° detector. The energy gates are applied on the low energy states of ^{23}Na that are directly populated in the resonance decay. The 90° detector has been chosen because it has higher detection efficiency for low energy gammas (while the 55° detector is more efficient at high energies).
The corresponding events in the 55° detector are then histogrammed and all the gamma ray lines produced in the resonance de-excitation are investigated. Fig. 2.30 shows a sample coincidence spectrum, obtained gating on the 440 keV transition in the 90° detector. In order to check the amount of background coincidences in the regions of the resonance peaks, a coincidence spectrum has

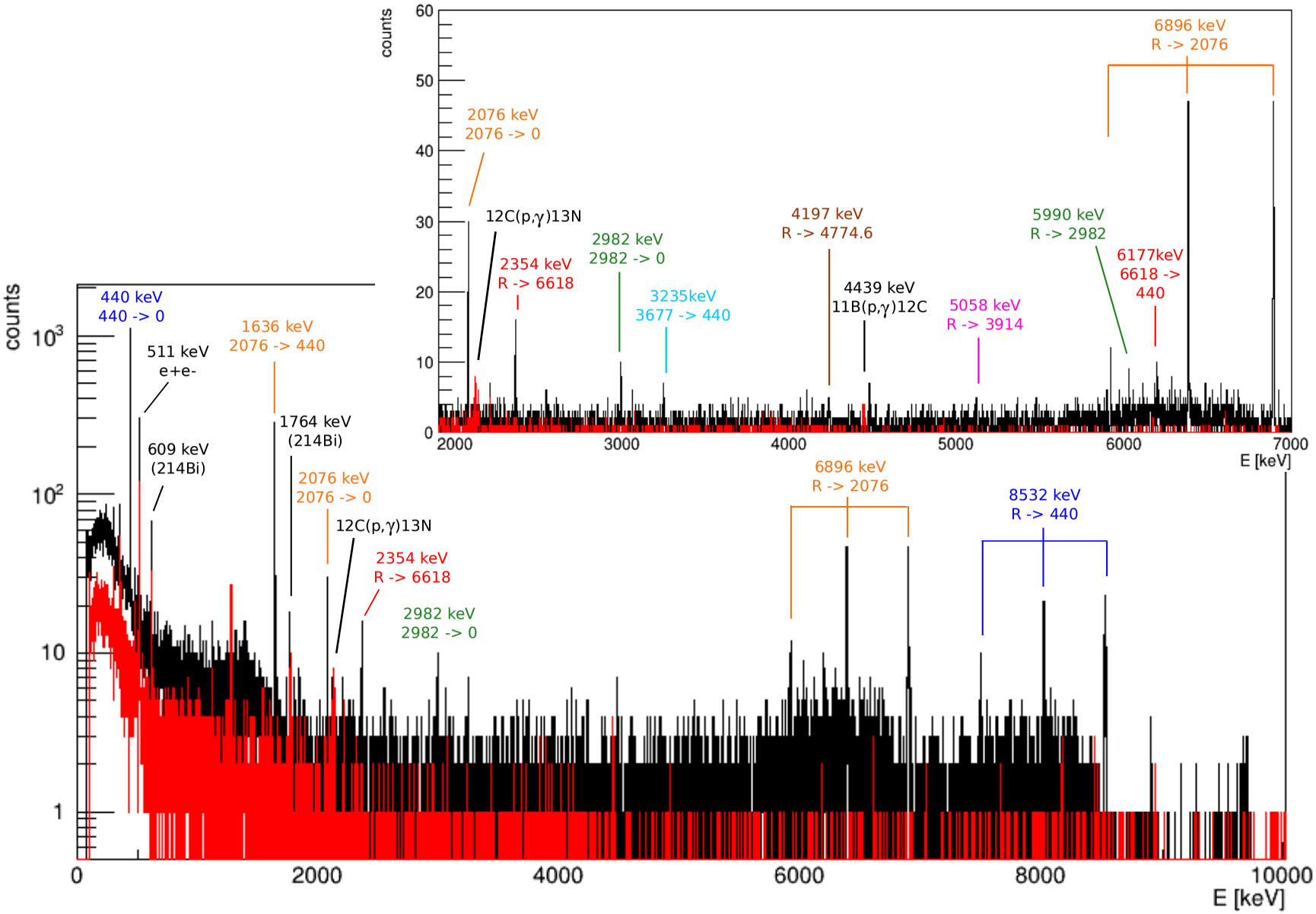

Figure 2.27: Comparison between on (black) and off (red) resonance spectra for the 189.5 keV resonance. The on and off resonance spectra are taken at 194.5 keV and 210 keV beam energy, respectively. The most intense lines associated to the de-excitation of ^{23}Na are labelled in blue, while background lines are labelled in black

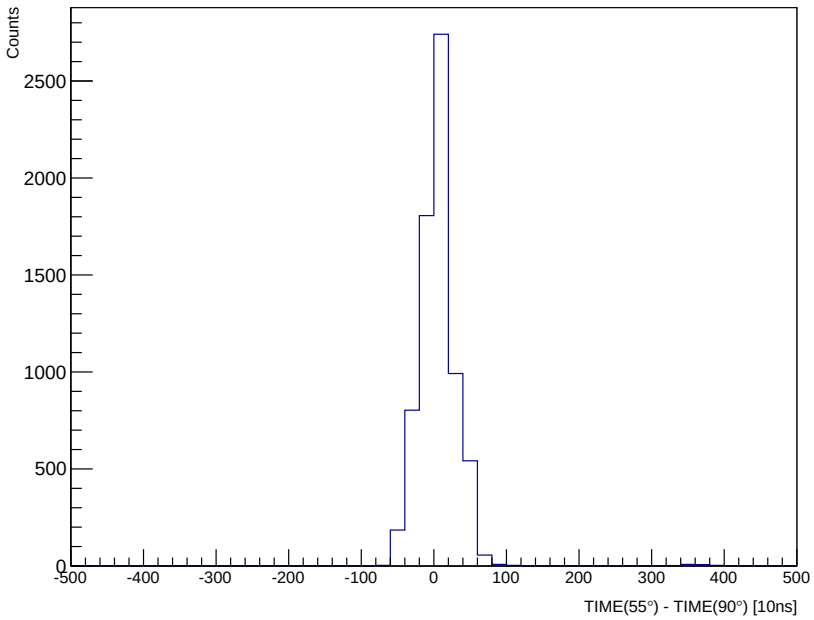

Figure 2.28: Distribution of the difference between the time stamps of coincidence signals recorded in the two detectors.

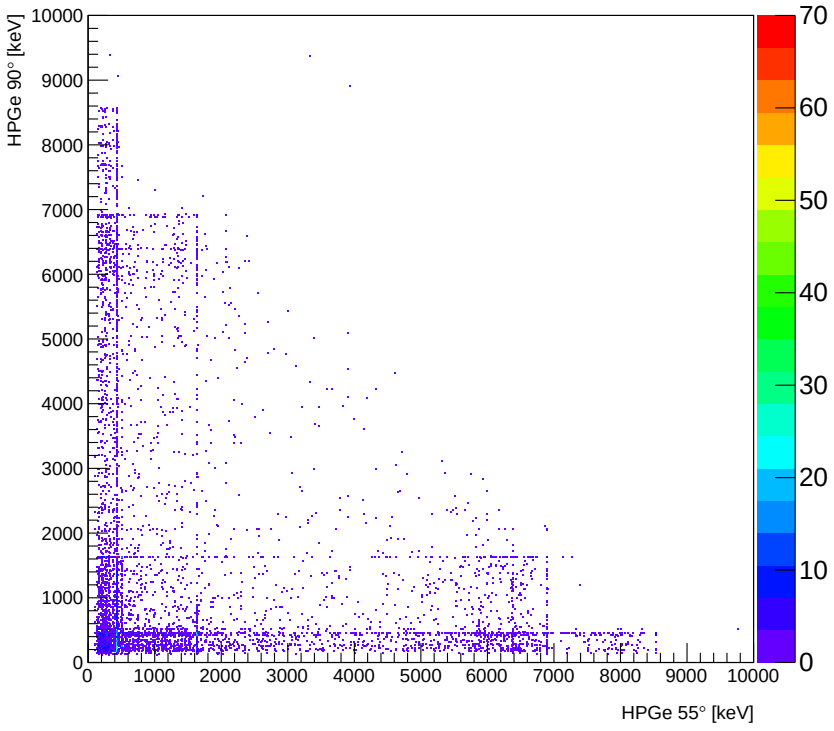

Figure 2.29: Coincidence matrix derived from the long run on top of the 189.5 keV resonance. The number of coincident events is expressed with the color code on the right.

been produced gating on a background region close to the 440 keV peak and of the same width.

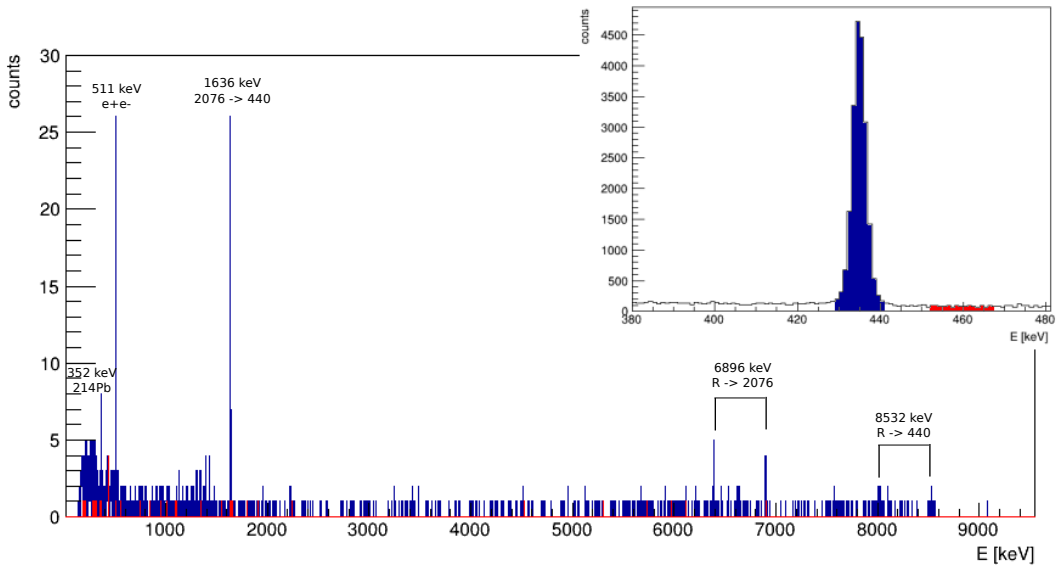

Figure 2.30: Coincidence spectrum obtained gating on the 440 keV transition in the 90° detector spectrum. In the insert, part of the 90° detector spectrum is shown with the peak gating region highlited in blue and the background gating region hilighted in red.

For the 189.5 keV resonance, gates on the transitions de-exciting the 440 keV, 2076 keV and 2982 keV levels (which are directly populated in the resonance decay) have been applied.
The transitions from the resonance to the 6618 keV and 4774.6 keV levels are expected to be in coincidence with the decay of the 440 keV and 2076 keV levels, since the 6618 keV and 4774.6 keV states decay with high probability to those states. Therefore, no additional gate has been included to investigate these transitions. The 3914 keV level decay mostly to the ground state. The resulting 3914 keV gamma is observed in the total spectra (not in fig. 2.27, which shows only part of the total statistics), but the statistics is too low to apply a coincidence gate.
For each coincidence spectrum, the net peak area for all the transitions de-exciting the 8972 keV level has been calculated. The regions of integration (ROI) used to calculate the net areas are determined on the full statistics spectrum of the 55° detector and then applied to the coincident spectrum. The statistical significance of the peak areas has been checked by comparison with the critical limit at 95% confidence level. The critical limit defines the number of counts below which the measured net area is compatible with the background fluctuations [45].
The net area A is defined as the difference between the total area N (obtained integrating the spectrum in the region of integration of the peak) and the background estimate B in the same ROI (calculated averaging the background at the right and left of the peak):

$$A = N - B \tag{2.21}$$

The uncertainty on the net area is calculated with the assumption that $\sigma(counts) = sqrt(counts)$:

$$\sigma_A^2 = N + \sigma_B^2 = A + B + \sigma_B^2 \tag{2.22}$$

The estimate of the background fluctuation in the ROI of the peak is obtained from equation 2.22 forcing the net area to be zero:

$$\sigma^2(A = 0) = B + \sigma_B^2 \tag{2.23}$$

The critical limit is calculated then calculated as:

$$L_c = k_\alpha \cdot \sigma^2(A = 0) \rightarrow L_c(95\% c.l.) = 1.645 \cdot \sigma^2(A = 0) \tag{2.24}$$

where the factor k_α depends on the confidence level adopted.

The results of the coincidence analysis are reported in table 2.12. For each energy gate, the area of the gamma transitions de-exciting the resonance in the coincidence spectrum is reported together with the critical limit (in parenthesis). Trying to maximize the statistics, the logical *or* of the energy gates on the 440 keV, 2076 keV and 2982 keV levels has also been performed. The results are displayed in the last line of table 2.12.

As shown in table 2.12, the transitions to the 440 keV and to the 2076 keV states (which were not observed in previous experiments) are observed in the coincidence spectrum with a number of counts higher than the critical limit. All other transitions have small branching ratios (see table 2.13), therefore the statistics is probably too low to observe a signature in the coincident spectrum. Since for those transitions both the gamma de-exciting the 8972 keV level and at least one of the gammas de-exciting the 2982 keV, 3914 keV, 4774.6 keV and the 6618 keV are detected, they have all been included in the resonance strength calculation.

Branching ratios

The branching ratios for the observed decay modes of the 8972 keV level have been determined with equation 2.20. The total statistics acquired with the 55° detector at 194.5 keV beam energy has been used. The results are reported in table 2.13.

While in [23] only the transition to the 2982 keV state was observed, the most intense transitions observed in this work are those to the 440 keV and 2076 keV levels.

2.2.3 259.7 keV resonance

The 259.7 keV resonance corresponds to the 9041 keV excited state in ^{23}Na. This level has recently been found to be part of a doublet with the 9038 keV level [23].

Gate	R→440 keV (8532 keV)	R→2076 keV (6896 keV)	R→2982 (5990 keV)	R→3677.6 (5294.4 keV)	R→3914 keV (5057.8 keV)	R→4774.6 keV (4197.4 keV)	R→6618 keV (2354 keV)
440 keV	8 ± 3 (1.9)	25 ± 5 (2.2)	1.5 ± 1.9 (2.4)	-0.9 ± 1.4 (2.8)	2.3 ± 2.2 (2.7)	-0.6 ± 1.4 (2.6)	0.5 ± 1.7 (2.5)
2076 keV	-	10 ± 3.2 (0)	-	0.7 ± 1.1 1.1	-	1 ± 1 (0)	-
2982 keV	-	-	-	-	-	-	-
All	8 ± 3 (1.9)	33 ± 6 (2.2)	1 ± 2 (2.8)	0 ± 1.7 (2.8)	2.3 ± 2.2 (2.7)	0.5 ± 1.7 (2.5)	0.5 ± 1.7 (2.5)

Table 2.12: Area of the gamma ray lines associated to the 189.5 keV resonance in the coincidence spectra obtained gating on different levels. The numbers in parenthesis represent the critical limit at 95% confidence level.

E_γ^{Th} [keV]	E_γ^{Exp} [keV]	E_f [keV]	Branching [%]
8532	8534.6	440	42 ± 1
6896	6897.3	2076	48 ± 1
5990	5991	2982	3.7 ± 0.5
5294.4	5297.5	3677.6	¡ 0.6
5057.8	5059.4	3914.2	1.3 ± 0.3
4197.4	4199.7	4774.6	1.7 ± 0.2
2354	2356.5	6618	2.8 ± 0.2

Table 2.13: Gamma decay modes and branching ratios observed at LUNA for the 8972 keV excited state (corresponding to the 189.5 keV resonance). The comparison between the gamma ray energy expected according to the literature level energies (E_γ^{Th}) and the observed gamma energies (E_γ^{Exp}) is also shown.

According to [23], the 9038 keV level has $J^\pi = 15/2^+$, while the 9041 keV level has $J^\pi = 7/2^+$ or $9/2^+$. The same authors report some gamma decay modes for the two levels (tab. 2.14).

E_i [keV]	E_f [keV]	E_γ [keV]
9038	7267	1771
9038	6234	2804
9038	5533	3505
9041	2076	6965
9041	440	8601

Table 2.14: Gamma decay modes reported in [23] for the 9038 and 9041 keV levels in ^{23}Na. E_i is the initial state, E_f is the final state and E_γ is the energy of the emitted gamma.

A complete resonance scan (fig. 2.31) and a long run at 264 keV proton beam energy (total integrated charge Q = 40.8 C) have been performed.

In fig. 2.32 the experimental spectrum taken on top of the 258 keV resonance is compared with a spectrum taken off resonance. The observed gamma transitions are also labelled. The figure shows that none of the transitions reported in 2.14 for the 9038 keV resonances is observed, while the two transitions associated to the 9041 keV are clearly visible in the spectrum.

This evidence is supported by selection rules arguments: the possibility to populate a resonance via a given reaction channel depends on angular momentum and parity conservation laws [2]. Angular momentum conservation requires the sum of the spins of the particles in the entrance channel j_1 and j_2, plus their relative angular momentum l, to add up to the angular momentum of the resonant state J:

$$J = j_1 + j_2 + l \tag{2.25}$$

Moreover, parity conservation requires the fulfillment of the relation

$$\pi(J) = (-1)^l \cdot \pi(j_1) \cdot \pi(j_2) \tag{2.26}$$

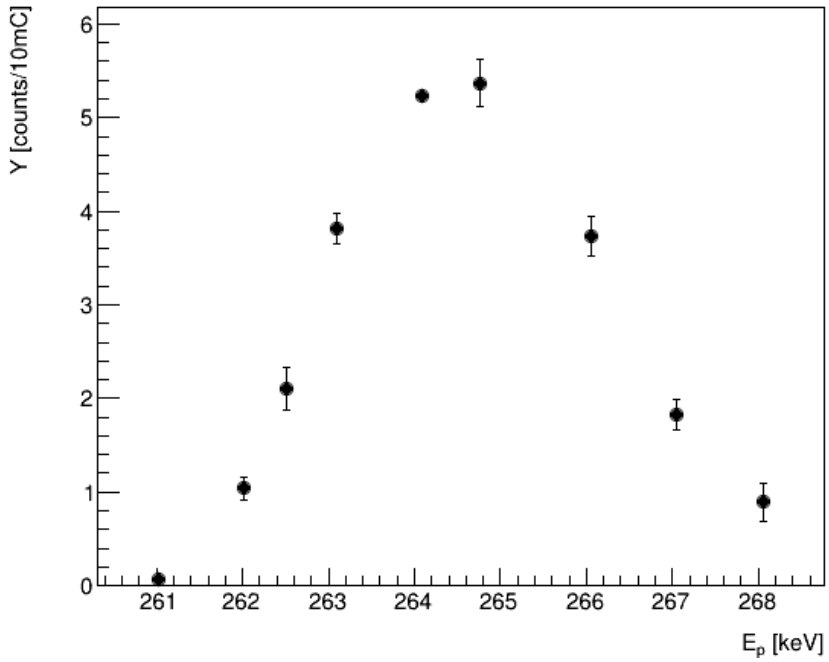

Figure 2.31: Scan of the 258 keV resonance measured with the 55° detector. The yield is calculated using the 440 keV transition.

where $\pi(j_1)$ and $\pi(j_2)$ are the parities of the reacting particles and $\pi(J)$ is the parity of the resonant state.
In the case of the ^{22}Ne(p,γ)^{23}Na resonance at 9038 keV, j_1^π is the spin and parity of the proton ($1/2^+$), j_2^π is the spin and parity of ^{22}Ne (0^+) and J^π is $15/2^+$ [23], therefore:

$$\frac{15}{2} = \frac{1}{2} + 0 + l \rightarrow l = 7$$

$$(-1)^7 \cdot + \cdot + \neq +$$

The spin and parity of the 9041 keV state is instead $7/2^+$ or $9/2^+$. Applying again equations 2.25 and 2.26 it is possible to verify that a $9/2^+$ state can be populated in the p + ^{22}Ne channel.

In addition to the transitions reported in [23], several other transitions are observed in the de-excitation of the 9041 keV level. In order to confirm the observed transitions, the analysis of gamma - gamma coincidences between the two detectors have been performed following the same procedure described for the 189.5 kev resonance.

Gamma - gamma coincidences

The coincidence matrix obtained for the 259.7 keV resonance is shown in fig. 2.33. Also in thise case some structures are observed, corresponding to the most intense gammas emitted in the ^{23}Na de-excitation.

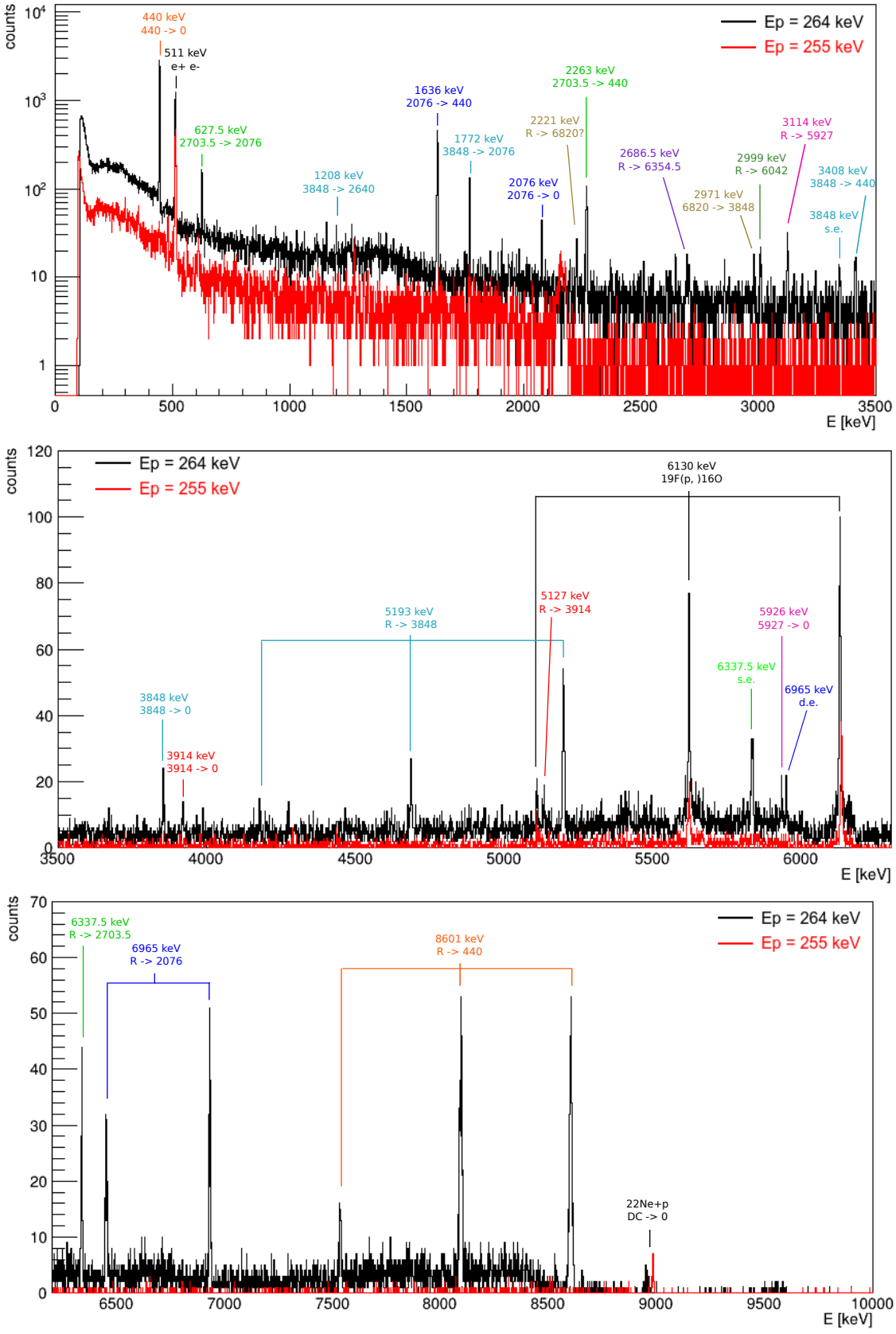

Figure 2.32: Comparison between on and off resonance spectra for the 259.7 keV resonace. The lines observed in the on resonance spectrum are also identified.

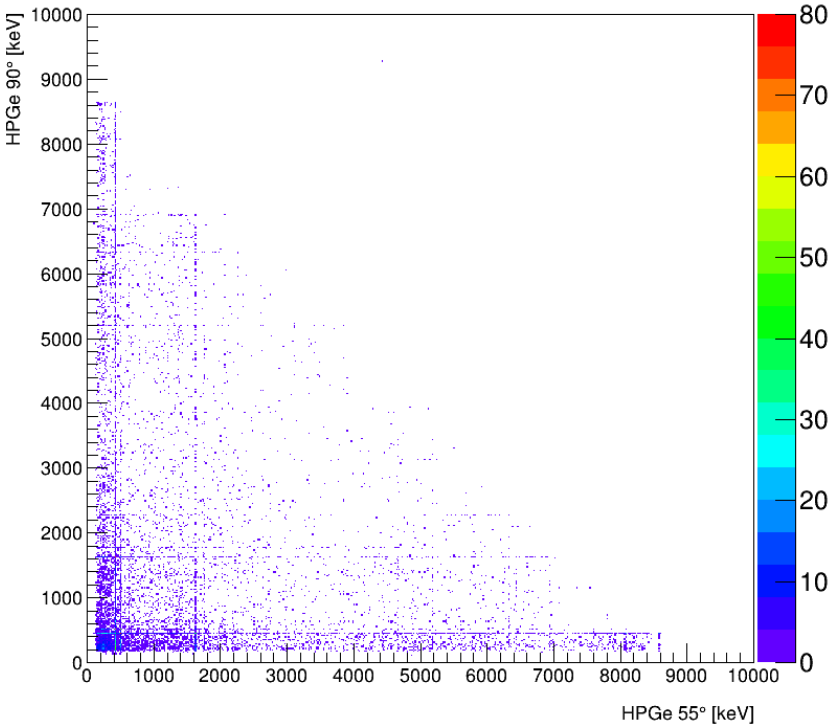

Figure 2.33: Coincidence matrix built using a long run on top of the 259.7 keV resonance. The number of coincident counts is expressed with the color scale.

Gates on the most intense transitions from the decay of 440, 2076, 2703.5, 3848 and 3914 keV levels have been applied on the 90° detector. These low energy levels are directly populated in the resonance decay. Moreover, they collect most of the statistics from the decay of high energy levels.
Fig. 2.34 shows a sample coincidence spectrum obtained gating on the 440 keV peak, together with the spectrum obtained gating on the background.

The results of the analysis of gamma-gamma coincidences are reported in table 2.15 in the same way as table 2.12.

The transitions to the 440 keV, 2076 keV, 2703.5 keV and 6042 keV levels are observed in the coincidence spectra with a number of counts higher than the critical limit, therefore they are confermed by the coincidence analysis.

Branching ratios

The branching ratios for the decay of the 9041 keV state (reported in tab. 2.16) have been derived from the long run at 264 keV beam energy (Q = 44.3 C).

In [23] only the transitions to the 440 keV and 2076 keV levels are mentioned. Those are among the most intense transitions observed at LUNA, but many other transitions have been observed as well.

Gate	R→440 keV (8602 keV)	R→2076 keV (6963 keV)	R→2703.5 keV (6335 keV)	R→3848 keV (5193 keV)	R→3914 keV (5127 keV)	R→5927 keV (3115 keV)	R→6042 keV (3000 keV)	R→6354.5 keV (2686.5)	R→6820 keV (2221 keV)
440 keV	25 ± 5 (0)	7.4 ± 3.6 (3.8)	7.4 ± 3.3 (3.2)	8.0 ± 3.3 (2.7)	-0.2 ± 1.3 (2.2)	0.8 ± 1.6 (2.3)	3.4 ± 2.1 (1.7)	-	1 ± 1 (0)
2076 keV	-	5 ± 2.2 (0)	0.5 ± 1.1 (1.4)	0.5 ± 1.1 (1.4)	0.8 ± 1.0 (0.8)	-	0.6 ± 1.1 (1.2)	1 ± 1 (0)	-
2703.5 keV	-	-	5 ± 2.2 (0)	2 ± 1.4 (0)	-	-	1 ± 1 (0)	-	-
3848 keV	-	-	-	3 ± 1.7 (0)	-	-	-	-	-
3914 keV	-	-	-	-	-	-	-	-	-
All	25 ± 5 (0)	11.4 ± 4.1 (3.8)	9.9 ± 3.8 (3.5)	10.6 ± 3.7 (3.0)	0.6 ± 1.7 (2.4)	0.6 ± 1.6 (2.3)	4.4 ± 2.3 (1.7)	0.3 ± 1.2 (1.7)	1 ± 1 (0)

Table 2.15: Area of the gamma ray lines associated to the 259.7 keV resonance in the coincidence spectra obtained with gates on different levels. The numbers in parenthesis represent the critical limit at 95% confidence level.

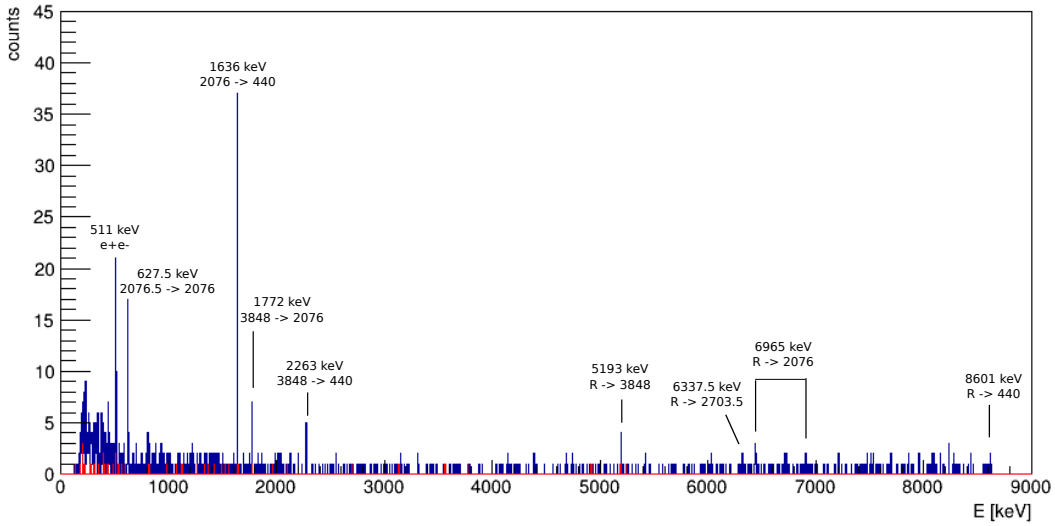

Figure 2.34: Coincidence spectrum obtained gating on the 440 keV transition in the 90° detector spectrum. In the insert, part of the 90° detector spectrum is shown with the peak gating region highlighted in blue and the background gating region highlighted in red.

2.2.4 Resonance strength determination

As discussed in section 1.1, the resonance strength $\omega\gamma$ allows to calculate the thermonuclear reaction rate for a Breit-Wigner resonance (eq. 1.12 and 1.13). The measured quantity in a nuclear physics experiment is the reaction yield Y:

$$Y \equiv \frac{number\,of\,reactions}{number\,of\,incident\,particles} = \frac{A}{\eta \cdot (I \cdot t/1.602 \cdot 10^{-19})} \tag{2.27}$$

where A is the peak area in the gamma ray spectrum, η is the detection efficiency, I is the beam current in ampere, t is the data acquisition time and $1.602 \cdot 10^{-19}$ is the elementary charge.
The experimental yield at a given beam energy E_0 is related to the nuclear reaction cross section by the relation

$$Y(E_0) = \int_{E_0-\Delta E}^{E_0} \frac{\sigma(E)}{\epsilon(E)} dE \tag{2.28}$$

where ΔE is the total energy lost by the beam in the target and ϵ(E) is the effective stopping power.
Integrating eq. 2.28 for a Breit-Wigner cross section and assuming the stopping power, the Broglie wavelength, and the partial widths of the resonance are independent of the energy over the resonance width, the yield becomes:

$$Y(E_0) = \frac{\lambda^2}{2\pi} \frac{m_p + m_t}{m_t} \frac{\omega\gamma}{\epsilon} \left[arctan\left(\frac{E_0 - E_R}{\Gamma/2}\right) - arctan\left(\frac{E_0 - E_R - \Delta E}{\Gamma/2}\right)\right] \tag{2.29}$$

E_γ^{Th} [keV]	E_γ^{Exp} [keV]	E_f [keV]	Br [%]
8601	8601.7	440	45.4 ± 0.9
6965	6966.8	2076	18.7 ± 0.6
6337.5	6339.4	2703.5	10.9 ± 0.5
5193	5195	3848	13.3 ± 0.5
5127	5128.7	3914	1.8 ± 0.4
3114	3116	5927	3.6 ± 0.2
2999	3001	6042	2.6 ± 0.2
2686.5	2688.6	6354.5	1.5 ± 0.0
2221.4	2222.5	6819.6	2.2 ± 0.2

Table 2.16: Gamma decay modes and branching ratios for the 9041 keV excited state (corresponding to the 259.7 keV resonance) observed at LUNA. The comparison between expected and observed gamma ray energies is also shown.

with m_p projectile mass and m_t target mass.
If the target thickness is much larger compared to the total resonance width ($\Delta E >> \Gamma$), the maximum yield is:

$$Y_{max}(E \to \infty) = \frac{\lambda^2}{2} \frac{m_p + m_t}{m_t} \frac{\omega\gamma}{\epsilon} \tag{2.30}$$

where

$$\frac{\lambda^2}{2} = \left(\frac{m_p + m_t}{m_t}\right)^2 \frac{4.125 \cdot 10^{-18}}{m_p E_R^{LAB}} \tag{2.31}$$

with the masses in amu and the resonance energy in the laboratory system E_R^{LAB} in eV.
The strengths of the observed ^{22}Ne(p,γ)^{23}Na resonances have been calculated with equations 2.30 and 2.31, where the yield at the maximum of the excitation function curve has been calculated assuming that all possible decay modes are observed:

$$Y = \frac{\sum_j (A_j/\eta(E_j))}{(I \cdot t/1.602 \cdot 10^{-19})} \tag{2.32}$$

Since for all resonances the strength obtained for the 55° and for the 90% detectors is compatible within the error bars, the final value has been obtained combining the two results to improve the statistical uncertainty.
For the unobserved resonances, new upper limits on the resonance strengths have been calculated according to the background in the region of integration of the 440 keV peak. The 55° detector has been used, in order to minimize possible angular distribution effects.
From the statistical point of view, the upper limit at 90% confidence level is calculated as:

$$L_U = A + 1.282 \cdot \sigma_A \tag{2.33}$$

where A is the net peak area and σ_A is the error associated to the net area. Since the 440 keV transition collects most of the statistics from the decay of the higher energy states, the upper limits have been evaluated assuming 100% branching ratio for the 440 keV line.
The results are summarized in table 2.17.

$E_{res,LAB}$ [keV]	$\omega\gamma$ [eV]			
	J. Görres [17]	NACRE [4]	Iliadis et al. [15]	LUNA
71	$\leq 3.2 \cdot 10^{-6}$	$\leq 4.2 \cdot 10^{-9}$	-	$\leq 3.4 \cdot 10^{-9}$
105	$\leq 6.0 \cdot 10^{-7}$	$\leq 6.0 \cdot 10^{-7}$	-	$\leq 7.0 \cdot 10^{-9}$
156.2	$\leq 1.0 \cdot 10^{-6}$	$(6.5 \pm 1.9) \cdot 10^{-7}$	$(9.2 \pm 3.7) \cdot 10^{-9}$	$(1.48 \pm 0.09_{stat} \pm 0.04_{syst}) \cdot 10^{-7}$
189.5	$\leq 2.6 \cdot 10^{-6}$	$\leq 2.6 \cdot 10^{-6}$	$\leq 2.6 \cdot 10^{-6}$	$(1.87 \pm 0.03_{stat} \pm 0.04_{syst}) \cdot 10^{-6}$
215	$\leq 1.4 \cdot 10^{-6}$	$\leq 1.4 \cdot 10^{-6}$	-	$\leq 2.4 \cdot 10^{-8}$
259.7	$\leq 2.6 \cdot 10^{-6}$	$\leq 2.6 \cdot 10^{-6}$	$\leq 1.3 \cdot 10^{-6}$	$(6.89 \pm 0.08_{stat} \pm 0.14_{syst}) \cdot 10^{-6}$

Table 2.17: Summary of resonance strengths and upper limits for the resonances investigated at LUNA. The results are compared with the literature data.

For the 71, 105 and 215 keV resonances, new upper limits have been calculated which are lower than the literature values.
For the 156.2 keV resonance, the NACRE strength is adopted from [16], while the Iliadis et al. strength is taken from [20]. Both resonance strengths were derived from indirect data assuming a spin and parity of $7/2^-$ for the corresponding excited state. This excited state was recently found to be a doublet [23], composed of a $3/2^+$ and a $7/2^-$ levels and only the level with $J^\pi = 3/2^+$ was observed in the LUNA measurement. Therefore, the spin and parity assumptions that have been made in the indirect measurement to derive the resonance strength from the spectroscopic factor may be the reason for the discrepancy.
For the 189.5 keV resonance, the new resonance strength is compatible with the literature upper limits.
Finally, for the 259.7 keV resonance, the new $\omega\gamma$ is higher than the literature upper limits. The NACRE upper limit is adopted from a direct measurement [17] and the reason for the discrepancy may lie in the assumptions that have been made in [17] on the decay branching ratios, which were not known at that time. Indeed, the branching ratios for the decay of the 259.7 keV resonance have been derived at LUNA for the first time. The Iliadis upper limit is adopted from the indirect measurement of Hale et al. [20]. Since this resonance was also found to be part of a doublet composed of a high and a low spin state, confusion between the two levels may be the reason for the discrepancy [23].

Chapter 3

Study of ^{22}Ne(p,γ)^{23}Na high energy resonances at HZDR

With the advent of high resolution spectrometers it has become possible to measure the abundances of the elements in some astrophysical objects with high accuracy. Theoretical models of classical nova end type Ia supernova try to reproduce both the detailed mechanism and the nucleosynthetic output of the explosion. These models require a precise knowledge of the cross sections of all nuclear reactions involved.
The ^{22}Ne(p,γ)^{23}Na resonances between 436 keV and 661 keV have already been measured in the past, but for some of them the uncertainty on the resonance strength is still high.
In order to pin down those strengths, a new direct measurement has been performed at Helmholtz-Zentrum Dresden-Rossendorf (HZDR). The experimental setup, data analysis and results are reported in the following sections.

3.1 Experimental Setup

A proton beam was provided by the 3 MV Tandetron of HZDR [46]. The accelerator consist of a Cs sputter ion source, producing negatively charged atoms. A 90° injection magnet selects the required charge/mass, then the ions are sent to the accelerator tube. A nitrogen gas stripper changes the ion charge to positive, so that ions can be further accelerated in the second half of the acceleration tube. A switching magnet sends the beam to the proper beam line, where it is focused and delivered to the target.
A photo and a scheme of the experimental setup are shown in fig. 3.1.

Before reaching the target, the beam goes through a water cooled copper collimator of 5 mm diameter and a copper tube of 30 mm diameter extending up to 2 mm from the target. During irradiation, this tube was biased to -100 V in order to force secondary electrons back to the target and to allow a precise measurement of the beam current. The beam current was measured with a current integrator and it was both displayed by an analog scaler and recorded by the list mode data acquisition system. The proton beam intensity on target was always between 5 and 10 μA.

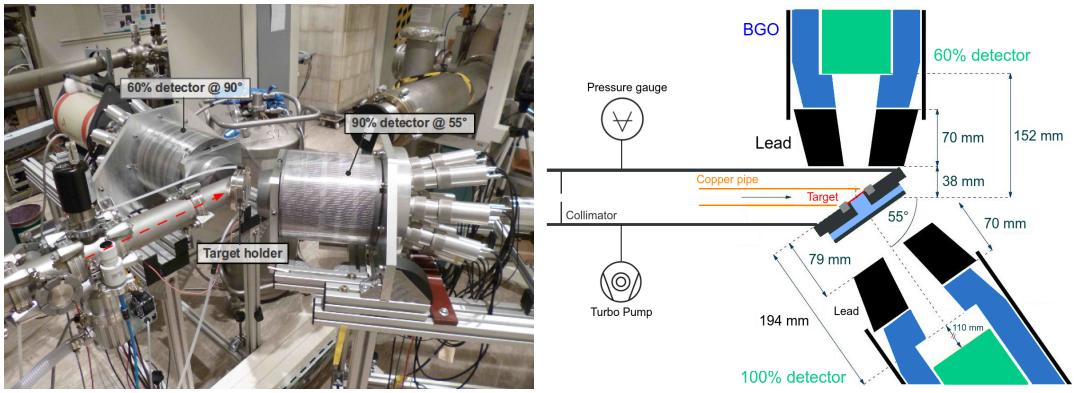

Figure 3.1: Photo and scheme of the experimental setup used for the measurement of ^{22}Ne+p high energy resonances at HZDR. The scheme is adapted from [47].

The target holder was electrically insulated from the rest of the chamber and the target was directly water cooled to prevent deterioration.
A turbomolecular pump kept the target chamber pressure in the 10^{-7} mbar range.

3.1.1 ^{22}Ne solid target preparation

Solid ^{22}Ne targets were produced with the implantation technique at the 200 kV high-current implanter of Legnaro National Laboratories (Italy).
The backing material of implanted targets should contain as high a density of implanted atoms as possible and be stable against outgassing. Moreover, high Z backings are typically used in order to minimize the beam induced background from the interaction of the beam inside the backing itself.
Concerning the implantation of neon gas, previous investigations showed that tantalum backings provide high saturation concentrations (between 10^{17} and 10^{18} atoms/cm^2) and a good stability of the implantation against beam irradiation [48–51]. Therefore, tantalum disks of 27 mm diameter and 0.2 mm thickness were used as backings.
Neon gas with natural isotopic composition (90.48% ^{20}Ne, 0.27% ^{21}Ne, 9.25% ^{22}Ne) was ionized, accelerated and sent to an analysing magnet to select only the mass-22 isotope. Then the ^{22}Ne beam was sent to a quadrupole magnet providing beam focusing and to the target chamber. A beam scanning magnet located between the quadrupole and the target produced a uniform beam spot of (10 x 8) cm on target. This allowed to produce, in a single irradiation, more than one implanted target with uniform implantation along the backing surface.
SRIM simulations [32,52] have been used to determine the irradiation energies and doses. The irradiation energy determines the depth of the implanted layer, while the dose defines the ion concentration. The thickness of the implanted region should allow to separate the ^{22}Ne + p resonances. Moreover, to simplify the data analysis, the total beam energy loss should be much higher than the resonance width and beam energy spread, lying in the infinitely thick target approximation.
Considering this requirements, the following ^{22}Ne doses have been chosen for the tantalum backing irradiation:

- $1.5 \cdot 10^{17}$ atoms/cm^2 at $E_{^{22}Ne} = 150$ keV
- $0.5 \cdot 10^{17}$ atoms/cm^2 at $E_{^{22}Ne} = 70$ keV

Throughout the irradiation, the ^{22}Ne beam current on target was about 2 μA/cm^2. The implantation profile predicted by means of SRIM simulations is shown in fig. 3.2. The predicted shape of the implantation profile is obtained as the sum of the profiles obtained at 150 keV and 70 keV, assuming that the number of incident ions at 150 keV is three times higher than the dose at 70 keV.

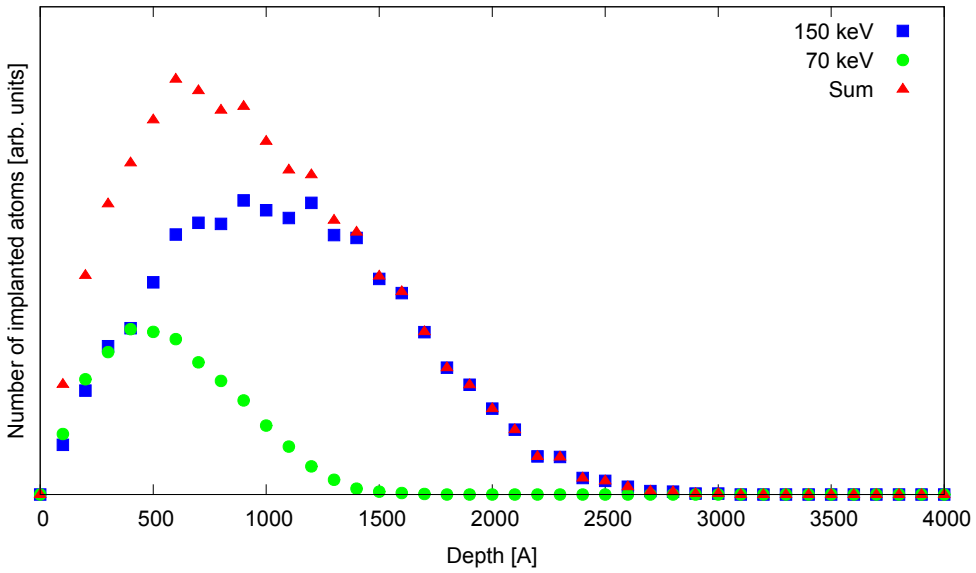

Figure 3.2: Shape of the implantation profile predicted with SRIM simulations. The profiles obtained for ^{22}Ne beams at 150 keV and 70 keV incident on a tantalum backing are displayed, as well as their sum. The number of ions at 150 keV is assumed to be three times higher than the number of ions at 70 keV.

The true implantation profile and target stoichiometry were measured during the experiment using the well known ^{22}Ne + p resonances at 1279 keV and 479 keV. The results are discussed in section 3.2.1.

3.1.2 Detectors and data acquisition

The gamma rays emitted in the ^{23}Na decay were detected by two high-purity germanium detectors of 90% and 60% relative efficiency positioned at 55° and 90° with respect to the beam direction, respectively. The two detectors were surrounded by BGO scintillators used as anti-Compton shields. Each BGO detector was enclosed in a 2 cm thick lead cylinder suppressing the environmental background. Moreover, the BGO detectors were shielded from radiation directly coming from the target by 7 cm thick lead collimators (fig. 3.1).
The BGO crystals detect with high efficiency the secondary gamma rays which scatter out of the germanium detector. When an event in the BGO is in coincidence with an event in the HPGe detector, the gamma ray detection in the HPGe is rejected. This improves the peak-to-total ratio and reduces the overall

background in the spectra. Fig. 3.3 shows ^{137}Cs spectra with and without Compton suppression. During the acquisition, the source was mounted at the target position.

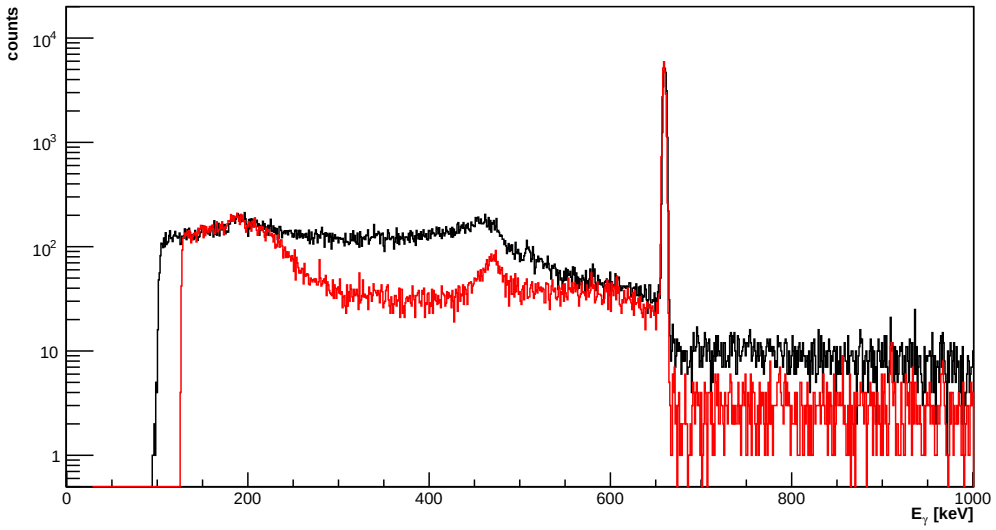

Figure 3.3: ^{137}Cs spectra with (red) and without (black) Compton suppression. The spectra were acquired with the 60% detector.

Table 3.1 shows, as an example, the peak-to-total improvement calculated for the 662 keV peak of ^{137}Cs.

	^{137}Cs Peak area	^{137}Cs Total area	P/T [%]
60% no anti-Compton	23871	82823	29
60% with anti-Compton	23620	54925	43
90% no anti-Compton	11369	28932	39
90% with anti-Compton	11230	22992	49

Table 3.1: Effect of the anti-Compton shielding on the peak-to-total ratio for both detectors.

As for the experiment performed at LUNA, two data acquisition systems have been used: one with a 100 MHz, 14-bit CAEN N1728B ADC (providing list mode data) and the other with an Ortec 919E ADC unit. A scheme of the data acquisition system is provided in fig. 3.4.

Detection efficiency

The full-energy peak efficiency was measured for gamma ray energies up to 10.8 MeV using ^{137}Cs, ^{60}Co and ^{88}Y sources and the ^{27}Al(p,γ)^{28}Si reaction.
The same radioactive sources used for the LUNA measurement have been used. The list of the most intense gamma rays emitted by each radioactive source is given in table 2.3, while the reference activities and dates are given in table 2.4.

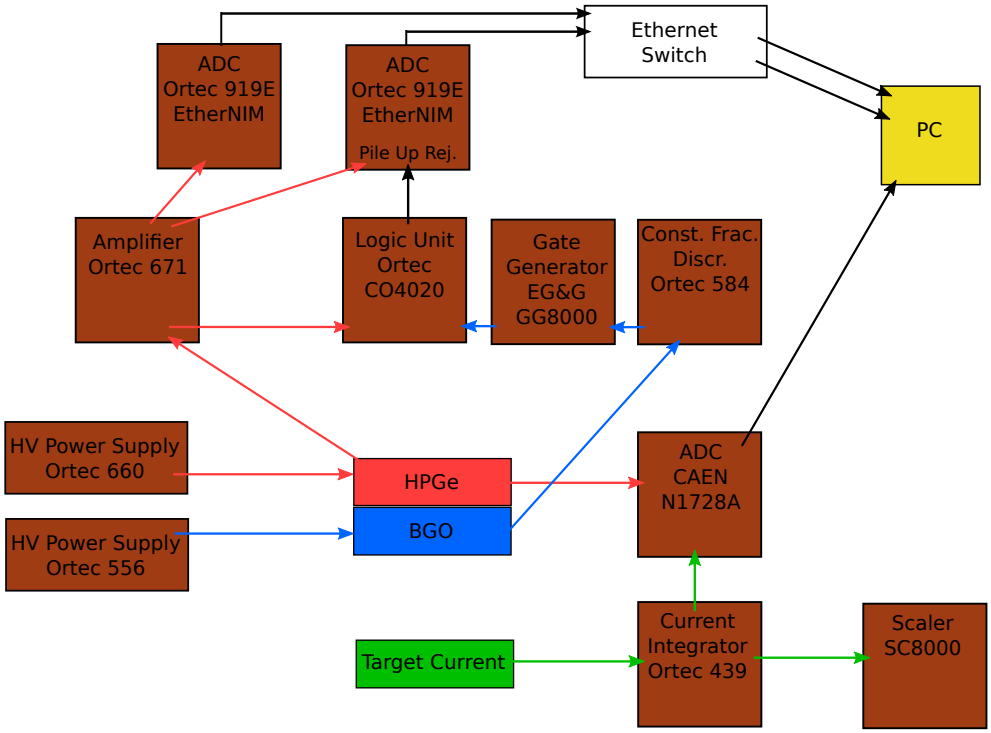

Figure 3.4: Scheme of the data acquisition system for one HPGe detector with BGO anti-Compton shield. The same acquisition scheme was adopted for both detectors.

The absolute detection efficiency measurement with radioactive sources was performed keeping the experimental setup unchanged and with the source mounted at the target position. The detection efficency obtained with the sources is shown in fig. 3.5. The same data analysis procedure described in section 2.1.5 has been followed, and the data have been fitted with a second order polynomial in the double logarithmic plane (eq. 2.15).

The fitting parameters and reduced χ^2 are reported in table 3.2.

Detector	a	b	c	χ^2/d.o.f.
HPGe 55°	-19.7 ± 0.1	5.38 ± 0.02	-0.414 ± 0.002	1.2
HPGe 90°	-0.61 ± 0.06	0.36 ± 0.01	-0.075 ± 0.001	0.95

Table 3.2: Fitting parameters for the efficiency curve measured with radioactive sources.

The efficiency curve was then extended to high gamma ray energies exploiting the ^{27}Al(p,γ)^{28}Si resonance at 992 keV proton energy (E_x = 12541.5 keV). This strong resonance ($\omega\gamma = (1.91 \pm 0.11)$ eV) [4], corresponds to the ^{28}Si excited state at 12541.5 keV which decays through a gamma ray cascade including an intense gamma of 1778.9 keV energy (lying in the energy range covered by radioactive sources) and a number of high energy gammas up to 10762.9 keV. This allows to derive the efficiency at high energies with a relative method, which is independent of the target composition and resonance strength. The use of the ^{27}Al(p,γ)^{28}Si resonance at 992 keV as a standard for efficiency measurements is documented

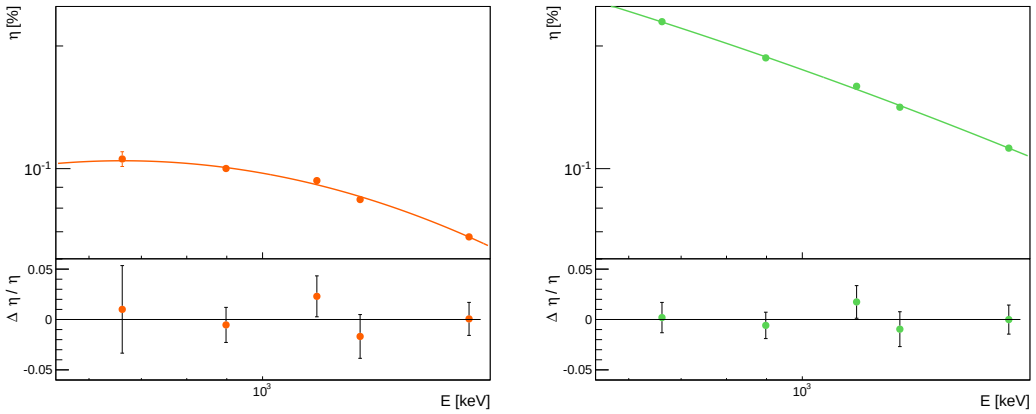

Figure 3.5: Detection efficiency measured with radioactive sources for the 55° detector (left) and for the 90° detector (right). The fitting function and residuals are also shown.

E_γ [keV]	E_i [keV]	E_f [keV]	Branching [%]	a_2	a_4
1778.9	1778.9	0	94.8 ± 1.5	0.000 ± 0.003	-0.016 ± 0.003
2838.9	4617.8	1778.9	5.5 ± 0.4	-0.009 ± 0.011	-0.022 ± 0.013
3063.3	r	9478.5	1.15 ± 0.11	0.08 ± 0.03	0.02 ± 0.03
3123.7	r	9418.1	0.70 ± 0.07	0.03 ± 0.03	-0.16 ± 0.04
4497.6	6276.5	1778.9	4.8 ± 0.3	0.085 ± 0.012	-0.069 ± 0.013
4608.4	r	7933.4	4.5 ± 0.4	-0.013 ± 0.014	0.036 ± 0.015
4743.0	r	7798.8	8.8 ± 0.5	-0.015 ± 0.009	-0.003 ± 0.011
6019.9	7798.8	1778.9	6.0 ± 0.5	0.003 ± 0.012	0.029 ± 0.014
6265.3	r	6276.5	2.1 ± 0.2	0.08 ± 0.02	-0.09 ± 0.02
10762.9	r	1778.9	76.6 ± 1.5	0.051 ± 0.005	-0.032 ± 0.005

Table 3.3: Most intense gamma transitions de-exciting the ^{27}Al(p,γ)^{28}Si resonance at 992 keV (E_x = 12541.5 keV) and corresponding branching ratios and angular distribution coefficients [53].

in [53, 54].
A typical spectrum of the ^{27}Al(p,γ)^{28}Si resonance at 992 keV is shown in fig. 3.6. The most intense transitions are also indicated. Only gamma rays with known angular distribution have been used for the efficiency measurement. These transitions are highlighted in blue in fig. 3.6.

The transitions used for the efficency measurement, their absolute branching ratios and the angular distribution coefficients are listed in table 3.3.

The efficiency at energy E_x was obtained with the following relation:

$$\eta(E_x) = \eta^{fit}(1779keV) \cdot \left(\frac{N_x}{Br_x \cdot W_x(\theta)}\right) \cdot \left(\frac{N_{1779}}{Br_{1779} \cdot W_{1779}(\theta)}\right)^{-1} \tag{3.1}$$

where $\eta^{fit}(1779keV)$ is the efficiency at 1779 keV calculated from the fit of radioactive sources data, N is the number of counts in the gamma ray spectrum, Br is the branching ratio and W(θ) is the angurar distribution function. The

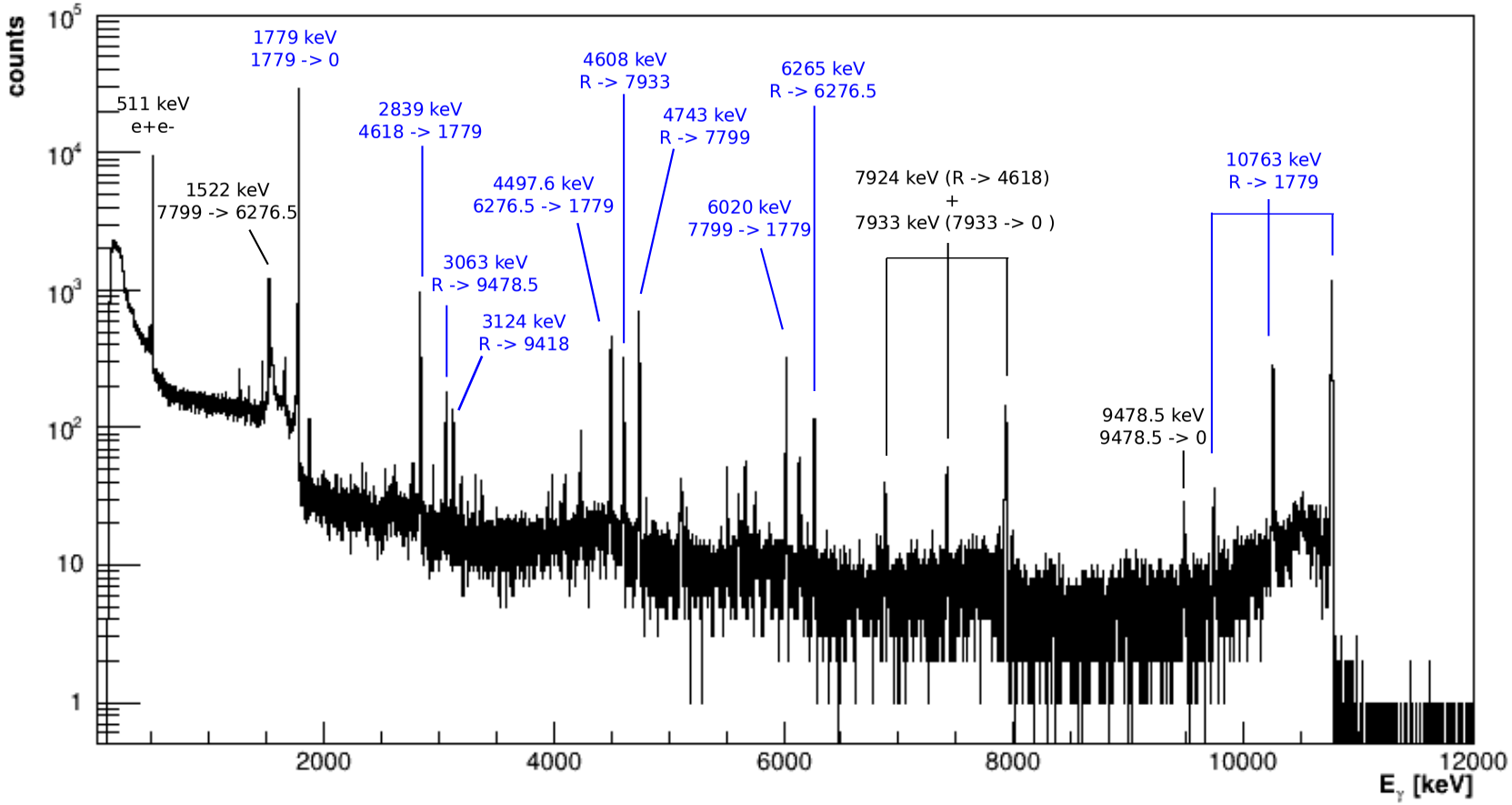

Figure 3.6: Gamma ray spectrum of the ^{27}Al+p resonance at 992 keV. The lines labelled in blue are those used for the efficiency measurement.

Detector	a	b	c	χ^2
HPGe 55°	-8.6 ± 1.3	2.3 ± 0.3	-0.19 ± 0.02	1.1
HPGe 90°	-5.3 ± 0.6	1.7 ± 0.2	-0.17 ± 0.01	1.5

Table 3.4: Fitting parameters for the complete efficiency curves.

value of W(θ) at 55° and 90° is calculated with equation 2.17, where Q_2 and Q_4 are ≈1 for this setup.

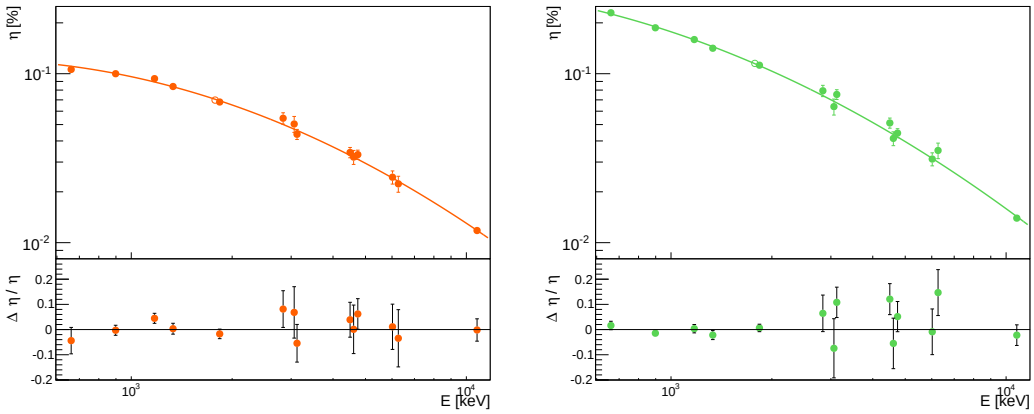

Figure 3.7: Total efficiency curve for the 55° detector (left) and for the 90° detector (right). The fitting function and residuals are also shown.

The fitting parameters are reported in table 3.4.

3.2 Data Analysis and results

The strengths of the ^{22}Ne(p,γ)^{23}Na resonances at 436 keV, 638.5 keV and 661 keV have been measured with a relative technique: since the target stoichiometry is in principle unknown, the comparatively well known resonances at 478 keV and 1279 keV have been used for normalization.
In the following paragraphs, the procedures adopted to derive the target stoichiometry and the resonance strengths are described and the results are shown.
In general, for each resonance the excitation function has been measured and the resulting yield profile has beed fitted with the following function (see sec. 2.2.4 for its derivation):

$$Y(E_0) = C\left[arctan\left(\frac{E_0 - E_R}{\Gamma_1/2}\right) - arctan\left(\frac{E_0 - E_R - \Delta E}{\Gamma_2/2}\right)\right] \qquad (3.2)$$

where C is a normalization constant. Compared with equation 3.2, two different widths Γ_1 and Γ_2 are used here. In principle, the widths of the rising and falling edges of the yield profiles depend on the resonance with Γ. However, in experimental yield profiles, the withs depend also on the beam energy spread and, for the falling edge, on the beam energy straggling. Therefore, two different widths are needed to fit the experimental data:

$$\Gamma_{1,2}^2 = \Gamma_{Res}^2 + \Gamma_{Beam}^2 \tag{3.3}$$

The fit with equation 2.29 has been used to verify the validity of the infinitely thick target approximation (i.e. $\Delta E >> \Gamma_{1,2}$) [1]. Then, a long run has been performed on the plateau of the excitation function.

3.2.1 Study of ^{22}Ne implantation profile

The amount of ^{22}Ne inside the target and the implantation profiles have been derived using the well known ^{22}Ne+p resonances at 1279 keV and 478 keV. For each resonance, a scan and then a long run at the energy of maximum yield have been performed. The resonance scan provides information on the implantation profile and depth, while the long run was used to derive the target composition. As already mentioned in sec. 2.2.4, in the approximation of infinitely thick target the reaction yield is related to the resonance strength by the following equation:

$$Y_{max}(E \to \infty) = \frac{\lambda^2}{2} \frac{m_p + m_t}{m_t} \frac{\omega\gamma}{\epsilon} \tag{3.4}$$

where ϵ is the effective stopping power. If only one species is present in the target, the effective stopping power is equal to the stopping power tabulated by SRIM for that element. When more than one species is present in the target, the effective stopping is given by:

$$\epsilon = \frac{\epsilon_X n_X + \epsilon_Y n_Y + ...}{n_X} = \epsilon_X + \frac{n_Y}{n_X}\epsilon_Y + ... \tag{3.5}$$

where X is the target element involved in the nuclear reaction of interest, Y is the inactive element, ϵ_i is the stopping power for the element i and n_i is the number of i atoms per square centimeter.
If, for a given resonance, the $\omega\gamma$ is known, eq. 3.4 can be used to derive the effective stopping power and hence the ratio n_Y/n_X (i.e. the target stoichiometry).

1279 keV resonance

The 1279 keV resonance (E_{lev} = 10017.4 keV) is a well known narrow resonance with $\omega\gamma = (10.5 \pm 1.0)$ eV [15]. This resonance has been already used in the past as a reference to normalize other resonance strengths in the ^{22}Ne+p reaction [21].
The 1279 keV resonance was also used to monitor the target stability every day. Only one target was used for the whole experiment. Fig. 3.8 shows the excitation functions of the 1279 keV resonance obtained at the beginning and at the end of the experiment. The scan is obtained integrating the 6102 keV peak in the 90° detector.

The only difference in the resonance scans of fig. 3.8 is a shift of the whole excitation function towards high energies. This is due to the build-up of contaminants on the target surface.

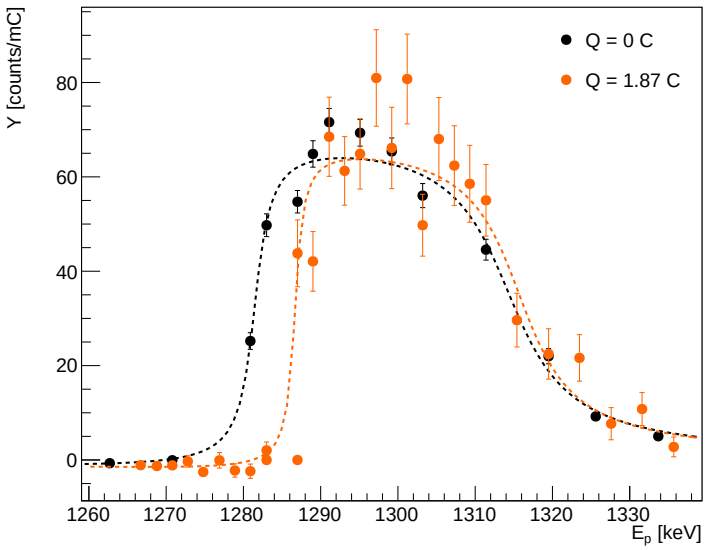

Figure 3.8: Scans of the 1279 keV resonance performed at the beginning and at the end of the experiment. The scan is obtained integrating the 6102 keV peak which is exclusively produced by the 1279 keV resonance. The results of the fit with eq. 3.2 are reported with dashed lines.

In order to determine the target stochiometry, a long run was performed at E_p = 1293 keV. Fig. 3.9 shows the long run spectrum for the 90° detector.

The full list of transitions de-exciting the 1279 keV resonance is reported in table 3.5.

In the long run both the 1279 keV and the 1264 keV resonance ($\omega\gamma = (1.1 \pm 0.3)eV$ [15]) were populated. Some transitions from the two resonances have similar energies. Indeed, some peaks in the spectrum have a double gaussian shape. Therefore, only gamma rays at 6102 keV and 9575 keV (which are populated exclusively by the 1279 keV resonance) have been used for the analysis. For each detector, the reaction yield has been calculated as:

$$Y = \frac{A}{\eta \cdot Br \cdot W(\theta) \cdot (I \cdot t / 1.602 \cdot 10^{-19})} \tag{3.6}$$

and the target stoichiometry was calculated independently for the transitions at 6102.3 keV and 9575.3 keV, inverting equations 3.4 and 3.5. The results are reported in table 3.6. Since all the values were found to be compatible within the error bars, the average stoichiometry has been adopted.

479 keV resonance

The same analysis procedure described for the 1279 keV resonance has been applied to the 479 keV resonance (E_{lev} = 9252.1 keV). The strength of this resonance has been recently measured with 10% uncertainty ($\omega\gamma = (0.524 \pm 0.051)eV$ [24]). The excitation function for the 479 keV resonance is shown in fig. 3.10.

In order to derive the target composition, a long run was performed at 506 keV proton energy. The long run spectrum is shown in fig. 3.11.

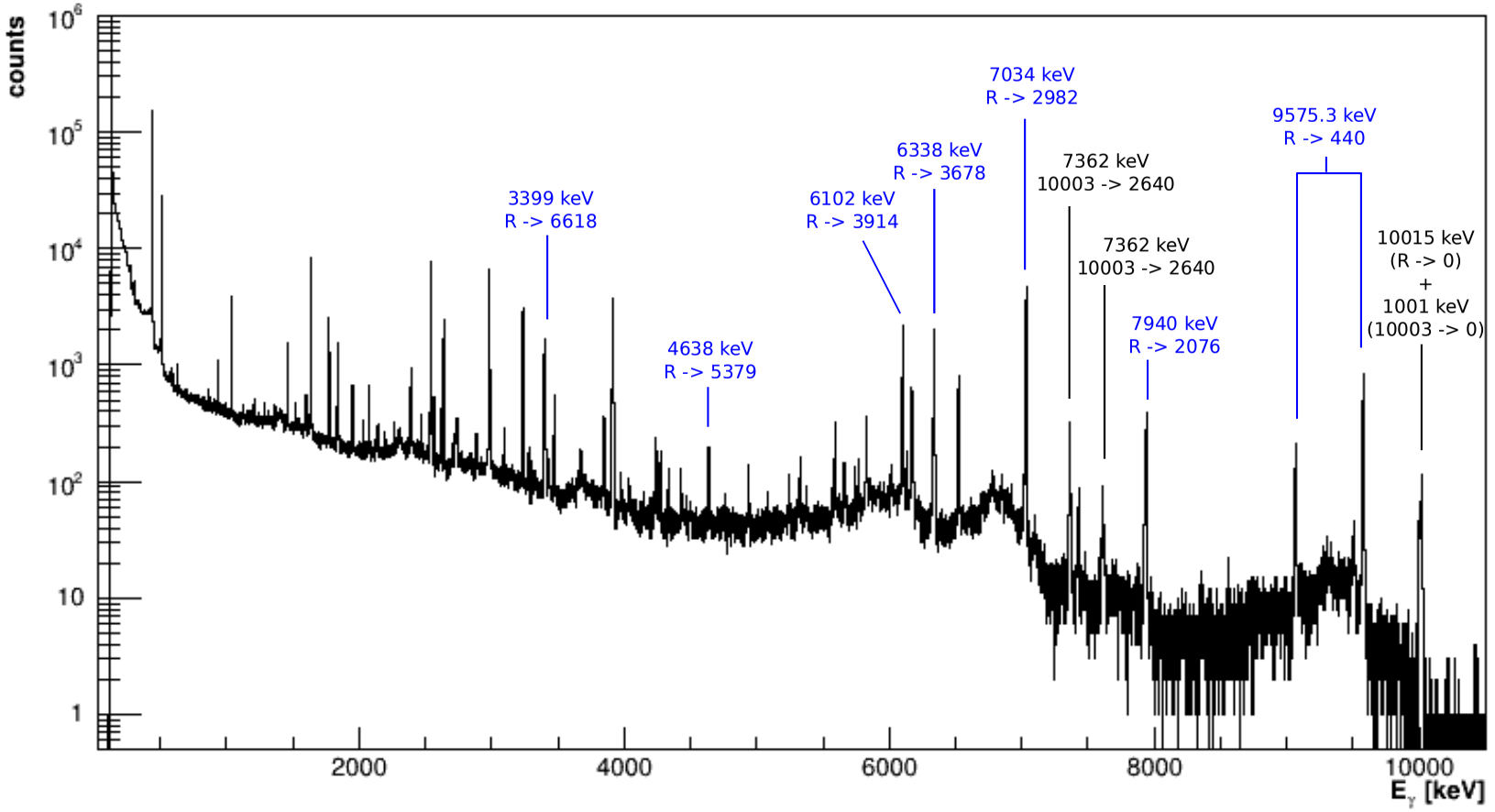

Figure 3.9: Gamma ray spectrum of the ^{22}Ne+p resonance at 1279 keV. The transitions de-exciting the 1279 keV resonance are labelled in blue. The most intense gammas from the decay of the 1264 keV resonance are also identified. Most of the low energy gammas come from the de-excitation of low-lying ^{23}Na excited states.

E_γ [keV]	E_f [keV]	Branching [%]	a_2	a_4
1386.4	8631	0.1		
1599.9	8417.4	0.3		
2141.1	7876.2	0.3		
2565.7	7451.5	0.6		
2740.0	7277.1	0.3		
2884	7133.3	0.2		
3096.6	6920.6	0.3		
3281.6	6735.5	0.2		
3399.0	6618	3.7	0.25 ± 0.13	0.14 ± 0.15
3974.8	6042.2	0.1		
4250.9	5766	0.3		
4276.0	5741.8	0.4		
4638.3	5378.6	0.7		
5242.1	4774.6	0.3		
6102.3	**3914.2**	**19**	$\mathbf{0.51 \pm 0.03}$	$\mathbf{-0.03 \pm 0.003}$
6168.4	3848	5	0.36 ± 0.07	0.01 ± 0.07
6338.9	3677.6	12	-0.40 ± 0.02	0.03 ± 0.03
7034.2	2982	34	-0.43 ± 0.02	0.00± 0.02
7312.7	2703.5	0.1		
7625.3	2390.7	0.4		
7939.9	2076	5	0.27 ± 0.04	-0.02 ± 0.04
9575.3	**440**	**15**	$\mathbf{0.22 \pm 0.03}$	$\mathbf{0.01 \pm 0.03}$
10015.1	0	1.6	-0.64 ± 0.08	0.40 ± 0.10

Table 3.5: Gamma decay modes, branching and angular distribution coefficients for the 10017 keV excited state (corresponding to the 1279 keV resonance). The angular distribution coefficients are from [55]

	E_γ [keV]	ϵ [eV/(atoms/cm^2)]	n_{Ta}/n_{Ne}
HPGe 55°	6102.3	$(1.55 \pm 0.15) \cdot 10^{-13}$	8.6 ± 0.9
	9575.3	$(1.49 \pm 0.15) \cdot 10^{-13}$	8.2 ± 0.9
HPGe 90°	6102.3	$(1.53 \pm 0.15) \cdot 10^{-13}$	8.4 ± 0.9
	9575.3	$(1.50 \pm 0.15) \cdot 10^{-13}$	8.3 ± 0.9
Average			$\mathbf{8.4 \pm 0.9}$

Table 3.6: Effective stopping power and target stoichiometry derived from the 1279 keV resonance.

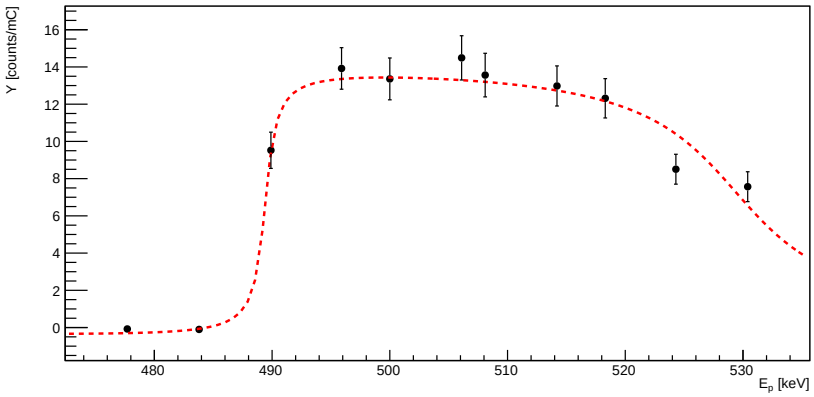

Figure 3.10: Scan of the 479 keV resonance obtained integrating the 6269 keV peak in the 90° detector. The fitting function is also shown.

	ϵ [eV/(atoms/cm^2)]	n_{Ta}/n_{Ne}
HPGe 55°	$(2.10 \pm 0.21) \cdot 10^{-13}$	7.4 ± 0.8
HPGe 90°	$(2.12 \pm 0.21) \cdot 10^{-13}$	7.5 ± 0.8
Average		$\mathbf{7.5 \pm 0.8}$

Table 3.7: Effective stopping power and target stoichiometry derived from the 479 keV resonance.

In this case, all the transitions de-exciting the 9252 keV level have been used to calculate the experimental yield. Since no information is available in the literature for the angular distribution of emitted gammas, the angular distribution has been assumed to be isotropical. The results on the target stoichiometry are summarized in table 3.7. Also in this case, the uncertainty on the target composition reflects the uncertainty on the resonance strength.

For this resonance, updated branching ratios for the decay of the level have been derived following the same procedure described in section 2.2.1. The results are reported in table 3.8, compared to the literature branchings. In order to minimize angular distribution effects, the branchings have been calculated using the 55° detector.

Since the dominant source of uncertainty on the target stoichiometry is the strength of the reference resonances, the error bar can be reduces adopting the average of the compositions derived with the two resonances. The adopted target stoichiometry is therefore:

$$\frac{n_{Ta}}{n_{Ne}} = 7.9 \pm 0.6$$

Using this target stoichimetry and the total energy loss derived from the resonances excitation functions it is possible to obtain an estimate of the number of implanted neon atoms per square centimeter. Fitting the excitation function of fig. 3.8 with equation 2.29, a total target thickness of (32.8 ± 0.8) keV is obtained. For our target, the stopping power is given by a linear combination of the stopping powers of protons in neon and tantalum:

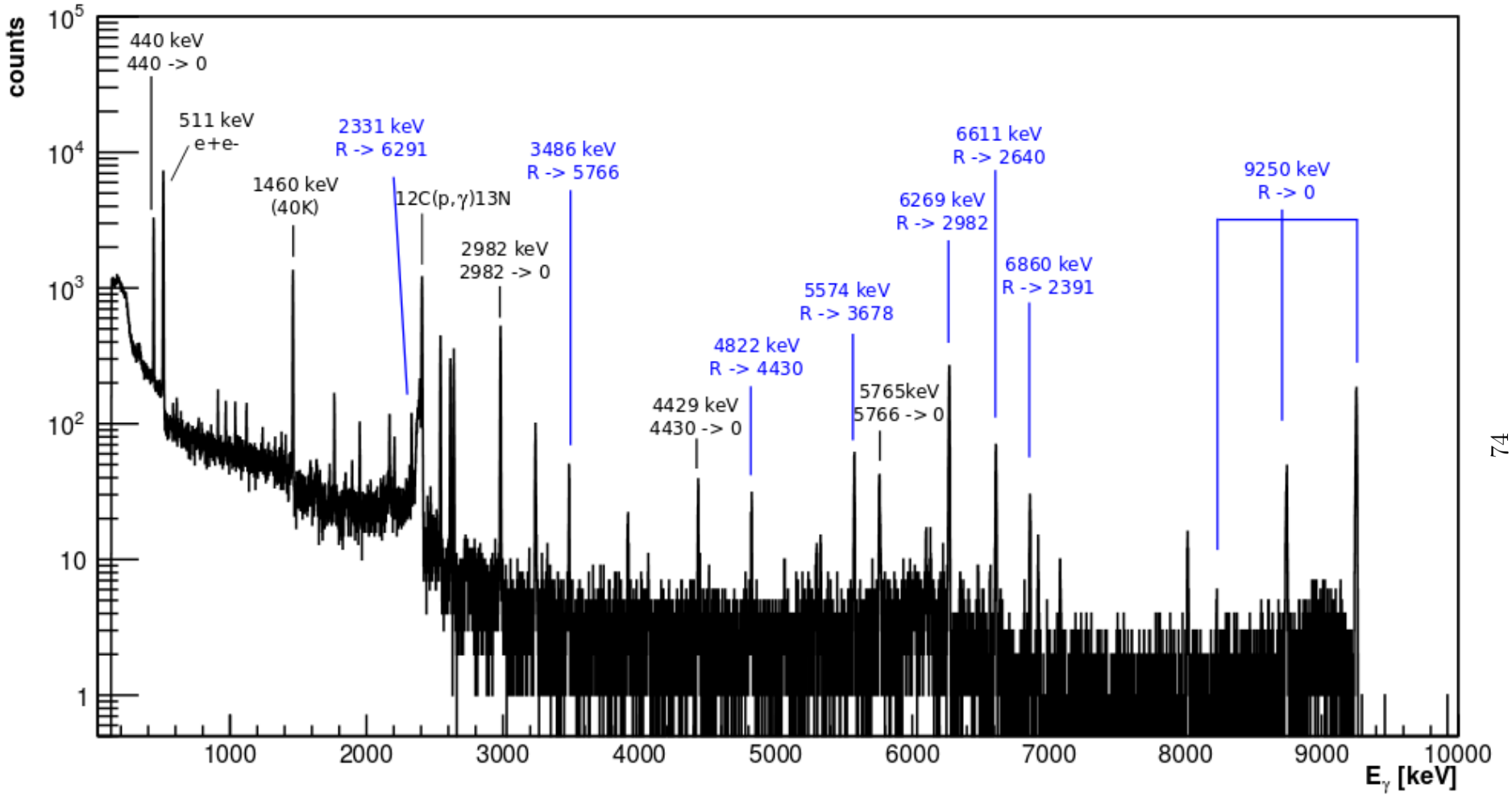

Figure 3.11: Gamma ray spectrum of the 479 keV resonance. The most intense transitions de-exciting the resonance are labelled in blue.

E_γ [keV]	E_f [keV]	Branching [%]	
		Meyer et al. [18]	This work
9250.1	0	46	43.7 ± 1.3
6860.3	2390.7	3.7	3.5 ± 0.3
6611.2	2639.85	8.5	9.9 ± 0.5
6269.1	2982	32	32.9 ± 0.9
5573.8	3677.6	4.1	3.9 ± 0.3
5337.2	3914.2	0.7	< 0.2
4821.9	4429.6	1.8	1.7 ± 0.2
3485.8	5766	2.4	1.9 ± 0.2
2331.4	6920.6	0.8	2.3 ± 0.2

Table 3.8: Gamma transitions and branching ratios for the gamma decay of the 9252 keV level (corresponding to the 479 keV resonance). The results from this ecperiment are compared with the literature data.

$$\frac{dE}{d(nx)} = \left.\frac{dE}{d(nx)}\right|_{Ne} \cdot n_{Ne} + \left.\frac{dE}{d(nx)}\right|_{Ta} \cdot n_{Ta} \tag{3.7}$$

where n_{Ne} and n_{Ta} are the percentage abundances of neon and tantalum and dE/d(nx) are the SRIM stopping powers in eV/(atoms/cm^2).
A stoichiometry of $n_{Ta}/n_{Ne} = 7.9$ translated to percentage abundances of $n_{Ta} = 88.8\%$ and $n_{Ne} = 11.2\%$. With this abundances, the stopping power of 1300 keV protons in the target calculated with eq. 3.7 is $16.2 \cdot 10^{-15}$ eV/(atoms/cm^2).
The total target thickness is related to the stopping power by the following relation:

$$\Delta E = \frac{dE}{d(nx)} \cdot (nx)_{Tot} \cdot cos(55°) \Rightarrow 32.8keV = 16.2 \cdot 10^{-18} \frac{keV}{atoms/cm^2} \cdot (nx)_{Tot} \cdot cos(55°)$$
$$\Rightarrow (nx)_{Tot} = 1.2 \cdot 10^{18} atoms/cm^2$$

where the factor cos(55°) accounts for the fact that the target is tilted by 55° with respect to the beam direction. Since only the 11.2% of the atoms is ^{22}Ne, the amount of ^{22}Ne in the target is estimated to be $1.3 \cdot 10^{17}$ atoms/cm^2. This value is lower than the ^{22}Ne dose delivered on the tantalum backing during the target implantation, but it does not take into account the finite efficiency of the implantation process (and the doses given in sec. 3.1.1 are only approximate values).

3.2.2 436 keV resonance

The 436 keV resonance ($E_{lev} = 9211$ keV) significantly contributes to the ^{22}Ne(p,γ)^{23}Na cross section, especially in the classical novae energy range. Its resonance strength is affected by a 23% uncertainty ($\omega\gamma = (0.065 \pm 0.015)eV$ [21]).
An updated value for the 436 keV resonance strength has been measured performing, as for the other resonances, a resonance scan and a long run on the

plateau of the excitation function. The resulting excitation function and long run spectum are shown in fig. 3.12 and 3.13.

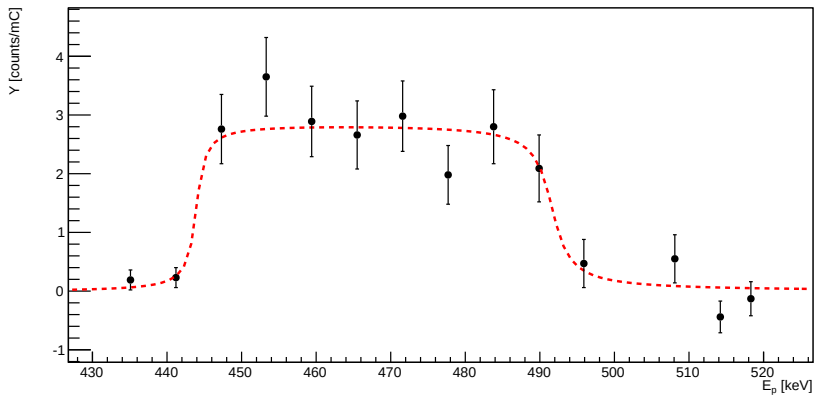

Figure 3.12: Scan of the 436 keV resonance obtained integrating the 5296 keV peak in the 90° detector. The fitting function is also shown.

The resonance strength was calculated with equations 2.30 - 2.32 and the yield was calculated summing the peak areas of all the gamma rays emitted in the level de-excitation. The $\omega\gamma$ was calculated independently for the two detectors and since compatible values were found, the average strength was adopted to minimize the statistical error (tab. 3.9).

	$\omega\gamma$ [eV]
HPGe 55°	$0.073 \pm 0.002_{stat} \pm 0.005_{syst}$
HPGe 90°	$0.075 \pm 0.002_{stat} \pm 0.006_{syst}$
Average	$\mathbf{0.074 \pm 0.002_{stat} \pm 0.006_{syst}}$

Table 3.9: Strength of the 436 keV resonance.

The new resonance strength is compatible with the literature, but the uncertainty is a factor of 3 smaller.
Updated branching ratios for the gamma decay of the 9211 keV excited state of ^{23}Na have also been calculated. The results are reported in table 3.10.

3.2.3 638.5 keV resonance

The 638.5 keV resonance (E_{lev} = 9404.8 keV) is the most intense resonance in the type Ia supernova range. Its literature strength is $\omega\gamma = (2.8 \pm 0.3)eV$ [21]. The resonance scan obtained at HZDR is reported in fig. 3.14, while the long run spectrum is displayed in fig. 3.15.

The resonance strengths derived from the spectra of the single detectors and the average $\omega\gamma$ are reported in table 3.11. Also in this case, since all the gammas de-exciting the 9404.8 keV level are observed, the yield is calculated summing the contributions from all the transitions.

The new resonance strength is compatible with the literature but the uncertainty has been reduced to the 8% level.

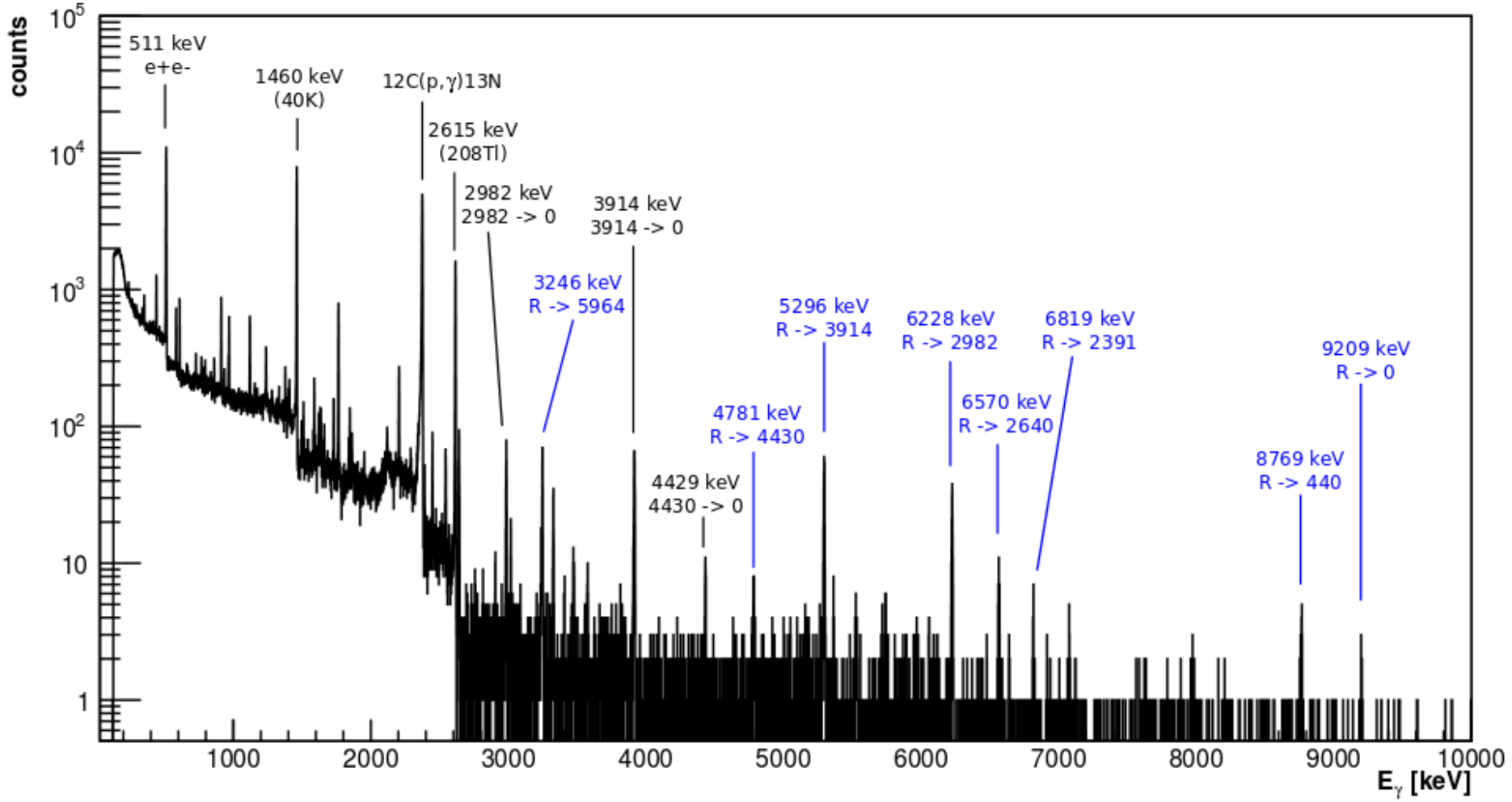

Figure 3.13: Long run spectrum acquired on the 436 keV resonance (E_p = 465.5 keV). The most intense transitions de-exciting the resonance are labelled in blue.

E_γ [keV]	E_f [keV]	Branching [%]	
		Meyer et al. [18]	This work
9209	0	0.7	1.8 ± 0.5
8769.2	440	2.1	4.9 ± 0.8
6819.2	2390.7	2.4	2.1 ± 0.5
6570.1	2639.9	9.8	5.9 ± 0.8
6228.3	2982.1	25	21.3 ± 1.5
5532.7	3677.6	3.0	3.2 ± 0.7
5362.3	3848.1	2.1	1.8 ± 0.5
5296.1	3914.2	30	31.8 ± 1.8
4780.8	4429.6	2.3	4.7 ± 0.6
3246.3	5964.4	17	16.1 ± 1.3
3016.2	6194.6	3.3	3.1 ± 0.4
1723.1	7487.8	2.3	3.3 ± 1.0

Table 3.10: Gamma transitions and new branching ratios for the gamma decay of the 9211 keV level, corresponding to the 436 keV resonance. The results from this experiment are compared with the literature data.

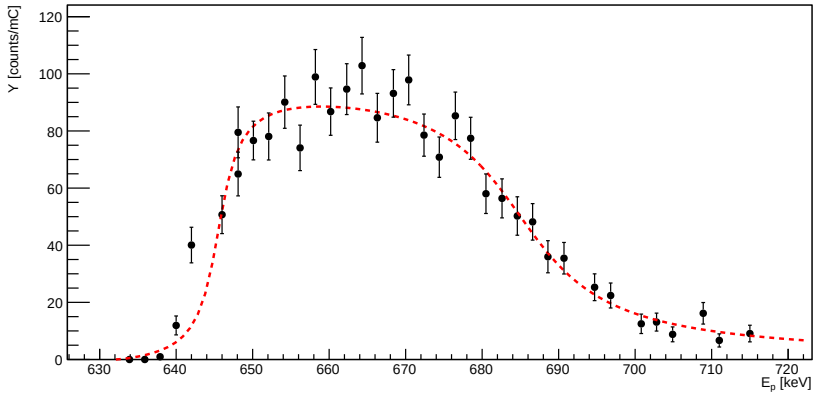

Figure 3.14: Scan of the 638.5 keV resonance obtained integrating the 9403 keV peak in the 90° detector. The fitting function is also shown.

	$\omega\gamma$ [eV]
HPGe 55°	$2.26 \pm 0.02_{stat} \pm 0.17_{syst}$
HPGe 90°	$2.36 \pm 0.02_{stat} \pm 0.18_{syst}$
Average	$\mathbf{2.31 \pm 0.02_{stat} \pm 0.18_{syst}}$

Table 3.11: Strength of the 638.5 keV resonance derived analysing the the spectra from the two detectors independently and average value.

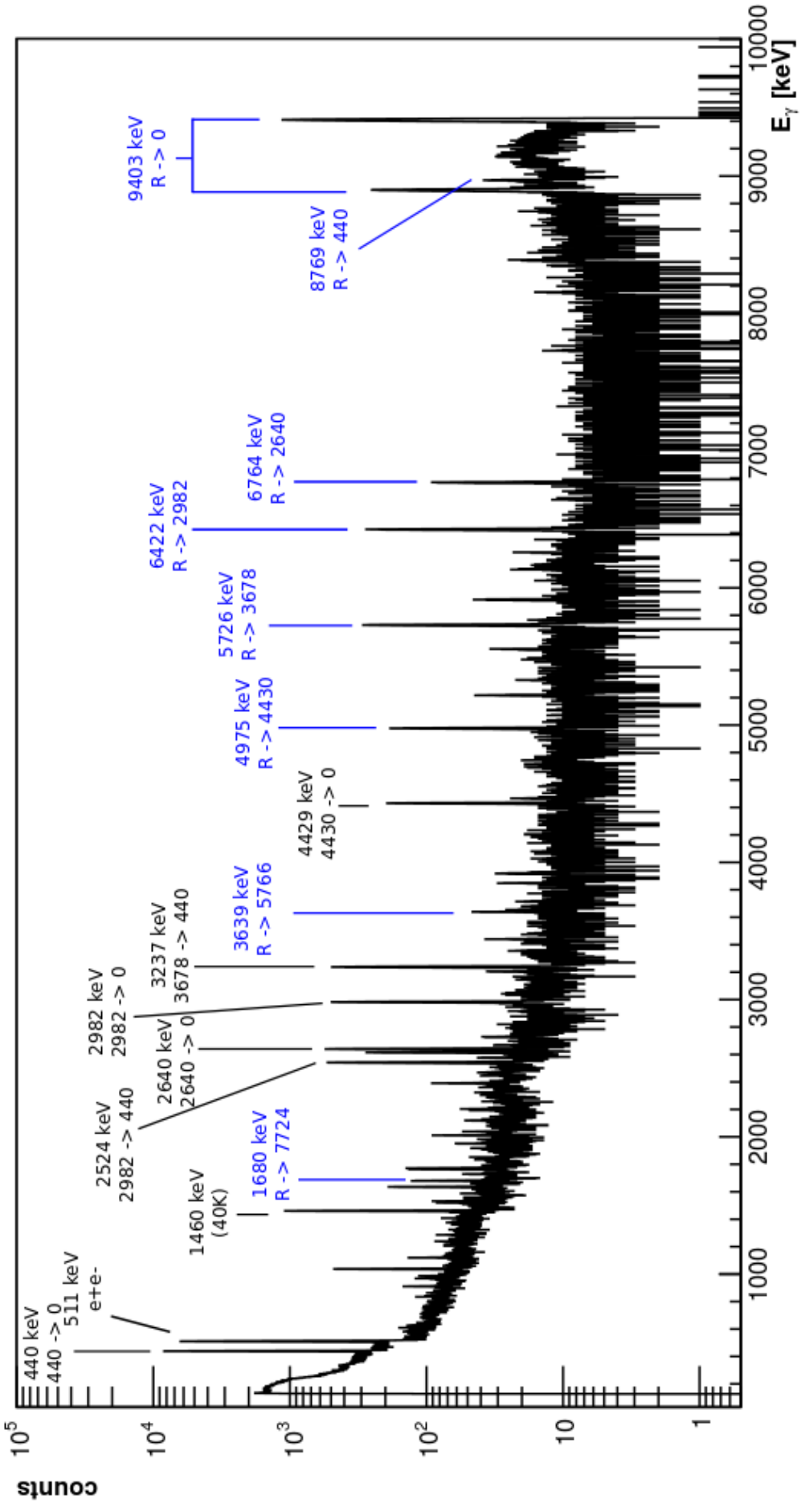

Figure 3.15: Long run spectrum on the 638.5 keV resonance ($E_p = 650$ keV). The transitions de-exciting the resonance are labelled in blue.

Updated branching ratios for the gamma decay of the 9404.8 keV level are reported in table 3.12

E_γ [keV]	E_f [keV]	Branching [%]	
		Meyer et al. [18]	This work
9402.7	0	78	76.7 ± 1
8962.9	440	1.0	1.60 ± 0.19
6763.9	2639.9	3.2	2.89 ± 0.15
6421.8	2982	7.6	7.3 ± 0.2
5726.4	3677.6	6.8	7.3 ± 0.2
4974.6	4429.6	2.7	3.41 ± 0.14
3638.5	5766	0.3	0.37 ± 0.05
1680.3	7724.4	0.4	0.43 ± 0.07

Table 3.12: Gamma transitions and branching ratios for the gamma decay of the 9404.8 keV level, corresponding to the 638.5 keV resonance. The results from this experiment are compared with the literature data.

3.2.4 661 keV resonance

The 661 keV resonance (E_{lev} = 9426.1 keV) is the weakest of the observed resonances. Its literature strength is $\omega\gamma = (0.35 \pm 0.1)$ eV. Because of the target thickness, this resonance could not be completely separated from the 638.5 keV resonance. Fig. 3.16 shows the excitation function of the 638.5 keV and 661 keV resonances obtained integrating the 440 keV peak (which collects the highest statistics) and summing the peak areas from both detectors. The rising edge of the 661 keV resonance lies on the plateau of the 638.5 keV resonance.

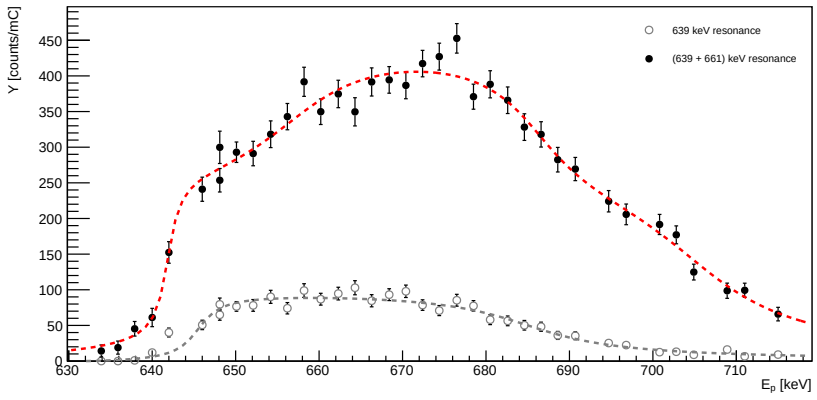

Figure 3.16: Scan of the 638.5 and 661 keV resonances obtained integrating the 440 keV peak. The fitting function is a sum of two functions like eq. 3.2. The scan of the 638.5 keV obtained integrating the 9403 keV peak is also reported.

Fig. 3.17 shows the long run spectrum at proton energy E_p = 666.3 keV. Only the most intense transitions from the 661 keV resonance are observed together with the gammas from the 638.5 keV resonance.

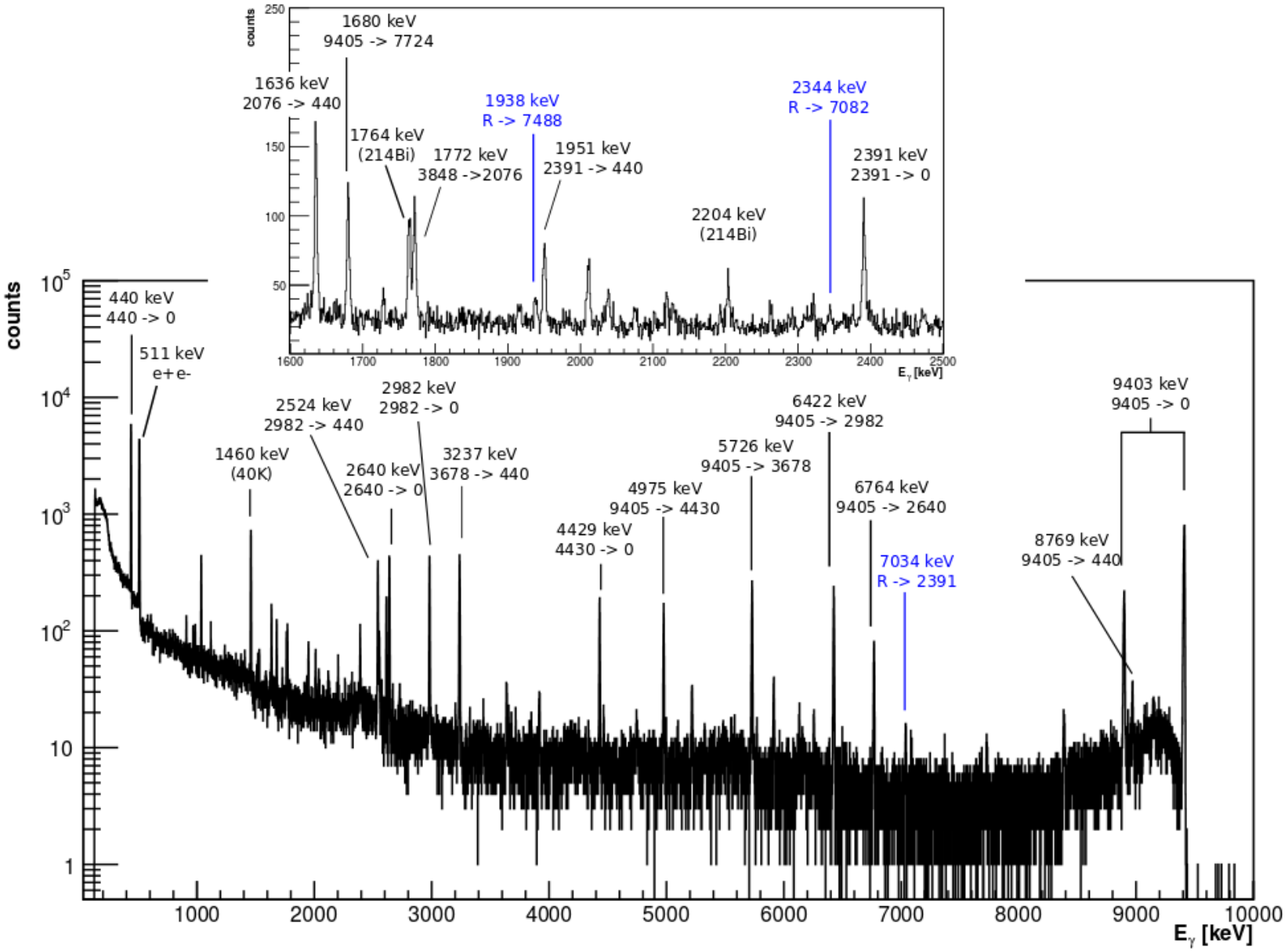

Figure 3.17: Long run spectrum on the 661 keV resonance. Both the transitions de-exciting the 661 keV resonance (in blue) and the gamma ray lines from the 638.5 keV resonance (in black) are indicated.

To confirm that the observed transitions are actually emitted in the 661 keV resonance decay, the gamma intensities relative to the 7034 keV peak have been calculated. This test could be performed only in the 90° detector, where three transitions are observed, while in the 55° spectrum only the 7034 keV line is visible.
The observed relative intensities are reported in table 3.13, together with the literature values.

E_γ [keV]	Literature relative branching [18] [%]	Observed relative branching [%]
1938.2	17	23 ± 7
2344.1	19	19 ± 8
7034.2	100	100

Table 3.13: Branching ratios for the decay of the 661 keV resonance normalized to the 7034 keV gamma intensity. The observed values are compared with the literature.

Since not all the gammas de-exciting the 9426 keV level are observed, this time the resonance yield has been calculated using the single gamma ray peaks. Table 3.14 shows the full list of gammas emitted in the 661 keV resonance decay and the corresponding branching ratios [18] and angular correlation coefficients [56] that have been used to calculate the resonance yield.

E_γ [keV]	E_f [keV]	Branching [%]	a_2	a_4
1938.2	**7487.8**	**5.8**	$\mathbf{-0.32 \pm 0.02}$	
2344.1	**7081.9**	**6.7**	$\mathbf{0.41 \pm 0.02}$	
2606.3	6819.6	5.3	-0.20 ± 0.10	
2690.4	6735.5	1.6	0.48 ± 0.08	
3117.9	6308	1.6	-0.50 ± 0.05	
3461.4	5964.4	1.2	0.47 ± 0.07	-0.16 ± 0.07
3659.8	5766	1.1	0.12 ± 0.09	
4495.9	4429.6	9.5	-0.48 ± 0.02	
5511.2	3914.2	10	-0.02 ± 0.03	
5577.3	3848.1	11	0.18 ± 0.02	
5748.5	3677.6	0.8		
6444	2982	1.0		
6785.2	2639.9	1.9	-0.03 ± 0.07	
7034.2	**2390.7**	**35**	$\mathbf{-0.453 \pm 0.008}$	
8984.2	440	1.5	-0.53 ± 0.04	
9424.0	0	6.0	0.83 ± 0.03	

Table 3.14: Gamma decay modes, branching and angular distribution coefficients for the 9426 keV excited state, corresponding to the 661 keV excited state. The branching ratios are adopted from [18], while the angular distribution coefficients are from [56]

The results are reported in 3.15. A weighted average of all values is adopted

and, since not all the values are 1σ compatible, the uncertainty is conservatively estimated as $(\omega\gamma_{max,min} - < \omega\gamma >)$

	E_γ [keV]	$\omega\gamma$ [eV]
HPGe 55°	7034.2	$0.022 \pm 0.006_{stat} \pm 0.002_{syst}$
HPGe 90°	1938.2	$0.052 \pm 0.015_{stat} \pm 0.005_{syst}$
	2344.1	$0.050 \pm 0.020_{stat} \pm 0.004_{syst}$
	7034.2	$0.032 \pm 0.006_{stat} \pm 0.003_{syst}$
Average		$\mathbf{0.030^{+0.022}_{-0.008}}$

Table 3.15: Strength of the 661 keV resonance derived analysing the the spectra from the two detectors independently and average value.

The measured resonance strength is about one order of magnitude lower than the literature value. The literature resonance strength comes from the direct experiment performed by M.A. Meyer and J.J.A. Smit in 1973 [18]. In that experiment, absolute resonance strengths were derived using the strength of the 638.5 keV resonance as a reference for normalization. No clear explanation for the discrepancy between the literature and the present strength could be found.

3.2.5 Resonance strengths

A summary of the resonance strengths determined in the HZDR experiment is given in table 3.16.

E_p [keV]	E_x [keV]	$\omega\gamma$ [eV]	
		Literature [21, 24]	This work
436	9211.02	0.065 ± 0.015	0.074 ± 0.006
638.5	9404.8	2.8 ± 0.3	2.31 ± 0.18
661	9426.1	0.35 ± 0.1	$0.030^{+0.022}_{-0.008}$

Table 3.16: Gamma transitions and branching ratios for the gamma decay of the 9252 keV level. The results from this ecperiment are compared with the literature data.

The uncertainty on the 436 keV resonance strength has been suppressed by a factor of 3 compared to the literature, while the 661 keV resonance has been found to be one order of magnitude weaker than previously thought.
The combined use of the 478 and 1279 keV resonances for normalization allows to reduce the systematic uncertainty on the resonance strengths to the 7.6%. This is the dominant source of uncertainty for the strengths of the 436 keV and 638.5 keV resonances reported in table 3.16.

Chapter 4

Astrophysical reaction rate

An updated thermonuclear reaction rate has been calculated using the new resonance strengths and upper limits measured in the LUNA and HZDR experiments. In this chapter, the method and the assumptions used to calculate the reaction rate are described and the new rate is compared with the literature.

As already mentioned in chapter 1, the thermonuclear reaction rate (defined as the number of reactions per unit of time and volume happening in a star at a given temperature) depends on the number of interacting particles, on their relative speed and on the nuclear cross section. Assuming that the velocity distribution of the interacting particles follows a Maxwell-Boltzmann distribution, one obtaines:

$$N_A\langle\sigma v\rangle = N_A\left(\frac{8}{\pi\mu}\right)^{1/2}\frac{1}{(kT)^{3/2}}\int_0^\infty E\sigma(E)exp\left(-\frac{E_R}{kT}\right)dE \tag{4.1}$$

All possible contributions to the total cross section σ(E) should be included in the reaction rate calculation. In the case of the ^{22}Ne(p,γ)^{23}Na reaction, the cross section is characterized by the contribution of both narrow resonances and direct capture. The treatment of these components is discussed in the following.

4.1 Nonresonant reaction rate

The nonresonant cross section is usually expressed as a function of the astrophysical S-factor:

$$\sigma = \frac{1}{E}S(E)e^{-2\pi\eta} \tag{4.2}$$

where the S-factor is a smooth function of the energy. The direct capture cross section and corresponding S(E) curve has been measured by J. Görres at al. in the energy range between 300 and 1600 keV [16]. In Ref. [16], the direct capture to different ^{23}Na excited states has been measured and the total S-factor has been calculated as the sum of of all contributions. The total S(E) curve was found to be nearly energy independent, therefore a constant S-factor of 62 keV·b was adopted in the reaction rate calulation. This value corresponds to the extrapolation of the S(E) curve to zero energy. For the present purposes, the same reaction rate parametrization given in [16] has been adopted:

$$N_A\langle\sigma v\rangle = 1.05 \cdot 10^9 T_9^{-2/3} exp(-19.431 \cdot T_9^{-1/3}) \quad (4.3)$$

The direct capture S-factor measured by Görres at al. has also been adopted in the NACRE and C. Iliadis et al. reaction rate compilations [4, 5]. Since no uncertainty is given in [16] for the direct capture contribution, the same uncertainty quoted in [5] is adopted in the present calculation (±40%). This choice allows to compare the present reaction rate with the literature and to estimate the improvement in the reaction rate uncertainty due to the new results on the resonant component.

4.2 Narrow-resonance reaction rate

In order to account for the contribution of narrow resonances, the thermonuclear reaction rate can be evaluated substituting σ(E) with the Breit-Wigner formula in eq. 4.1. The integration gives:

$$N_A\langle\sigma v\rangle = \frac{1.5399 \cdot 10^{11}}{T_9^{3/2}} \left(\frac{M_0 + M_1}{M_0 M_1}\right)^{3/2} \sum_i (\omega\gamma) e^{-11.605 E_i/T_9} \quad (4.4)$$

where the sum is over all the narrow resonances i contributing to the cross section and the resonance strenghts $\omega\gamma_i$ and center of mass energies E_i are all in units of MeV.

Table 4.1 shows the resonance strenghts used to calculate the ^{22}Ne(p,γ)^{23}Na thermonuclear reaction rate. For the upper limits, the same approach adopted in the NACRE compilation has been used: the adopted rate is calculated multiplying the upper limit by 0.1, the high rate is calculated with the upper limit and the low rate is calculated with resonance strength equal to zero.

In fig. 4.1, the updated reaction rate for the ^{22}Ne(p,γ)^{23}Na reaction is compared with the rates provided in the two referecen compilations [4, 5]. To enphasize the improvement on the reaction rate uncertainty, the rates normalized to the Iliadis et al. value are also displayed (fig. 4.2).

The updated reaction rate lies between the ones reported in [4, 5]. The reaction rate and corresponding uncertainty adopted in [5] are significantly smaller compared to NACRE and to the present work. The reason for the discrepancy lies in the different choice of the adopted resonances. Indeed, Iliadis et al. disregard completely the resonances at 71 and 105 keV, which are the main sources of uncertainty for the NACRE rate and for the reaction rate calculated here.
Fig. 4.3 shows the contribution of the single resonances to the reaction rate. All the curves are normalized to the reaction rate from this work.

At temperatures below 0.09 GK (in the Gamow peak of AGB-HBB), the uncertainty on the reaction rate is still dominated by the upper limit on the 71 keV resonance. Between 0.09 and 0.3 GK (in the Gamow peak of classical novae explosions), the uncertainty on the reaction rate is up to a factor of 9 smaller than NACRE and up to a factor of 2 smaller than C. Iliadis et al. This improvement is produced by the first detection of the resonances at 156.2, 189.5 and 259.7 keV

E_{res}^{CM} [keV]	E_{res}^{LAB} [keV]	$\omega\gamma$ [eV] NACRE [4]	Iliadis et al. [15]	Adopted
27.9	29	-	$\leq 2.6 \cdot 10^{-25}$	$\leq 2.6 \cdot 10^{-25}$
35.4	37	$(6.8 \pm 1.0) \cdot 10^{-15}$	$(3.1 \pm 1.2) \cdot 10^{-15}$	$(3.1 \pm 1.2) \cdot 10^{-15}$
68	71	$\leq 4.2 \cdot 10^{-9}$	-	$\leq 3.4 \cdot 10^{-9}$ *
100	105	$\leq 6.0 \cdot 10^{-7}$	-	$\leq 7.0 \cdot 10^{-9}$ *
149.4	156.2	$(6.5 \pm 1.9) \cdot 10^{-7}$	$(9.2 \pm 3.7) \cdot 10^{-9}$	$(1.48 \pm 0.10) \cdot 10^{-7}$ *
181.3	189.5	$\leq 2.6 \cdot 10^{-6}$	$\leq 2.6 \cdot 10^{-6}$	$(1.87 \pm 0.05) \cdot 10^{-6}$ *
206	215	$\leq 1.4 \cdot 10^{-6}$	-	$\leq 2.4 \cdot 10^{-8}$ *
248.4	259.7	$\leq 2.6 \cdot 10^{-6}$	$\leq 1.3 \cdot 10^{-6}$	$(6.89 \pm 0.16) \cdot 10^{-6}$ *
278	291	$\leq 2.2 \cdot 10^{-6}$	$\leq 2.2 \cdot 10^{-6}$	$\leq 2.2 \cdot 10^{-6}$
309	323	$\leq 2.2 \cdot 10^{-6}$	$\leq 2.2 \cdot 10^{-6}$	$\leq 2.2 \cdot 10^{-6}$
319	334	$\leq 3.0 \cdot 10^{-6}$	$\leq 3.0 \cdot 10^{-6}$	$\leq 3.0 \cdot 10^{-6}$
353	369	-	$\leq 6.0 \cdot 10^{-4}$	$\leq 6.0 \cdot 10^{-4}$
377	394	-	$\leq 6.0 \cdot 10^{-4}$	$\leq 6.0 \cdot 10^{-4}$
417	436	0.07 ± 0.02	0.065 ± 0.015	0.074 ± 0.006 *
458	479	0.49 ± 0.13	0.45 ± 0.1	0.524 ± 0.051
602	630	0.03 ± 0.01	0.03 ± 0.01	0.03 ± 0.01
611	639	2.70 ± 0.25	2.8 ± 0.3	2.31 ± 0.18 *
632	661	0.34 ± 0.09	0.35 ± 0.1	$0.030^{+0.022}_{-0.008}$ *

* From present work

Table 4.1: Summary of ^{22}Ne(p,γ)^{23}Na resonance strengths adopted in the two reference compilations of thermonuclear reaction rates and values adopted for the present calculation. The resonance strengths measured at LUNA or HZDR are marked with a star.

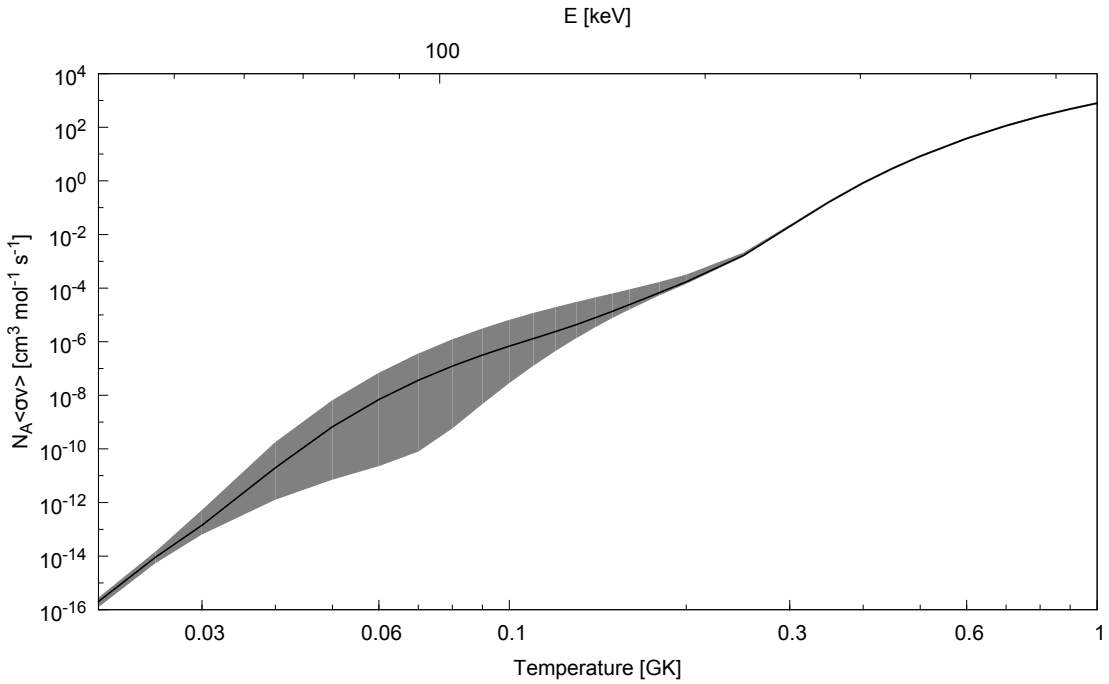

Figure 4.1: Updated reaction rate including the new results of this work, compared with the literature reaction rates [4, 5]. The lines represent the adopted values while the bands represent the uncertainties.

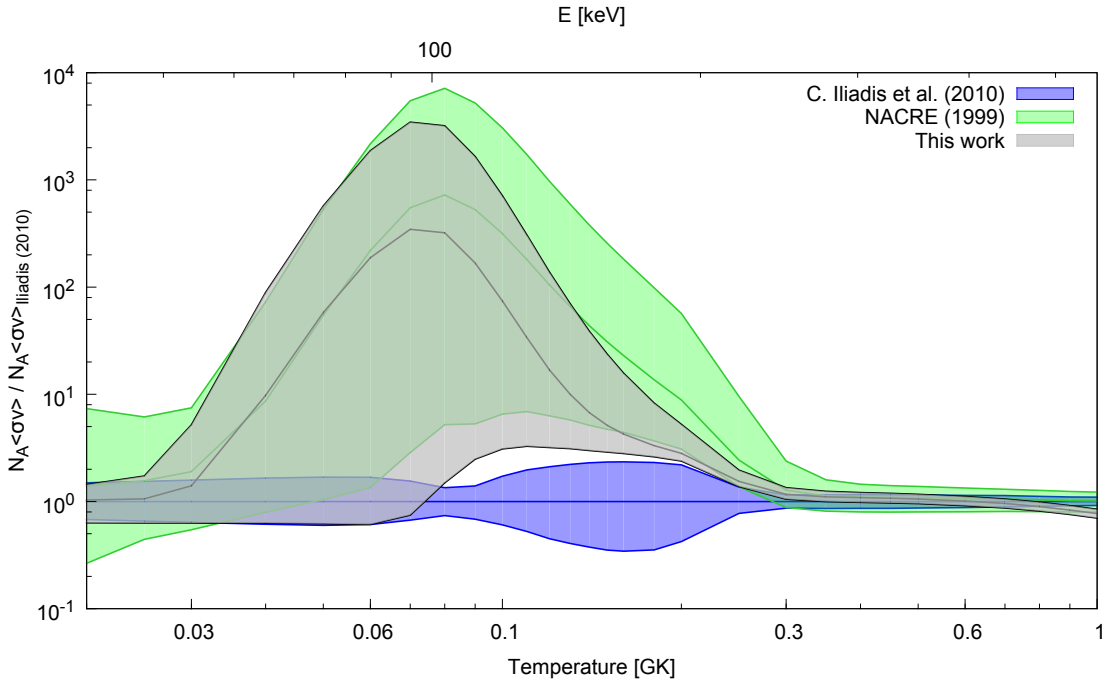

Figure 4.2: Same as fig. 4.1, but with all the rates divided by the median rate from Iliadis et al.

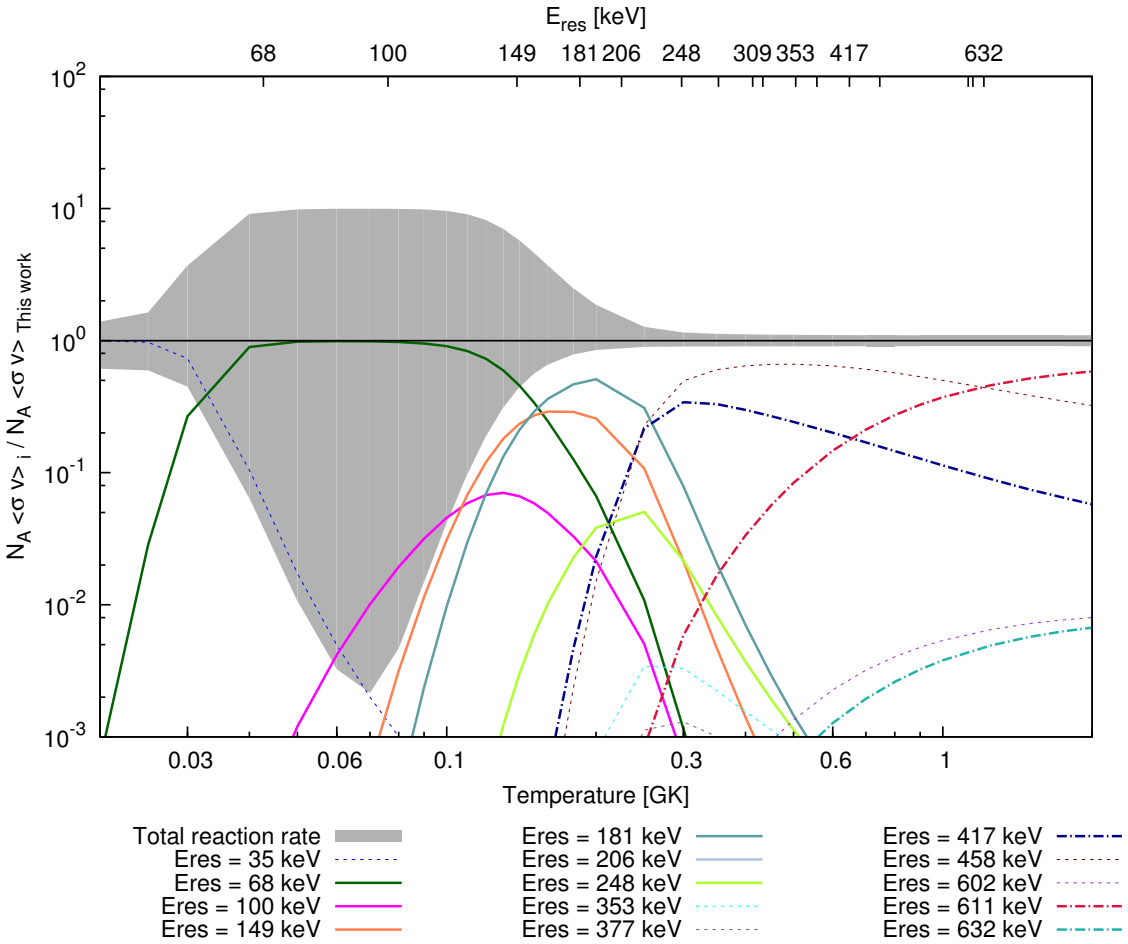

Figure 4.3: Contribution of single resonances to the total reaction rate. The gray band represent the relative uncertainty on the reaction rate determined here. All the contributions are normalized to the adopted value from this work. The dashed lines represents the resonances for which only an upper limit is available.

and by the two orders of magnitude reduction of the upper limits on the 100 and 215 keV resonances.

Summary

The ^{22}Ne(p, γ)^{23}Na reaction has been studied in the energy range between 70 and 660 keV with two different experiments. The resonances at proton energy below 400 keV have been investigated at LUNA. For this measurement, a windowless gas target filled with enriched ^{22}Ne was used and the gamma rays emitted in the ^{23}Na decay were detected by two high-purity germanium detectors. A preliminary experimental campaign was needed to characterize the gas target. First, the gas density with no beam has been measured at different positions inside the target chamber. Then, the beam heating effect has been measured for the first time for a proton beam in neon gas exploiting the ^{21}Ne(p,γ)^{22}Na resonance at 271.56 keV. The experiment performed at LUNA led to the first detection of the resonances at 156.2, 189.5 and 259.7 keV proton energy. For these resonances, resonance strengths in the $10^{-6} - 10^{-7}$eV range have been measured. Moreover, the decay schemes of the corresponding excited states of ^{23}Na have been extended with the observation of new transitions. The LUNA measurement also allowed to reduce the upper limits on the unobserved resonances at 71, 105 and 215 keV by about two orders of magnitude compared to the previous direct measurement [17].
The aim of the HZDR experiment was, instead, to provide a precise measurement of the strength of the resonances between 400 and 660 keV. The experiment was performed with a ^{22}Ne solid target and two high-purity germanuim detectors surrounded by BGO anti-Compton shields. Resonance strengths have been normalized to the well known ^{22}Ne+p resonances at 1279 keV and 478 keV. This measurement allowed to reduce up to a factor of three the uncertainty on the strengths of the resonances at 436 keV and 638.5 keV. Moreover, the strength of the 661 keV resonance has been revised downward by one order of magnitude.
Taking into account the new results, an updated thermonuclear reaction rate has been calculated. For stellar temperatures below 0.09 GK (in the range of interest for AGB stars), the uncertainty on the ^{22}Ne(p, γ)^{23}Na reaction rate is still dominated by the upper limit on the 71 keV resonance. Between 0.09 and 0.3 GK (in the Gamow window of classical nova explosions) the uncertainty on the new reaction rate is about one order of magnitude lower than the one provided by NACRE.
Further improvements will be achieved in the next phase of the ^{22}Ne(p, γ)^{23}Na study at LUNA, when the windowless gas target system will be coupled to a 4π BGO detector with high efficiency. In this phase, the unobserved resonances will be investigated again with improved sensitivity and the direct capture cross section will also be studied directly in the Gamow window of AGB stars and classical novae.

Bibliography

[1] C. Iliadis. *Nuclear Physics of Stars*. Wiley-VCH, 2007.

[2] C. E. Rolfs and Rodney. W. S. *Cauldrons in the Cosmos*. The University of Chicago Press, 1988.

[3] J.B. Marion and W.A. Fowler. Nuclear Reactions with the Neon Isotopes in Stars. *The Astrophysical Journal*, 125:221, January 1957.

[4] C. Angulo et al. A compilation of charged-particle induced thermonuclear reaction rates. *Nuclear Physics A*, 656(1):3 – 183, 1999.

[5] C. Iliadis, R. Longland, A.E. Champagne, A. Coc, and R. Fitzgerald. Charged-particle thermonuclear reaction rates: Ii. tables and graphs of reaction rates and probability density functions. *Nuclear Physics A*, 841(14):31 – 250, 2010. The 2010 Evaluation of Monte Carlo based Thermonuclear Reaction Rates.

[6] A. L. Sallaska et al. Absolute determination of the ^{22}Na(p,γ)^{23}Mg reaction rate in novae. *Phys. Rev. C*, 83:034611, 2011.

[7] E. Carretta et al. Properties of stellar generations in globular clusters and relations with global parameters. *A&A*, 516:A55, 2010.

[8] Carretta, E., Lucatello, S., Gratton, R. G., Bragaglia, A., and DOrazi, V. Multiple stellar populations in the globular cluster ngc1851. *A&A*, 533:A69, 2011.

[9] R. Gratton, C. Sneden, and E. Carretta. Abundance variations within globular clusters. *Annual Review of Astronomy and Astrophysics*, 42(1):385–440, 2004.

[10] R. G. Izzard, M. Lugaro, A. I. Karakas, C. Iliadis, and M. van Raai. Reaction rate uncertainties and the operation of the NeNa and MgAl chains during HBB in intermediate-mass AGB stars. *A&A*, 466(2):641–648, 2007.

[11] Jordi José and Margarita Hernanz. Nucleosynthesis in classical nova explosions. *Journal of Physics G: Nuclear and Particle Physics*, 34(12):R431, 2007.

[12] C. Iliadis, A. Champagne, J. José, S. Starrfield, and P. Tupper. The effects of thermonuclear reaction-rate variations on nova nucleosynthesis: A sensitivity study. *The Astrophysical Journal Supplement Series*, 142(1):105, 2002.

[13] A. Goobar and B. Leibundgut. Supernova cosmology: Legacy and future. *Annual Review of Nuclear and Particle Science*, 61(1):251–279, 2011.

[14] A. Parikh, J. José, I. R. Seitenzahl, and F. K. Röpke. The effects of variations in nuclear interactions on nucleosynthesis in thermonuclear supernovae. *A&A*, 557:A3, 2013.

[15] C. Iliadis, R. Longland, A.E. Champagne, and A. Coc. Charged-particle thermonuclear reaction rates: Iii. nuclear physics input. *Nuclear Physics A*, 841(14):251 – 322, 2010. The 2010 Evaluation of Monte Carlo based Thermonuclear Reaction Rates.

[16] J. Görres et al. Proton-induced direct capture on ^{21}Ne and ^{22}Ne. *Nuclear Physics A*, 408(2):372 – 396, 1983.

[17] J. Görres, C. Rolfs, P. Schmalbrock, H.P. Trautvetter, and J. Keinonen. Search for low-energy resonances in ^{21}Ne(p, γ)^{22}Na and ^{22}Ne(p, γ)^{23}Na. *Nuclear Physics A*, 385(1):57 – 75, 1982.

[18] M.A. Meyer and J.J.A. Smit. The energy levels of ^{23}Na. *Nuclear Physics A*, 205(1):177 – 192, 1973.

[19] M. Piiparinen, A. Anttila, and M. Viitasalo. A study of the excited states of ^{23}Na from the ^{22}Ne(p,γ)^{23}Na reaction. *Zeitschrift für Physik*, 247(5):400–407, 1971.

[20] S. E. Hale, A. E. Champagne, C. Iliadis, V. Y. Hansper, D. C. Powell, and J. C. Blackmon. Investigation of the ^{22}Ne(p,γ)^{23}Na reaction via (^{3}He,d) spectroscopy. *Phys. Rev. C*, 65:015801, Dec 2001.

[21] P.M. Endt. Energy levels of A = 21 - 44 nuclei (VII). *Nuclear Physics A*, 521(0):1 – 400, 1990.

[22] J. R. Powers, H. T. Fortune, R. Middleton, and Ole Hansen. Nuclear structure of ^{23}Na: The ^{22}Ne(^{3}He,d) reaction. *Phys. Rev. C*, 4:2030–2046, Dec 1971.

[23] D. G. Jenkins et al. γ-ray spectroscopy of the a = 23, t = 1/2 nuclei ^{23}Na and ^{23}Mg: High-spin states, mirror symmetry, and applications to nuclear astrophysical reaction rates. *Phys. Rev. C*, 87:064301, Jun 2013.

[24] R. Longland et al. Resonance strength in ^{22}Ne(p,γ)^{23}Na from depth profiling in aluminum. *Phys. Rev. C*, 81:055804, May 2010.

[25] C. Broggini, D. Bemmerer, A. Guglielmetti, and R. Menegazzo. Luna: Nuclear astrophysics deep underground. *Annual Review of Nuclear and Particle Science*, 60(1):53–73, 2010.

[26] C. Casella et al. A new setup for the underground study of capture reactions. *Nuclear Instruments and Methods in Physics Research Section A: Accelerators, Spectrometers, Detectors and Associated Equipment*, 489(13):160 – 169, 2002.

[27] A. Formicola et al. The LUNA II 400 kV accelerator. *Nuclear Instruments and Methods in Physics Research Section A: Accelerators, Spectrometers, Detectors and Associated Equipment*, 507(3):609 – 616, 2003.

[28] R. B. Bird, W. E. Stewart, and E. N. Lightfoot. *Transport phenomena*. John Wiley & Sons Inc., revised second edition edition, 2007.

[29] J. Görres, K.U. Kettner, H. Kräwinkel, and C. Rolfs. The influence of intense ion beams on gas target densities. *Nuclear Instruments and Methods*, 177(23):295 – 303, 1980.

[30] D. Bemmerer et al. Low energy measurement of the ^{14}N(p,γ)^{15}O total cross section at the LUNA underground facility. *Nuclear Physics A*, 779(0):297 – 317, 2006.

[31] M. Marta et al. Study of beam heating effect in a gas target through Rutherford scattering. *Nuclear Instruments and Methods in Physics Research Section A: Accelerators, Spectrometers, Detectors and Associated Equipment*, 569(3):727 – 731, 2006.

[32] James F. Ziegler, M.D. Ziegler, and J.P. Biersack. SRIM the stopping and range of ions in matter (2010). *Nuclear Instruments and Methods in Physics Research Section B: Beam Interactions with Materials and Atoms*, 268(1112):1818 – 1823, 2010. 19th International Conference on Ion Beam Analysis.

[33] H.W. Becker et al. Low energy resonances in ^{21}Ne(p,γ)^{22}Na examined with a high energy resolution ion beam. *Zeitschrift für Physik A Hadrons and Nuclei*, 343(3):361–366, 1992.

[34] D. Bemmerer et al. Feasibility of low-energy radiative-capture experiments at the LUNA underground accelerator facility. *The European Physical Journal A - Hadrons and Nuclei*, 24(2):313–319, 2005.

[35] A. Caciolli et al. Ultra-sensitive in-beam γ -ray spectroscopy for nuclear astrophysics at LUNA. *The European Physical Journal A*, 39(2):179–186, 2009.

[36] D.R. Tilley et al. Energy levels of light nuclei A = 5, 6, 7. *Nuclear Physics A*, 708(12):3 – 163, 2002.

[37] E. Browne and J.K. Tuli. Nuclear Data Sheets for A = 137. *Nuclear Data Sheets*, 108(10):2173 – 2318, 2007.

[38] J. K. Tuli. Nuclear Data Sheets for A = 60. *Nuclear Data Sheets*, 100(3):347 – 481, 2003.

[39] G. Mukherjee and A.A. Sonzogni. Nuclear Data Sheets for A = 88. *Nuclear Data Sheets*, 105(2):419 – 556, 2005.

[40] A. Formicola et al. Astrophysical S-factor of ^{14}N(p,γ)^{15}O. *Physics Letters B*, 591(12):61 – 68, 2004.

[41] E. L. Brady and M. Deutsch. Angular correlation of successive gamma-rays. *Phys. Rev.*, 78:558–566, Jun 1950.

[42] M. Marta. *The $^{14}N(p,\gamma)^{15}O$ reaction studied at low and high beam energy.* PhD thesis, Fakultät Mathematik und Naturwissenschaften der Technischen Universität Dresden, 2011.

[43] M. E. Rose. The analysis of angular correlation and angular distribution data. *Phys. Rev.*, 91:610–615, Aug 1953.

[44] F. Cavanna. PhD thesis, Università degli studi di Genova, 2015.

[45] Gordon R. Gilmore. *Practical gamma-ray spectrometry.* John Wiley & Sons, second edition edition, 2008.

[46] M. Friedrich, W. Bürger, D. Henke, and S. Turuc. The Rossendorf 3 MV Tandetron: a new generation of high-energy implanters. *Nuclear Instruments and Methods in Physics Research Section A: Accelerators, Spectrometers, Detectors and Associated Equipment*, 382(12):357 – 360, 1996. Proceedings of the Seventh International Conference on Heavy Ion Accelerator Technology.

[47] Konrad Schmidt et al. Resonance triplet at $E_\alpha = 4.5$ MeV in the ^{40}Ca(α,γ)^{44}Ti reaction. *Phys. Rev. C*, 88:025803, Aug 2013.

[48] E. Selin, S.E. Arnell, and O. Almén. On the properties of electromagnetically separated noble gas targets for nuclear reaction studies. *Nuclear Instruments and Methods*, 56(2):218 – 228, 1967.

[49] S. Seuthe et al. Production and properties of implanted targets. *Nuclear Instruments and Methods in Physics Research Section A: Accelerators, Spectrometers, Detectors and Associated Equipment*, 260(1):33 – 42, 1987.

[50] U. Giesen et al. The astrophysical implications of low-energy resonances in ^{21}Ne + α. *Nuclear Physics A*, 561(1):95 – 111, 1993.

[51] H.Y. Lee, J. Görres, H.-W. Becker, E. Stech, E. Strandberg, and M. Wiescher. Production and characterization of oxygen-reduced implanted ^{21}Ne targets. *Nuclear Instruments and Methods in Physics Research Section B: Beam Interactions with Materials and Atoms*, 267(2122):3539 – 3544, 2009.

[52] J. F. Ziegler, J.P. Biersack, and M.D. Ziegler. *SRIM The stopping and range of ions in matter (2010).* SRIM Co., 2008, 2008.

[53] A. Anttila, J. Keinonen, M. Hautala, and I. Forsblom. Use of the ^{27}Al(p,γ)^{28}Si, E_p = 992 keV resonance as a gamma-ray intensity standard. *Nuclear Instruments and Methods*, 147(3):501 – 505, 1977.

[54] F. Zijderhand, F.P. Jansen, C. Alderliesten, and C. van der Leun. Detector-efficiency calibration for high-energy gamma-rays. *Nuclear Instruments and Methods in Physics Research Section A: Accelerators, Spectrometers, Detectors and Associated Equipment*, 286(3):490 – 496, 1990.

[55] M. Viitasalo, M. Piiparinen, and A. Anttila. Angular distribution measurements of gamma-rays from the ^{22}Ne(p,γ)^{23}Na reaction. *Zeitschrift für Physik*, 250(5):387–394, 1972.

[56] E.L. Bakkum and C. Van Der Leun. Low-spin states of ^{23}Na investigated with the reaction ^{22}ne(p,γ)^{23}na. *Nuclear Physics A*, 500(1):1 – 42, 1989.

[57] R. Longland, C. Iliadis, A.E. Champagne, J.R. Newton, C. Ugalde, A. Coc, and R. Fitzgerald. Charged-particle thermonuclear reaction rates: I. monte carlo method and statistical distributions. *Nuclear Physics A*, 841(14):1 – 30, 2010. The 2010 Evaluation of Monte Carlo based Thermonuclear Reaction Rates.

Acknowledgements

I would like to thank all the people who contributed to this work.
I am very grateful to Daniel Bemmerer for all the things he taught me and for his constant, tireless support. Special thanks to Francesca Cavanna who shared every single part of this work, through thick and thin. It was great to work with her.
Thanks to Federico Ferraro and Alessandra Slemer for their work on the HZDR experiment. We made a good team and it was nice to share the Dresden experience with them.
I am thankful to Carlo Broggini for supervising my work and for his wise advice.

Special thanks to Antonio Caciolli for bearing with me and for all the helpful discussions. I'm also indebted to Roberto Menegazzo for the huge help in the simulation and design of the experimental setup.
Finally, I would like to thank all the LUNA collaborators. Working for the LUNA experiment has been a wonderful experience and I learned from every person I shared a shift with.